

# Lawrence Berkeley National Laboratory

## Lawrence Berkeley National Laboratory

### Title

DEFECTS, PHASE TRANSFORMATIONS AND MAGNETIC PROPERTIES OF LITHIUM FERRITE

### Permalink

<https://escholarship.org/uc/item/0w9054x3>

### Author

Mishra, Raja Kishore

### Publication Date

1977-03-01

c.2

DEFECTS, PHASE TRANSFORMATIONS AND  
MAGNETIC PROPERTIES OF LITHIUM FERRITE

Raja Kishore Mishra  
(Ph. D. thesis)

RECEIVED  
LAWRENCE  
BERKELEY LABORATORY

APR 18 1977

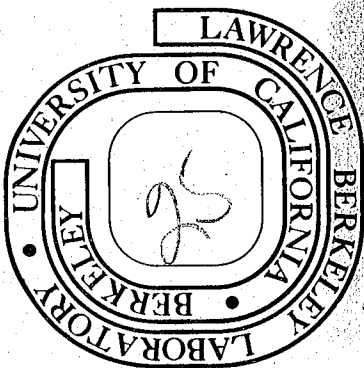
March 1977

LIBRARY AND  
DOCUMENTS SECTION

Prepared for the U. S. Energy Research and  
Development Administration under Contract W-7405-ENG-48

**TWO-WEEK LOAN COPY**

*This is a Library Circulating Copy  
which may be borrowed for two weeks.  
For a personal retention copy, call  
Tech. Info. Division, Ext. 5716*



c.2

LEGAL NOTICE

This report was prepared as an account of work sponsored by the United States Government. Neither the United States nor the Department of Energy, nor any of their employees, nor any of their contractors, subcontractors, or their employees, makes any warranty, express or implied, or assumes any legal liability or responsibility for the accuracy, completeness or usefulness of any information, apparatus, product or process disclosed, or represents that its use would not infringe privately owned rights.

...Ursachen erkennen, ...das eben ist Denken, und dadurch allein werden  
Empfindungen zu Erkenntnissen...

Herman Hesse - "Sidhartha"

...to recognize causes, ...is to think, and through thought alone,  
feelings become knowledge...

TABLE OF CONTENTS

Abstract . . . . .	v
I. Introduction . . . . .	1
II. Crystal Structure. . . . .	4
A. The Spinel Space Group . . . . .	4
B. Atomic Arrangements. . . . .	7
III. Phase Decomposition, Material Loss and Surface Energy. . . . .	10
A. Material Loss and a High Temperature Phase Transformation . . . . .	10
1. Introduction . . . . .	10
2. Experimental Procedure . . . . .	11
3. Results and Interpretation . . . . .	13
4. Discussion . . . . .	21
B. Material Loss and Surface Energy of Spinel . . . . .	26
1. Introduction . . . . .	26
2. Experiment . . . . .	26
3. Experimental Results and Interpretation. . . . .	27
4. Calculation of Surface Energy. . . . .	28
5. Discussion . . . . .	36
IV. Lattice Defects . . . . .	40
A. Introduction . . . . .	40
B. Experimental . . . . .	40
C. Results and Interpretation . . . . .	41
D. Atomistic Calculation of Fault Energy . . . . .	43
E. Discussion . . . . .	44

V. Electrical Resistivity and Magnetic Hysteresis . . . . .	46
A. Introduction . . . . .	46
B. Experiment . . . . .	46
C. Results and Interpretation . . . . .	47
1. Phase Transformation and Magnetic Properties . . . . .	47
2. Defects and Magnetic Hysteresis. . . . .	47
3. Electrical Resistivity and Microstructure. . . . .	48
D. Discussion . . . . .	48
VI. Remarks. . . . .	51
Acknowledgement. . . . .	54
References . . . . .	55
Tables . . . . .	61
Appendix I . . . . .	67
Figure Captions. . . . .	70
Figures . . . . .	80

Defects, Phase Transformations and  
Magnetic Properties of Lithium Ferrite

Raja Kishore Mishra

Materials and Molecular Research Division, Lawrence Berkeley Laboratory  
and Department of Materials Science and Engineering,  
University of California, Berkeley, California 94720

ABSTRACT

Achieving suitable magnetic properties in ceramic ferrites through thermomechanical treatments rather than through varying the processing and fabrication parameters alone has been investigated. Ferrimagnetic lithium ferrite and some other spinel structure materials were chosen for this investigation. This work has involved an extensive characterization program of phase transformations and lattice defects.

A new crystallographic phase transformation in spinel has been observed in which the low temperature low symmetry space group  $F\bar{4}3m$  of  $MgAl_2O_4$  transforms to the "spinel" space group  $Fd\bar{3}m$  at  $\sim 450^\circ C$ . The in situ electron diffraction experiments suggest that this is a second order phase transformation.

The kinetics and crystallography of the solid state phase transition accompanying oxygen and lithium loss in  $LiFe_5O_8$  have been studied at  $1200^\circ C$  in air, oxygen ( $P_{O_2} = 760$  torr) and vacuum ( $P = 5 \times 10^{-5}$  torr) using high voltage electron microscopy.  $LiFeO_2$  was observed to nucleate and

grow in the  $\text{LiFe}_5\text{O}_8$  matrix and finally transform to spinel in all three atmospheres; but the kinetics of the transformation depend on the atmosphere. It is concluded that the amorphous phase that forms in the flux grown single crystals and not in the polycrystalline  $\text{LiFe}_5\text{O}_8$ , is not intrinsic to the Li-Fe-O system.

The surface topography accompanying the material loss is characterized in detail. The results suggest that the mass loss occurs from {111} surfaces, probably by a "surface energy" mechanism. The energies of these surfaces have been calculated and {111} surfaces are predicted to have the lowest energies. Most of the results of the calculation await experimental confirmation.

Structural defects in as-prepared and deformed lithium ferrite spinel were studied using transmission electron microscopy. Growth-type cation stacking faults and glissile dislocations on (110) planes were observed. From the measured value of the spacing between the partials  $\frac{1}{2}\langle 110 \rangle = \frac{1}{4}\langle 110 \rangle + \frac{1}{4}\langle 110 \rangle$ , the cation stacking fault energy was estimated to be about  $75 \text{ ergs/cm}^2$ . Atomistic calculations of the fault energies have been performed to explain the results.

Finally, magnetic property measurements showed that a dispersion of paramagnetic  $\text{LiFeO}_2$  particles in  $\text{LiFe}_5\text{O}_8$  matrix gives rise to increased squareness of the hysteresis curve, increased coercivity and a higher electrical resistivity. Annealing treatments of sintered  $\text{NiFe}_2\text{O}_4$  removed undesirable intra-granular  $(110)\frac{1}{4}\langle 110 \rangle$  cation stacking faults and improved the hysteresis loop parameters without affecting the electrical resistivity.



## I. INTRODUCTION

It is now accepted that if both process route-structures and structure-property relationships can be established, together they provide a firm basis for the control and development of materials properties. The primary role of microstructural characterization in development work is the specification of structures to optimise process route-property relationships. Such basic studies are necessary for more efficient utilization of available materials and development of newer ones at a time when we face a resource crisis.

Great success has been made in designing of metallic alloys for mechanical and physical applications through thermomechanical treatments to obtain suitable microstructures. This has been possible due to our understanding of the microstructural features, (such as defects and phases) and their effects on the material properties.<sup>(1)</sup> An analogous situation does not exist for ceramic materials, specifically because of the lack of detailed microstructural information on many ceramic systems. Even at present, the microstructure-sensitive properties of ceramic materials are controlled empirically by varying processing parameters so as to change porosity, grain-size, grain distribution, etc.<sup>(2)</sup> With the advent of ion thinning techniques to prepare electron transparent foils from ceramic materials, and high voltage electron microscopes to examine thicker specimens with less damage due to ionization, the study of microstructures in ceramic materials is now receiving more attention (e.g. refs. 3-5).

Structure-property relationships, the key to materials design, are yet to be established in almost all cases. The present work is concerned with the investigation of such relationships. It attempts to study the relationship between the microstructure and the magnetic properties in spinel structure ceramic ferrites. The emphasis is placed on (i) complete characterization of microstructural features obtained through well-defined thermomechanical treatments of the material, (ii) theoretical understanding of the origin of these features, and (iii) a critical evaluation of the direction of future research based on these findings. Lithium ferrite ( $\text{LiFe}_5\text{O}_8$ ), a soft ferrimagnetic spinel that finds application in microwave devices and computer memory cores, has been chosen as the ceramic material for this investigation.

Section II starts with a discussion of the crystal structure of  $\text{LiFe}_5\text{O}_8$  and the controversy surrounding the spinel space group.<sup>(6)</sup> Results of this investigation on the structure are presented. In addition, atomic arrangements on different crystallographic planes in spinel are included to facilitate the discussion of surfaces and defects in Sections III and IV. Section III includes the results of a detailed investigation of a high temperature precipitation reaction in  $\text{LiFe}_5\text{O}_8$ . Morphological and kinetic studies as well as the effect of material loss on the formation of the second phase are discussed in Section III(a). The material loss from the surfaces and the surface energies of the spinel are discussed in detail in III(b). A study of another important feature of the microstructure, viz., lattice defects, is presented in Section IV.

Structure-property relationships, the key to materials design, are yet to be established in almost all cases. The present work is concerned with the investigation of such relationships. It attempts to study the relationship between the microstructure and the magnetic properties in spinel structure ceramic ferrites. The emphasis is placed on (i) complete characterization of microstructural features obtained through well-defined thermomechanical treatments of the material, (ii) theoretical understanding of the origin of these features, and (iii) a critical evaluation of the direction of future research based on these findings. Lithium ferrite ( $\text{LiFe}_5\text{O}_8$ ), a soft ferrimagnetic spinel that finds application in microwave devices and computer memory cores, has been chosen as the ceramic material for this investigation.

Section II starts with a discussion of the crystal structure of  $\text{LiFe}_5\text{O}_8$  and the controversy surrounding the spinel space group.<sup>(6)</sup> Results of this investigation on the structure are presented. In addition, atomic arrangements on different crystallographic planes in spinel are included to facilitate the discussion of surfaces and defects in Sections III and IV. Section III includes the results of a detailed investigation of a high temperature precipitation reaction in  $\text{LiFe}_5\text{O}_8$ . Morphological and kinetic studies as well as the effect of material loss on the formation of the second phase are discussed in Section III(a). The material loss from the surfaces and the surface energies of the spinel are discussed in detail in III(b). A study of another important feature of the microstructure, viz., lattice defects, is presented in Section IV.

Both experimental and theoretical results are included for  $\text{LiFe}_5\text{O}_8$  as well as for some other spinel structure compounds for comparison. The work on magnetic and electrical properties is presented in Section V which also includes a discussion of the relationship between these properties and the microstructural features of the earlier sections. In the final section, the significance and importance of the results are evaluated.

## II. CRYSTAL STRUCTURE

### A. The Spinel Space Group

Spinel ferrites generally have the chemical formulae  $M^{+2}Fe_2^{+3}O_4^{-2}$  where  $M^{+2}$  is a divalent metal ion and the crystal structure is that possessed by the mineral spinel,  $MgAl_2O_4$ .<sup>(7)</sup>  $MgAl_2O_4$  spinel is cubic and its structure was determined first by Bragg<sup>(8)</sup> and Nishikawa<sup>(9)</sup>. The unit cell contains eight formulae units. The oxygen ions form, ideally, a face-centered cubic lattice. There are 64 tetrahedral (A) and 32 octahedral (B) interstices in the unit cell; out of these 8 and 16 respectively are occupied by cations. According to Bragg's results, the spinel space group is  $O_h^7(Fd3m)$  and the ionic positions are:

$$\begin{array}{l} \text{anion} \\ 32b \end{array} \quad \begin{array}{l} u, u, u; \bar{u}, \bar{u}, \bar{u}; \bar{u}, u, \bar{u}; \bar{u}, \bar{u}, u; \frac{1}{4} - u, \frac{1}{4} - u, \frac{1}{4} - u; \\ \frac{1}{4} - u, u + \frac{1}{4}, u + \frac{1}{4}; u + \frac{1}{4}, \frac{1}{4} - u, u + \frac{1}{4}; u + \frac{1}{4}, u + \frac{1}{4}, \frac{1}{4} - u; \end{array}$$

$$\begin{array}{l} \text{cation} \\ 16c \end{array} \quad 5/8, 5/8, 5/8; \quad 5/8, 5/8, 7/8; \quad 7/8, 5/8, 7/8; \quad 7/8, 7/8, 5/8;$$

$$\begin{array}{l} \text{cation} \\ 8f \end{array} \quad 0, 0, 0; \quad 1/4, 1/4, 1/4;$$

with the translations for an f.c.c. lattice

$$0, 0, 0; \quad 0, \frac{1}{2}, \frac{1}{2}; \quad \frac{1}{2}, 0, \frac{1}{2}; \quad \frac{1}{2}, \frac{1}{2}, 0.$$

When the oxygen parameter  $u = 3/8$ , packing is perfect and this corresponds to ideal structure. In real materials,  $u$  differs from 0.375, but only slightly; for example:  $u(\text{MgAl}_2\text{O}_4) = 0.387$ ,  $u(\text{LiFe}_5\text{O}_8) = 0.382$ .  $\delta$  in Section III denotes this difference.

The divalent ion  $\text{M}^{+2}$  may, in certain cases, be replaced by 'monovalent + trivalent' ions, while still retaining the spinel structure. Lithium ferrite is one such example with  $\text{M}^{+2}$  corresponding to  $(\text{Li}_{0.5}^+ \text{Fe}_{0.5}^{+++})$  in  $\text{Li}_{0.5}\text{Fe}_{2.5}\text{O}_4$ . If the trivalent ions exist on B-sites and the divalent ions on A-sites as in  $\text{MgAl}_2\text{O}_4$ , one gets a normal spinel. If eight 'divalent' ions are on B-sites and sixteen trivalent ions occur eight on B-sites and eight on A-sites as in  $\text{LiFe}_5\text{O}_8$ , one gets an inverse spinel. In many cases, an intermediate distribution exists and these are called mixed spinels.

More recently, questions have been raised about the space group of spinel. By a review of existing experimental data on infrared spectra and Debye-Waller factor, Grimes<sup>(10)</sup> first suspected that tetragonal symmetry through off-center displacements of octahedral ions might be present in spinel. His suggestion<sup>(10,11)</sup> that the space group of the spinel structure may not be  $\text{Fd}3\text{m}$  but  $\text{F}\bar{4}3\text{m}$  has been supported by recent electron and x-ray diffraction evidence, in which, the presence of  $hk0$  reflections with  $h+k=4n+2$  in  $\text{MgAl}_2\text{O}_4$ <sup>(12)</sup> and some thiospinels,<sup>(13)</sup> have been found at room temperature. However, in other compounds with the spinel structure, such as  $\text{LiFe}_5\text{O}_8$ , the room temperature electron diffraction patterns of the  $\langle 100 \rangle$  reciprocal lattice sections (Figure 1) do not exhibit these forbidden reflections, showing that the structure

has the originally proposed space group  $Fd3m$  (18). Neutron diffraction experiments from magnetite by Samuelson (14) and x-ray diffraction from  $CuCo_2S_4$  by Williamson and Grimes (15), also support the result that the space group of  $Fe_3O_4$  or  $CuCo_2S_4$  is  $Fd3m$  at room temperature. In the present study a structural phase transition that transforms the space group of  $MgAl_2O_4$  to  $Fd3m$  at high temperature is observed.

Figures 2a and 2b show the symmetrical  $\langle 100 \rangle$  selected area electron diffraction pattern from a stoichiometric  $MgAl_2O_4$  spinel single crystal grown by Czochralski method. The electron transparent specimen was prepared from the bulk crystal by ion thinning and examined in the Phillips EM301 transmission electron microscope operating at 100 kV. Figure 2a shows the presence of  $hk0$  spots with  $h+k=4n+2$  (i.e. 200, 420 etc.). The integrated intensity of the 200 spots as measured from microdensitometer traces is less than (1/1000)th of that of the 400 spots. On heating the specimen in the hot stage of the electron microscope to a temperature close to  $450^\circ C$ , the "forbidden" spots disappear, as is evident in figure 2b taken from the same area of the foil ( $\sim 2 \mu m$  in diameter). In order to prove that the extra reflections are representative of structural changes and not double diffraction or other effects, Figures 3a-d show selected area diffraction patterns taken from the foil near  $\langle 100 \rangle$  orientation tilted so as to excite the 400 reflection after the temperature changes as shown. The heating sequence Fig. 3a-c shows the disappearance of the 200 reflection near  $450^\circ C$ , and the reflection subsequently reappears upon cooling, as in Figure 3d. Close examination of the corresponding images both in bright field and

dark field using the 200 and 400 reflections does not show any changes in microstructure nor morphological features. This strongly suggests that the observed symmetry change is not accompanied by a solid state phase transition involving nucleation and growth, by which two phases can coexist.

Assuming that the space group of  $\text{MgAl}_2\text{O}_4$  at room temperature is  $\overline{F}43m$  as suggested by Grimes, (10,11) this experimental result suggests that the nonequivalent octahedral sites of the room temperature  $\overline{F}43m$  phase become statistically equivalent at higher temperature due to thermal vibration. The transformation can be accomplished without any long range diffusion. Application of Landau's theory of a second order phase transition (16) shows that it is possible for the transition  $\overline{F}43m \rightarrow \text{Fd}3m$  to occur by either a first or a second order transformation (17). However, the experimental evidence that no microstructural changes are resolved within the limits of the present experimental technique, suggests that the transformation is actually one of second order. It is possible that the other spinel structure compounds that do not give rise to  $hk0$  reflections with  $h+k=4n+2$  at room temperature may also transform and show these reflections at lower temperatures. Hence it may be that this transformation could be a general one for oxide spinels and thiospinels.

#### B. Atomic Arrangements

Whereas the octahedral ions in  $\text{Fd}3m$  would be at the geometrical center of the anion octahedra, they are shifted off-center (6) by distances of about  $0.002\text{\AA}$  to  $0.004\text{\AA}$  in  $\overline{F}43m$ . For the discussion of



the atomic arrangement on various crystallographic planes, we neglect this difference and assume that the symmetry is  $Fd\bar{3}m$ . Then, in the spinel  $AB_2O_4$ , the projections of atomic arrangements on  $\{100\}$ ,  $\{110\}$  and  $\{111\}$  planes are as shown in Figures 4, 5(b) and 6.

Along a  $\langle 100 \rangle$  direction, the spinel unit cell consists of 8 layers,  $a_0/8$  apart. The successive layers have compositions ...  $/A/B_2O_4/A/B_2O_4/A/B_2O_4/...$ . The two dimensional periodicity of the A plane can be described by choosing a coordinate system and square unit cell of sides  $a_0/2$  as shown in Figure 4. The two dimensional reciprocal lattice corresponding to this cell is given by

$$\vec{g}_{1m} = 2\pi/a_0 (\sqrt{2} l \hat{x} + \sqrt{2} m \hat{y}) \quad (1)$$

The layer corresponding to  $B_2O_4$  can be constructed by superimposing two B-planes and four oxygen planes on each other such that all planes have identical periodicity; but the origins of the elementary planes are, for example, at  $0,0$ ;  $0, \sqrt{2}/4$ ;  $-\sqrt{2}/8, -\sqrt{2}/8$ ;  $\sqrt{2}/8, -\sqrt{2}/8$ ;  $\sqrt{2}/8, \sqrt{2}/8$ ; and  $-\sqrt{2}/8, \sqrt{2}/8$  (in units of  $a_0$ ) respectively in Figure 4. This description of atomic arrangements will be used in Sections III and IV for purposes of performing atomistic calculations.

Similarly, the atomic arrangements on  $\{110\}$  planes can be described by a two dimensional unit cell whose reciprocal lattice vector is

$$\vec{g}_{1m} = 2\pi/a_0 [1 \hat{x} + \sqrt{2} m \hat{y}] \quad (2)$$

with respect to the coordinate system shown in Figure 5(b). Along  $\langle 110 \rangle$ , the unit cell contains 8 layers,  $\sqrt{2} a_0/8$  apart, and the composition of successive layers is...  $/BO_2/ABO_2/BO_2/ABO_2/\dots$ . With this periodicity,  $BO_2$  layer can be constructed from two B-planes and four oxygen planes as before. The  $ABO_2$  layer will have two additional A planes. The origins of these elementary planes with the prescribed periodicity is apparent from Figure 5(b).

The Atomic arrangements on  $\{111\}$  planes are more complex and have been discussed in detail by Hornstra.<sup>(18)</sup> Along  $\langle 111 \rangle$ , the spinel consists of a 24 layer stacking of cations and anions with an inter-layer spacing of  $a_0\sqrt{3}/24$ . Figure 6 shows the stacking sequence and the ionic positions on  $\{111\}$  planes in Hornstra's extended ...ABC... notation for the spinel  $AB_2O_4$ . Choosing the basic two dimensional unit cell as the one corresponding to the periodicity on the least populated layer (any plane from mixed layer<sup>(18)</sup>) the corresponding reciprocal lattice vector  $\vec{g}$  with respect to the coordinate system in Figure 6 is given by:

$$\vec{g}_{1m} = 4\pi/a_0 [ (1+m) \hat{x}/\sqrt{2} + (1-m)\hat{y}/\sqrt{6} ] \quad (3)$$

The kagomè layers<sup>(18)</sup> (or oxygen layers), then consist of three (or four) elementary planes.

The present atomistic calculations will be limited to these three crystallographic planes only, and hence the atomic arrangements on other planes will not be discussed. However, this method can be extended to describe the atomic positions on any other plane.

### III. PHASE DECOMPOSITION, MATERIAL LOSS AND SURFACE ENERGY

#### A. Material Loss and a High Temperature Phase Transformation

##### 1. Introduction

As already noted, lithium ferrite is a ferrimagnetic material with many attractive properties<sup>(19)</sup>. Its main asset is a high Curie temperature of about 650°C. With proper preparation, high electrical resistivity<sup>(20)</sup>, a square hysteresis loop<sup>(21)</sup>, a low resonance line width<sup>(22)</sup> can also be obtained. These properties are however, strongly dependent on the history of the sample. It is generally assumed that this material loses appreciable amounts of oxygen and lithium above 1000°C where it would be desirable to sinter the material. It is this material loss that has limited the application of pure and doped lithium ferrites and hence the phenomenon has received the attention of a number of investigators<sup>(23-31)</sup>. In all these studies the authors have used powder compacts with  $\text{Fe}_2\text{O}_3$  and  $\text{Li}_2\text{CO}_3$  as starting materials, sometimes with  $\text{LiFeO}_2$  as an intermediate product. The resulting powder compacts need to be prepared at low temperature, at times with the help of a packing powder<sup>(25)</sup>, in order to prevent material losses prior to the actual measurements. Hence these powder aggregates often contain traces of unreacted  $\text{Fe}_2\text{O}_3$  and (or)  $\text{LiFeO}_2$ . In addition, the study of the material loss in lithium ferrite is hampered by the following:

(i) Chemical analysis for lithium is difficult and expensive, (ii) Phase identification using X-ray diffraction is also difficult, especially the detection of small amounts (up to 20%) of the  $\text{LiFeO}_2$  phase because its interplanar spacings are very close to those in  $\text{LiFe}_5\text{O}_8$  so that the

X-ray diffraction peaks overlap.<sup>(27)</sup> Salmon and Marcus<sup>(29)</sup> postulated that  $\text{LiFeO}_2$  could be formed as an intermediate phase during the decomposition of the spinel. Evidence for the occurrence of  $\text{LiFeO}_2$  phase near the surface of a sample with excess lithia, has been obtained by Bondyopadhyay and Fulrath.<sup>(25)</sup>

In the present work the high temperature material loss in lithium ferrite has been studied using single crystals, to ensure that the starting material is single phase. The microstructures resulting from the material loss have been characterised in detail using high voltage transmission electron microscopy. The kinetics and the mechanism of the phase transformations accompanying the material loss have also been studied. It may be noted here that this transformation is different from the extensively studied<sup>(32,33)</sup> order-disorder transformation in  $\text{LiFe}_5\text{O}_8$  where the lithium ions and iron ions on the octahedral sites order below  $750^\circ\text{C}$ .

## 2. Experimental Procedure

Flux grown single crystals of lithium ferrite spinel with a maximum dimension of 2 cm were obtained from Airtron Litton Industries. These crystals contained particles of vitrified flux trapped during growth. The portion of the flux trapped in open pores could simply be removed by heating the crystal to  $750^\circ\text{C}$ , where these flux particles become liquid. Semi-quantitative spectrographic analysis of such a crystal is given in Table I. The flux contained  $\text{PbO}$  and  $\text{B}_2\text{O}_3$ ; these oxides also showed up in the chemical analysis but some of it is due to the flux particles trapped in closed pores. Quantitative chemical

analysis revealed that the crystals were slightly deficient in Li with a Fe/Li ratio of  $5.17 \pm .27$  as determined by flame photometry. The starting material had a homogeneous single phase spinel microstructure as revealed by TEM. From X-ray measurement the lattice parameter was found to be 8.33 Å. The temperature of the heat treatments was kept constant at 1200°C for all runs. The effects of three atmospheres; air, 1 atm. O<sub>2</sub> and a vacuum of  $5 \times 10^{-5}$  torr were investigated. It was expected that gradients in composition would occur throughout a crystal as oxygen and lithium were lost from the surface. Thin foils from different depths of the specimen were prepared to study the reaction sequence in the interior of the crystals. In order to follow the microstructural changes with annealing time, care was taken to prepare a sample for observation in the electron microscope at fixed distances from both surfaces of a thin slice of crystal. These slices were all ground to a thickness of 0.015 inch with faces nearly parallel to {110}. These slices were heat treated for different times (see Table II) in the three different atmospheres; care was taken that both faces were exposed to the environment during heat treatment. Specimens for electron microscopy were prepared from the heat treated samples by drilling a small disc from the center of the sample, mechanically polishing the disc to a thickness of 8µm and finally by ion thinning.

Specimens prepared in this way exhibited some surface irregularities<sup>(34)</sup>, but all the artifacts due to the specimen preparation method could easily be identified since these were present in all specimens. All the microscopy was done using a HU-650 transmission electron microscope operating at 650 kV.

Some sintered polycrystalline samples were prepared starting from  $\text{Li}_2\text{CO}_3$  and  $\text{Fe}_2\text{O}_3$  (processing details can be found elsewhere)<sup>(25)</sup>.

These were sliced and heat treated. Specimens prepared from them were examined in the microscope under the same conditions.

The iron and lithium contents in the annealed and unannealed samples were determined by semi-quantitative chemical analysis for a few specimens and are listed in Table III.

### 3. Results and Interpretation

The mechanism of the phase transitions as observed in the HVEM are the same in air-annealed, vacuum annealed, and oxygen annealed samples. However, there are significant differences in the kinetics as revealed by a comparison of the observations on samples aged in air, oxygen and vacuum under otherwise identical conditions.

The results of the air-annealed single crystals are presented first, followed by a discussion of the additional features seen in the oxygen-annealed and vacuum annealed crystals. Results of the experiments on polycrystalline samples are then presented at the end of this section.

#### (a) Transformation in air

Technologically air is the most important atmosphere during processing and hence the observations in air are discussed below in detail. For convenience, the sequence of events are discussed in terms of the three different stages of transformation, as shown schematically in Figure 7.

(i) The early stage: (Stage ~) This corresponds to the interval when precipitates of  $\text{LiFeO}_2$  form. After 15 minutes, the microstructure

near the center of the heat-treated discs consists of coherent octahedral shaped particles of  $\text{LiFeO}_2$  dispersed randomly in the spinel matrix as shown in Figure 8. Particles with an average dimension of  $2500 \text{ \AA}$  or less remain coherent with the matrix. The precipitate-matrix interfaces are parallel to  $\{111\}$  planes and there is negligible strain contrast around these particles. Lattice fringe images from a specimen containing octahedral precipitates is shown in Figure 9. Accounting for the thin slab of the specimen<sup>(35)</sup> contributing to the image, it can be seen that the spinel periodicities are retained to the very edge of the precipitate, indicating that the precipitate-matrix interface remains atomistically flat when the precipitates are coherent. However, this is not true for semicoherent precipitates as can be seen in Figure 10. The spinel periodicities contain ledge-like fringes near the interface.

The octahedral particles grow in size and become semicoherent with the matrix in regions nearer to the disc surface. The structure of the new phase is determined by examining the electron diffraction patterns from the precipitate and the matrix. Figure 11 shows the SAD patterns from a) matrix only, b) precipitate and matrix, c) precipitate only, and d) the  $[110]$  reciprocal lattice sections of the precipitate and the matrix (including the spots that may arise due to double diffraction) superimposed on each other. The second order spots of the matrix coincide with the first order spots of the precipitate. The orientation relationship can be written as

$$(\bar{1}\bar{1}0)_m // (\bar{1}\bar{1}0)_p$$

$$[110]_m // [110]_p, [001]_m // [001]_p.$$

i.e. Here is perfect matching of parallel crystallographic planes and directions. BF and DF images taken from the first and second order spots of a  $\langle 220 \rangle$  systematic row are shown in Figure 12. From the figure it is apparent that spot 1 on the systematic row arises from the matrix while spot 2 arises from both the matrix and the precipitate. This leads to the conclusion that the precipitate has a cubic structure with lattice parameter which is almost exactly half of that of the matrix. From X-ray measurements, the room temperature lattice parameter of  $\text{LiFe}_5\text{O}_8$  spinel is 8.33 Å. On the basis of ASTM data on (Li,Fe,O) compounds and the results of earlier investigations<sup>(26,29)</sup>, the new phase here is inferred to be lithium ferrate ( $\text{LiFeO}_2$ ) with the rock-salt structure and a room temperature lattice parameter of 4.14 Å. The result is further confirmed by the fact that diffuse scattering arising due to short range order in  $\text{LiFeO}_2$ <sup>(36)</sup> precipitates is observed in Figure 11c and less clearly in Figure 11b. The lattice fringe images from the precipitates show microdomains<sup>(37,38)</sup> with APB's as in Figure 10.

The critical size of the growing  $\text{LiFeO}_2$  precipitates when they lose coherency with the matrix is calculated below. Let  $\epsilon_s$  be the self-energy<sup>(39)</sup> of a prismatic dislocation loop of Burgers vector  $b$ ,  $\epsilon_i$  be the energy of interaction<sup>(39)</sup> between the precipitate and the



loop and  $\epsilon_e$  be the elastic strain energy<sup>(40)</sup> before the dislocation loop is introduced. It will be favourable to introduce a dislocation loop around a spherical precipitate of radius  $r$ , when

$$\epsilon_e(r) \lesssim \epsilon_i(r) + \epsilon_s(r) \quad (4)$$

It may be noted here that Brown et al.<sup>(39)</sup> do not account for  $\epsilon_e(r)$  in their discussion of coherency loss.

Equation (4) can be written as:

$$\frac{2}{9} \cdot \mu \cdot \frac{4\pi}{3} r^3 \left( \frac{1+\nu}{1-\nu} \right) \epsilon^2 \lesssim \frac{\mu b^2 r}{2(1-\nu)} \left[ \ln \frac{8r}{r_c} - 1 + \frac{3-2\nu}{4(1-\nu)} \right] - 4\pi\mu b \epsilon r^2 \quad (5)$$

With the core radius of the dislocation  $r_c \approx 0.4b$ ,<sup>(41)</sup>  $R(= r/b)$  must satisfy the equation

$$2.37\pi(1+\nu)\epsilon^2 R^2 + 32\pi(1-\nu)\epsilon R - 8 - (3-2\nu)/(1-\nu) \lesssim 4 \ln R \quad (6)$$

The strain  $\epsilon$  is given by<sup>(42)</sup>

$$\epsilon = \frac{3\kappa \Delta}{3\kappa + 2E/(1+\nu)} \quad (7)$$

$\kappa$  is the bulk modulus of the precipitate,  $E$  and  $\nu$  are respectively the Young's modulus and Poisson's ratio of the matrix, and  $\Delta$  is the lattice misfit defined below in Equation (10). The Reuss average<sup>(41)</sup> values for  $\nu$ ,  $E$  and  $\kappa$  are 0.3169,  $1.9 \times 10^{12}$  dynes/cm<sup>2</sup> and  $5.5 \times 10^{11}$  dynes/cm<sup>2</sup> respectively. Thus,  $R$  is the solution of the equation

$$1.25 \times 10^{-5} R^2 + 3.88 \times 10^{-2} R - 2.86 \approx \ln R \quad (8)$$

Hence, precipitates with radii  $\lesssim 1162$  Å will be coherent with the matrix. This is more or less consistent with the present observations, though the observed size of the octahedral precipitates is somewhat larger. If there will be an activation barrier for generating the loop, the coherent precipitates may grow larger than the size calculated above. Assuming that an activation barrier will be overcome, once the particle reaches a size large enough so that two loops spaced  $D$  apart will be needed to relieve the strain; the particles will be coherent unless

$$\epsilon_e(r') \approx 2[\epsilon_i(r') + \epsilon_s(r')] + \epsilon_D(r') \quad (9)$$

Here  $\epsilon_D(r')$  is the energy of interaction<sup>(41)</sup> of the two loops of radii  $r'$  around the spherical precipitate of radius  $r$ . Complete analysis gives a critical value of  $r$  higher than the previous one. However, whether such a process occurs or not can only be resolved by in situ observation of coherency loss in thin foils.

The growing precipitates have two different kinds of morphologies. Some precipitates are highly elongated while other remain nearly

spherical. Figure 13a shows few isolated spherical precipitates which are semicoherent with the matrix and are connected by matrix dislocations, and Figure 13b shows two of the growing semicoherent precipitates as they coalesce. Precipitates nucleated heterogeneously on dislocations are shown in Figure 13c. Figure 13d shows an elongated precipitate resulting from the coalescence of these particles. Precipitates as long as  $25\mu$  have been observed compared to the lateral dimensions of about  $1\mu\text{m}$ . Figure 14 shows part of an elongated precipitate in two different diffracting conditions. The semicoherent interface consists of a network of dislocations with Burgers vector  $a/2 \langle 110 \rangle$ . Dislocations visible in Figures 14a and b have  $1/2[1\bar{1}0]$  and  $1/2[101]$  Burgers vectors, and the average separations between the dislocations are  $1100\text{ \AA}$  and  $640\text{ \AA}$  respectively. Assuming the interface as fitting together of two crystals of slightly different lattice parameters but identical orientations, we may determine the misfit parameter  $\delta$  from Brook's<sup>(43)</sup> relation

$$\delta = \frac{2(a_1 - a_2)}{a_1 + a_2} = \frac{b}{D} \quad (10)$$

where  $b$  is the component of the Burgers vector in the plane of the interface,  $D$  is the average distance between dislocations and  $a_1, a_2$  are the lattice parameters of the two crystals. For  $D = 1100\text{ \AA}$  and  $\vec{b} = 1/2[110]$  for the edge dislocations on  $(110)$  as in Figure 14a,  $\delta = 5.4 \times 10^{-3}$ . For  $D = 640\text{ \AA}$  and  $1/2[001]$  as component of  $\vec{b}$  on  $(110)$  along  $[001]$  in Figure 6b,  $\delta = 6.5 \times 10^{-3}$ . Thus the average value of

$\delta$  as measured from the misfit dislocation spacing is  $5.95 \times 10^{-3}$  which compares very well with the value of  $\delta$  obtained from the values of the lattice parameters of  $\text{LiFeO}_2$  and  $\text{LiFe}_5\text{O}_8$ .

A rough estimate shows that the volume fraction of the  $\text{LiFeO}_2$  is about 10-12%.

(ii) The Intermediate Stage (Stage II): With longer aging times, the microstructure near the center of the disc consists of large semi-coherent  $\text{LiFeO}_2$  particles in  $\text{LiFe}_5\text{O}_8$ . These have characteristics similar to the ones discussed earlier for Stage I particles. In regions near the surface of the heated crystal one sees a single phase microstructure. The single phase is a spinel phase as confirmed by the selected area electron diffraction pattern. The thin foils show a high density of small angle tilt boundaries with numerous dislocations in between. Figure 15a shows one such boundary and Figure 15b is the SAD pattern obtained with the selected area aperture placed over the boundary to include portions of both the grains. From this pattern, the misorientation is found to be about three degrees about the  $[\bar{1}\bar{1}0]$  direction between the two grains. The dislocations have a Burgers vector of  $1/2\langle 110 \rangle$ .

(iii) The Final Stage (Stage III): As shown schematically in Figure 7, in Stage III, the entire crystal has a polygranular single phase microstructure. The details are similar to the features of the near-surface regions of Stage II, which were discussed above.

On reaging such a sample at  $750^\circ\text{C}$  (where lithium ferrite shows an order-disorder transition), all the superlattice reflections<sup>(44)</sup> of ordered lithium ferrite are visible from all grains. Since the ordering

is due to rearrangement of lithium atoms in the octahedral interstices, this proves the presence of Li throughout the material.

On further aging (>3 hrs), a microstructure with opaque particles (~1000 Å in diameter) dispersed in spinel as in Figure 16a is obtained near the center of the sample. The particle contrast is always dark in bright field as well as in dark field images, and the contrast does not change with  $\vec{g}$ , sign of  $s$ , nor thickness of the foil. This suggests that the particles are amorphous and very dense. Although one would expect to see diffuse rings from amorphous particles, the low volume fraction ( $\leq 1\%$ ) of this phase does not contribute enough intensity to the electron diffraction pattern. No glassy particles are present near the crystal surface.

(b) Transformation in Vacuum

As noted earlier, the features of the phase transformation in vacuum are similar to those in air, with the exception of the reaction kinetics. In fact the initial transformation stage is not observed in the thin platelet samples even for the shortest annealing times. Stages II and III are similar to those in air. An additional observation in the vacuum annealed specimens is that the amorphous particles form after shorter aging times. In Stage II, the amorphous particle density increases very rapidly and reaches a maximum. For very long aging times the amount of amorphous particles decreases. The amorphous particles have a nearly spherical shape, although in a few cases these are elongated. There is no detectable strain in the matrix around these particles. Figure 16b shows the preferential growth of the amorphous particles at the  $\text{LiFe}_5\text{O}_8$ - $\text{LiFeO}_2$  interface in Stage II of the

transformation. As can be seen in Figure 16b, no amorphous inclusions are present in the  $\text{LiFeO}_2$  phase.

(c) Transformation in Oxygen

Here again, the morphology of the transformation is the same as that in air except for the kinetics, but unlike the vacuum-annealed case, the reaction is very slow. The two phase microstructure corresponding to Stage II is shown in Figure 17 where part of an elongated semicoherent precipitate is imaged. The misfit as measured here corresponds to the value of  $\delta$  obtained earlier. The amorphous phase forms only for very long annealing times. Roughly 10-12% of  $\text{LiFe}_5\text{O}_8$  transforms to  $\text{LiFeO}_2$ .

(d) Transformation in Polycrystalline Material

The sintered polycrystalline material is single phase spinel with the largest grain size of about  $5\mu$ . This was annealed in vacuum for times corresponding to Stage II and Stage III of the transformation. Of special significance is the observation that, even after heating for very long times, no amorphous phase appears unlike the vacuum-annealed single crystals. Figure 18 taken from foils near the center of the crystal, shows  $\text{LiFeO}_2$  particles form in the grain interior as well as on the grain boundary. The role of the grain boundaries in the transformation kinetics has not been systematically investigated in this study.

#### 4. Discussion

(a) Formation and Growth of  $\text{LiFeO}_2$  Particles

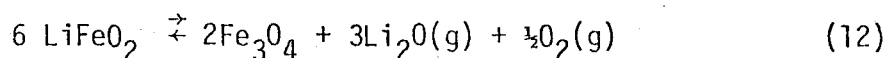
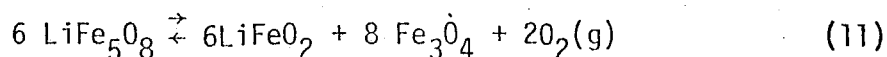
$\text{LiFeO}_2$  has the rock salt structure with oxygen at the anion sites and a random distribution of Li and Fe at the cation sites<sup>(45)</sup>. The

distributions of anions on the closepacked  $\{111\}$  planes in  $\text{LiFeO}_2$  and  $\text{LiFe}_5\text{O}_8$  are almost identical (separation between oxygen ions are 2.927 Å and 2.945 Å respectively). The cations in  $\text{LiFe}_5\text{O}_8$  are arranged in alternate Kagomé and mixed layers<sup>(18)</sup> where as cations in  $\text{LiFeO}_2$  are arranged in close packed layers. From the ASTM data file, the misfit between the two lattices is only 0.6% and thus the strain energy due to the precipitates is quite small. The formation of octahedral shaped precipitates with  $\{111\}$  planes as faces suggests that the shape is determined by the anisotropy of the interfacial energy. Undoubtedly  $\{111\}$  interfaces in this case have the lowest surface-free energy. For a given volume, tetrahedral precipitates have nearly 20% more area than octahedral precipitates and thus, for negligible strain energy, octahedral particles are preferred. It may be noted that larger strains may change the morphology<sup>(40)</sup> of the particles as seen in the case of wüstite precipitates in  $\text{CoFe}_2\text{O}_4$ <sup>(46)</sup>. Since the anion positions remain unchanged in the precipitation process, and since cations are very mobile in the spinel structure<sup>(47)</sup>, the formation and growth of  $\text{LiFeO}_2$  particles can be viewed simply as a process of diffusion and redistribution of cations. The phase transformation is discussed further below.

As in Figure 18,  $\text{LiFeO}_2$  Particles also form inside the grains in a polygranular  $\text{LiFe}_5\text{O}_8$  sample. Because of the high diffusivity of the cations in the spinel structure, it may be possible to suppress heterogenous precipitation on grain boundaries to obtain a homogeneous dispersion of precipitates, if desired.

b. Nature of the Phase Transformations during Material Loss

The results described earlier can be interpreted by considering the reaction postulated by Salmon and Marcus<sup>(29)</sup>:



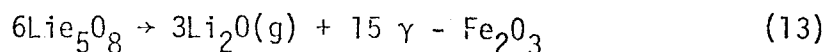
$\text{LiFeO}_2$  would then be an intermediate product in the decomposition. If reactions (11) and (12) occur at an equal rate i.e. if  $\text{LiFeO}_2$  decomposes at the same rate as it is being formed, then one should find it only at the surface of the sample. It is clear from the above observations that this is not the case. It is possible to explain the present results if one assumes that reaction (11) proceeds faster than reaction (12); or, in more general terms, if oxygen is lost at a higher rate than lithia. As a result an excess of cations or alternatively an oxygen deficit is created within the spinel phase, causing the precipitation of the cation rich  $\text{LiFeO}_2$  phase. The precipitation process starts at first at the surface. As the oxygen loss at the surface continues, the oxygen deficiency is gradually transmitted to the interior of the sample through diffusional processes, the nature of which are not known, but need not be specified here. As a result, precipitation occurs throughout the sample (Stage I). However, near the surface, the oxygen deficiency is more severe, and hence at this stage there is more  $\text{LiFeO}_2$  present near the surface than in the interior. On the other hand, the



loss of lithia is also gradually felt. This causes the dissolution of the lithia rich  $\text{LiFeO}_2$  phase, again starting first near the surface. In Stage II (Figure 7) the outer surface layers lose enough lithia so that the  $\text{LiFeO}_2$  dissolves again leaving behind the interface dislocations introduced during the precipitation process. Ultimately, in samples which are thin enough, reaction (12) catches up with reaction (11) even at the center of the sample and only the spinel phase remains with the remnants of the interface dislocations and boundaries (Stage III). This spinel phase still contains some lithium depending on the atmosphere. This point has been investigated by Tretyakov et al<sup>(31)</sup>. In the present case, when annealed in air, enough lithium is still present to observe the order-disorder reaction as described earlier. This is also apparent from the chemical analysis results given in Table III. It is clear that in thick crystals, Stage III, may never be reached and that a two phase state is obtained in the interior of the sample. An example is shown in Figure 19 taken from the center of a crystal, 2 cm in diameter annealed in vacuum for 10 hours. The interior of the crystal contains  $\text{LiFeO}_2$  precipitates several microns in diameter. It is important to realize this when processing lithium-ferrite. In polycrystalline material, the lithium ferrite can form as precipitates within the spinel grains (Figure 18).

In summary, the phase transformations observed during the material loss of lithium ferrite are due to the competition between the oxygen loss and the lithia loss. These phase transformations can be understood by plotting the local composition at a constant depth in the sample as

a function of time in the  $\text{Fe}_3\text{O}_4$ - $\text{Fe}_3\text{O}$ - $\text{Li}_2\text{O}$  phase diagram as determined by Tretyakov et al. (Figure 20). Schematically the path ABC will be followed, where branch AB is due to the oxygen loss at constant lithia content, and branch BC is due to the lithia loss at constant  $\text{Fe}^{2+}$  content. Regarding the reactions by Salmon and Marcus, the remark needs to be made that the  $\text{LiFeO}_2$  is not strictly an intermediate product in the sense that it is a necessary step in the lithia loss process, as this phase is not found near the surface of the samples in Stage II. Lithia loss can take place independently from the oxygen gas loss through the reaction:



The  $\gamma$ - $\text{Fe}_2\text{O}_3$  forms a solid solution with the lithium ferrite. Nevertheless, reactions (11) and (12) can still provide a useful framework for the discussion of the material loss processes.

(c) The Amorphous Particles:

The absence of any amorphous particles in sintered polycrystals in spite of their presence in the flux-grown single crystals rules out the possibility that this phase is characteristic of the Li-Fe-O system. The chemical analysis of single crystal  $\text{LiFe}_5\text{O}_8$  as given in Table I shows the presence of some glass forming impurities retained from the flux and most probably the amorphous phase is a low melting complex oxide of some of these impurities. The gradient in their distribution

with the depth of the foil indicates that the phase is very volatile. No attempt has been made in this investigation to characterize the amorphous phase further.

## B. Material Loss and Surface Energy of Spinel

### 1. Introduction

The effect of material loss on phase transformations has already been discussed. The gaseous species formed during reactions (11) and (12) escape from the surfaces of the specimen. In the present section, the surface topography accompanying the material loss is studied. The surface energies have also been estimated to explain the observations. Possible mechanisms governing the material loss are discussed.

### 2. Experiment

Single crystals of  $\text{LiFe}_5\text{O}_8$  grown by the flux method were obtained from Airtron-Litton Company. One millimeter thick discs with faces parallel to  $\{111\}$  and  $\{110\}$  planes were cut from these bulk single crystals. These were heated at  $1200^\circ\text{C}$  in air, flowing oxygen at one atm. pressure and vacuum ( $10^{-5}$  torr) as in III.A.2. for a range of intervals. The surfaces of these discs were gold coated and examined in JSM-U3 scanning electron microscope. Also, samples were etched in phosphoric acid at  $195^\circ\text{C}$  for ~15 minutes, gold coated, and examined in the SEM.

To ascertain whether the mass loss results for  $\text{LiFe}_5\text{O}_8$  were characteristic of the spinel structure or peculiar to the chemical composition of the  $\text{LiFe}_5\text{O}_8$  only, Czochralski grown  $\text{MgAl}_2\text{O}_4$  were also heated at  $1600^\circ\text{C}$  under similar atmospheric conditions and examined in the SEM.

### 3. Experimental Results and Interpretation

Figure 21 is a scanning electron micrograph taken from the (111) surface of a  $\text{LiFe}_5\text{O}_8$  specimen heated in air for three hours. On heating, the surface has become porous with a spongelike topography. As can be seen in this micrograph, the bottom of the pores is almost flat, and faceting is insignificant compared to that in Figure 22. Figure 22 is the scanning micrograph of a surface which was initially parallel to (110), and has been heated for three hours in air. By measuring the angles between the various facet directions and comparing them with the angles between crystallographic directions, a set of self-consistent indices have been assigned to these directions. This conclusion has been confirmed by careful Laue diffraction experiments. The marked crystallographic direction in Figure 22 correspond to the lines of inter-section of {111} planes with the (110) surface. Figures 21 and 22 thus suggest that material loss occurs preferentially from {111} planes giving flat surfaces (apart from the spongy nature) if the initial surface is an {111} surface, and a growth step structure if it is not an {111} surface.

Figure 23 is taken from the {110} surface of a sample heated for fifteen minutes in vacuum. (This corresponds to Stage II of the phase transformation of III.A.) For such a short heating time, the surface topography is primarily due to initiation of material loss. In the area near A, one can notice the development of a steplike structure. The results from vacuum and oxygen annealed  $\text{LiFe}_5\text{O}_8$  surfaces and  $\text{MgAl}_2\text{O}_4$  surfaces exhibit features identical to the ones just described.

#### 4. Calculation of Surface Energy

Surface energy, defined as the excess of energy on the free surface compared to the bulk, is an important parameter of a ceramic material. It controls many chemical and physical processes such as sintering, material loss, adhesion, colloid dispersion, diffusion bonding, crack nucleation and growth, etc.<sup>(48)</sup>. A precise knowledge of the surface energy will be very useful in estimating and optimising processing and properties of ceramic materials. Unfortunately, due to various theoretical and experimental difficulties,<sup>(49)</sup> a precise value for this parameter is not easily obtained. It has been measured only in a very limited number of materials<sup>(50)</sup> and has been theoretically calculated for solids with simple structures<sup>(50)</sup>. Nevertheless, surface energies obtained by atomistic calculations compare satisfactorily with experimental values<sup>(51)</sup>. Extensions of the calculations to complex ionic solids such as spinels have been lacking due to insufficient knowledge about the repulsive potential functions. Recently, it has been possible to estimate<sup>(52)</sup> some of these potential functions for  $\text{MgAl}_2\text{O}_4$  from infrared and Raman spectra. Thus, it is now possible to estimate surface energies of  $\text{MgAl}_2\text{O}_4$  and is presented below. Also, for comparison, the surface energy values for  $\text{MgAl}_2\text{O}_4$ ,  $\text{NiFe}_2\text{O}_4$ ,  $\text{LiFe}_5\text{O}_8$ ,  $\text{Fe}_3\text{O}_4$ , etc. have been estimated from elastic constants following Gilman's<sup>(51)</sup> method. It is seen that the surface energies of spinel ferrite and  $\text{MgAl}_2\text{O}_4$  spinel are very similar.

(a) Atomistic Calculation of Surface Energy

(i) Method of Calculation: For an ionic solid, the surface energy  $\gamma$ , can be written as a sum of two parts:

$$\gamma = \gamma_0 + \Delta_\gamma \quad (14)$$

$\gamma_0$  is the energy of the surface when the ions are held rigidly everywhere just as the ions in the bulk, and  $\Delta_\gamma$  is a small correction that takes into account relaxation of the surface. Consider a semi-infinite crystal bound by a planar surface and choose two of the fundamental translation vectors  $\vec{a}$  and  $\vec{b}$  in a plane parallel to the surface with the third fundamental translation vector  $\vec{c}$  normal to it outwardly. In the rigid lattice approximation,  $\gamma_0$  of the surface, defined by the vectors  $\vec{a}$  and  $\vec{b}$ , is the negative of the interaction energy of the crystal<sup>(53)</sup> with a stack of lattice cells sticking out of it along  $\vec{c}$  divided by twice the contact area  $|\vec{a} \times \vec{b}|$ . The atomic re-arrangement and the electronic polarisation tend to minimize this energy, and hence  $\Delta_\gamma$  is a negative quantity<sup>(54)</sup>. Its estimation requires a knowledge of the equilibrium surface structure which is not known for spinels. To a first approximation,  $\Delta_\gamma$  is neglected in the present calculation, and thus the results here pertain to an ideal undistorted surface.

Assuming additive central forces, the interaction potential between  $i$ th and  $j$ th atoms is given by<sup>(55)</sup>

$$V(R_{ij}) = Z_i Z_j \frac{e^2}{R_{ij}} + b_{ij} e^{-\left(\frac{R}{r_0}\right)_{ij}} - \left( \frac{c_{ij}}{R_{ij}^6} + \frac{d_{ij}}{R_{ij}^8} \right) \quad (15)$$

In Equation (15), first term on the right is the Coulomb electrostatic contribution, second term is Born-Mayer repulsive contribution and the third term in the bracket is the Van der Waals interaction contribution in a hard-shell repulsion model. No estimation of the constants  $c_{ij}$  and  $d_{ij}$  appearing in the third term in Equation (15) can be made at this time for spinels and hence only the first two terms are considered below. In all these approximations, the present work compares with that of Born and Stern<sup>(56)</sup> for NaCl where both relaxation and Van der Waals interaction were neglected.

(ii) Contribution from Coulomb Interaction: In order to calculate the surface energy as defined earlier, one needs to calculate the interaction energy between two parallel planes P and P' in Figure 24. Following the method of Friedel, Blandin and Saada<sup>(57)</sup> (so that the energy is expressed as a sum in the real space), let ions of charges  $q$  and  $q'$  be placed in a two dimensional periodic array and with identical periodicities on planes P and P' respectively in Figure 24. With  $\Omega$  as the origin, and  $O$  and  $O'$  as the position of an ion on P and its projection on P' respectively such that  $OO' = \vec{Z}$  and  $O'\Omega = \vec{r}$ ; the position of an ion on P' with respect to the ion at  $O$  is given by  $\vec{R} = \vec{Z} + \vec{r} + \vec{\rho}$ , where  $\vec{\rho}$  is the two dimensional vector joining any ion to  $\Omega$  on P'. If the interaction energy between the ions is denoted by  $W(R_i)$ , then the energy of the charge at  $O$  due to the charges

on  $P'$  is given by

$$\chi(z) = \sum_i W(|\vec{R}_i|) = \sum_i W(|\vec{z} + \vec{r} + \vec{\rho}_i|) \quad (16)$$

$$= \sum_i \int e^{i\vec{k}z} e^{i\vec{\kappa}_1 \cdot (\vec{\rho}_i + \vec{r})} \omega(\sqrt{\kappa^2 + \kappa_1^2}) d\kappa d^2\kappa_1 \quad (17)$$

$\omega(K)$  is the Fourier transform of  $W(R)$  and  $K^2 = \kappa_1^2 + \kappa^2$ ;  $\kappa$  being the component of  $\vec{K}$  parallel to  $\vec{z}$  and  $\vec{\kappa}_1$ , parallel to the plane  $P'$ . In terms of the two dimensional reciprocal lattice vector  $\vec{g}$ , and unit cell area  $S$

$$\sum_i e^{i\vec{\kappa}_1 \cdot \vec{\rho}_i} = \frac{(2\pi)^2}{S} \sum_{\vec{g}} \delta(\vec{\kappa}_1 - \vec{g}) \quad (18)$$

Thus

$$\chi(z) = \frac{4\pi^2}{S} \sum_{\vec{g}} \int e^{i\vec{k}z} \omega(\sqrt{\kappa^2 + g^2}) e^{i\vec{g} \cdot \vec{r}} d\kappa \quad (19)$$

For the Coulomb interaction  $\omega(K) = \frac{qq'}{2\pi^2 K^2}$ , the interaction energy per unit area between the planes  $P$  and  $P'$  is given by

$$\phi(z) = \frac{\chi(z)}{S} = \frac{2\pi qq'}{S^2} \sum_{\vec{g}(|\vec{g}| \neq 0)} e^{i\vec{g} \cdot \vec{r}} \frac{e^{-gz}}{g} = \frac{4\pi qq'}{S^2} \sum_{|\vec{g}| > 0} \frac{e^{-gz}}{g} \cos(\vec{g} \cdot \vec{r})$$



Including more atomic planes on either side of P and P' in calculating  $\phi(z)$ , the interaction energy between the two halves of the crystal can be calculated. Calculation of the interaction energy between planes on only one side of P or P' is unnecessary since these planes retain the bulk environment even after the surface has been created between P and P'.

(iii) Contribution from Born-Mayer Interaction: Since the Born-Mayer interaction is very short range in nature, a significant contribution comes from the nearest neighbor repulsion only. Equation (19) with appropriate  $\omega(k)$  can be used to calculate this contribution. However, it turns out that, in a complex structure where more than one b and  $r_0$  are involved, it is simpler to first calculate the energy for different individual pairs of ions. The net contribution per unit area can then be calculated by adding the contribution from all nearest neighbors that have ions on the opposite sides of the surface.

(b) Calculation for  $MgAl_2O_4$

(i) Coulomb Contribution: The atomic arrangements on different crystallographic planes have already been discussed in II.B. Let us first assume that the surface is parallel to {111} planes. In order to calculate the contribution of the Coulomb interaction to the surface energy we sum Equation 20 over z as well as  $\vec{r}$ .

$$\phi_c = \frac{4\pi qq'}{S^2} \sum_z \sum_{\vec{r}} \sum_{|\vec{g}|>0} \frac{e^{-gZ}}{g} \cos(\vec{g} \cdot \vec{r}) \quad (21)$$

$\vec{g}$  is given by Equation (3) and  $\vec{r}$ 's can be determined from Figure 6. Carrying out the calculation of  $\phi_c$  from Equation (21) until a convergent value is obtained, one gets the contribution of the Coulomb interaction to the cohesive energy between the two parts of the crystal as  $-7043 \text{ ergs/cm}^2$  across the  $\{111\}$  plane in the mixed layer<sup>(18)</sup>. A copy of the computer program to compute  $\phi_c$  is included in Appendix I. The values of  $\phi_c$  for  $\{110\}$  and  $\{100\}$  surfaces calculated in a similar way are  $-16530$  and  $-13100 \text{ ergs/cm}^2$  respectively.

(ii) Born-Mayer Contribution: There are two different cation-anion first nearest neighbor distances in a spinel, viz.,  $d_t$  and  $d_o$  corresponding to the tetrahedrally surrounded Mg ions and octahedrally surrounded Al ions respectively. Also there are three different types of oxygen-oxygen nearest neighbor distances  $d_1, d_2$  and  $d_3$ . Following the method of Striefler and Barsch<sup>(52)</sup>, both of the cation-anion interactions and only one of the anion-anion repulsions corresponding to  $d_1$  (the distance between oxygen ions located on nonparallel tetrahedron edges) are taken into account. For  $\text{MgAl}_2\text{O}_4$ ,  $a_o = 8.08 \text{ \AA}$ ,  $\delta = 0.012$

$$\text{so } d_t = a_o \left( \frac{1}{8} + \delta \right) 3 = 1.918 \text{ \AA}$$

$$d_o = a_o \left( \frac{1}{4} - \delta \right) + \delta^2 \left( \frac{1}{4} - \delta \right) + \dots = 1.928 \text{ \AA}$$

$$d_1 = a_o \left( \frac{1}{4} - 2\delta \right) 2 = 2.583 \text{ \AA}$$

Values of  $r_o$  and  $b$  can be calculated from Striefler and Barsch's<sup>(52)</sup> analysis and are given in Table IV along with the values of Born-Mayer energies for the pairs.

Depending on the nature of the planes adjacent to the surface, different numbers of cation-anion and anion-anion nearest neighbors will be broken when the surface is created. The least number of such bonds are broken if the surface is created such that the two adjacent layers of cations on the mixed layer would belong to different surfaces. This involves breaking of two tetrahedral cation-oxygen pairs and three octahedral cation-oxygen pairs per every unit area of  $(\sqrt{3}/4)a_0^2$ , contributing  $6232 \text{ ergs/cm}^2$ . The Born-Mayer contribution for the surfaces located between an anion and kagomé layer<sup>(18)</sup> or anion and mixed layer<sup>(18)</sup> are  $15010$  and  $8172 \text{ ergs/cm}^2$  respectively. Similar calculations for  $\{110\}$  and  $\{100\}$  surfaces give values of  $7100 \text{ ergs/cm}^2$  in each case.

The values of  $\gamma$  for the  $\{110\}$  and  $\{100\}$  surfaces are thus  $4715$  and  $3000 \text{ ergs/cm}^2$  respectively. The value of  $\gamma$  when the surface is parallel to  $\{111\}$  planes is  $615.5 \text{ ergs/cm}^2$  if the surface lies in a mixed layer.

### (c) Phenomonological Calculation<sup>(51)</sup>

An estimation of the surface energy can also be made by calculating the amount of work necessary to separate two internal surfaces. Let the attractive stress between the surfaces be approximated by a sine function. The stress is zero when the surfaces have their normal spacing  $d$ . As the interplanar spacing increases due to the applied stress perpendicular to these planes, the stress rises to a maximum value  $\sigma_0$  and then drops to zero when the separation of the planes exceeds the range  $h$  of the attractive forces. If  $y$  denotes the increase in the

spacing, the strain between the planes is  $y/d$  and for small strains by Hooke's law,  $\sigma = E \frac{y}{d}$ .  $E$  is the elastic modulus normal to the plane under consideration. From the above considerations,

$$\sigma = \sigma_0 \sin \frac{\pi y}{h} \quad ; h > y > 0$$

and for small  $y$ ,  $\sigma \sim \sigma_0 \frac{\pi y}{h} = \frac{E y}{d}$

$$\therefore \sigma_0 = \frac{E h}{\pi d}$$

or,

$$\sigma = \frac{E h}{d} \sin \frac{\pi y}{h} \quad (22)$$

The work done in moving the surfaces from  $y = 0$  to  $y = h$ , where they are no longer attracted, is

$$\begin{aligned} W &= \int_0^h \sigma \, dy = \frac{E h}{\pi d} \int_0^h \sin \frac{\pi y}{h} \, dy \\ &= \frac{2 E h^2}{\pi^2 d} \quad \text{per unit area} \end{aligned}$$

This energy appears as the surface energies of the two newly created surfaces. Hence the specific surface energy may be written as

$$\gamma = \frac{E h^2}{\pi^2 d} \quad (23)$$

The value of E can be calculated from the elastic stiffness coefficients<sup>(58)</sup>. The elastic constant normal to the {111} planes is

$$E_{111} = \frac{1}{3}(C_{11} + 2C_{12} + 4C_{44})$$

For  $\text{MgAl}_2\text{O}_4$ <sup>(59)</sup>,  $C_{11} = 2.825 \times 10^{12}$  dynes/cm<sup>2</sup>,  $C_{12} = 1.549 \times 10^{12}$  d/cm<sup>2</sup> and  $C_{44} = 1.547 \times 10^{12}$  dynes/cm<sup>2</sup> giving  $E_{111} = 4.037 \times 10^{12}$  dynes/cm<sup>2</sup>.

If we choose the periodicity d as the separation between two successive stoichiometric blocks ( $d_{111} = a_0/\sqrt{3}$ ) and h as the smallest possible inter layer spacing, ( $h_{111} = a_0\sqrt{3}/24$ ), we get from Equation (23),  $\gamma = 298$  ergs/cm<sup>2</sup>. Similar calculations for {110} and {100} surfaces give  $\gamma = 2702$  ergs/cm<sup>2</sup> and 1446 ergs/cm<sup>2</sup> respectively. These values clearly show the anisotropic nature of the surface energy. The {111} surfaces have the lowest values, which is consistent with the atomistic calculations.

The values of  $\gamma$  calculated from Equation (23) for  $\text{LiFe}_5\text{O}_8$ ,  $\text{NiFe}_2\text{O}_4$  and  $\text{Fe}_3\text{O}_4$  from their elastic constants<sup>(60)</sup> for various surfaces are given in Table V.

## 5. Discussion

In spite of the approximations in the calculation of  $\gamma$  by both methods, the results are important in three ways. First of all, the values compare satisfactorily even though the methods are very different. Secondly, these calculations show clearly the anisotropy of the surface energy for the spinel structure materials, with  $\gamma_{111}$  being the lowest. These calculations are consistent with the experimental results viz.

the octahedral shape of the spinel single crystals as in Figure 25. Thirdly, and the most important is that these considerations are true for all spinel systems and are independent of the chemical composition of a specific spinel. Although no experimental values are available for comparison, the calculated values may not be far-off from the experimental values in vacuum at low temperatures. That these results are qualitatively correct, is verified by etching crystals of  $MgAl_2O_4$  and  $LiFe_5O_8$  spinels where  $\{111\}$  planes are etched preferentially as shown in Figure 26. The methods of calculation have all the features one would encounter in dealing with complex ionic compounds and hence can be applied to a large number of important inorganic and ceramic materials as well as minerals. An important corollary of the calculations is that a freshly cleaved surface should have two cation layers of the "mixed layer" on the two surfaces. This awaits experimental verification and would have many useful applications in determining surface properties of many complex ionic solids.

In a decompositions reaction



where A and B can both be compounds, product B would escape from the surface leaving behind A. As the reaction front in Figure 27 moves away from the initially planar surface, pores, separated by regions richer in A would be left behind. Counter diffusion of A and B would enable B to escape out of the specimen. If this process is independent

of the crystallographic orientation of the surface, the reaction front in Figure 27 will remain planar. This also will occur if the initial surface is parallel to the preferred crystallographic plane, even when the process is anisotropic. But if the process is anisotropic and the initial surface is not a preferred surface, the reaction front would be highly irregular.

These considerations lead one to infer that the decomposition and mass loss reactions such as in (11) and (12) in III.A. occur anisotropically.  $\{111\}$  surfaces are the preferred ones, giving rise to the spongelike topography of Figure 21 with nearly flat pores and the growth-step topography of Figure 22. Assuming that the mass loss occurs by a "surface energy" mechanism<sup>(61)</sup> through the ledge-kink process, surfaces with higher specific energies are expected to be etched away to expose the low energy surfaces. On the other hand, if an "evaporation" mechanism<sup>(62)</sup> is operative in forming the facets, the faceted surfaces should consist of several exposed low-index planes. In the later case, both Figures 21 and 22 should contain facets corresponding to  $\{100\}$ ,  $\{110\}$ ,  $\{111\}$ , etc. Clearly, the observation of nearly flat pores on the starting  $\{111\}$  surface (and none of the other variants such as  $\{11\bar{1}\}$ , etc. with the same  $\gamma$  but whose formation would lead to a deviation from a planar front and thus an increase in total area) and the exposed  $\{111\}$  planes on  $\{110\}$  surfaces, coupled with the results of the surface energy calculations, suggests that the material loss is governed by a "surface energy mechanism"<sup>(61)</sup>. These considerations would apply for all spinel structure compounds in any experiment on

high temperature phase transformation where mass loss may occur. Control of the mass loss (when it gives rise to undesirable features) is another problem; but the solution of the problem requires an understanding of the processes. It is with this in mind, such an elaborate study of surface energy was undertaken. In Section V, the deleterious consequences of the mass loss on magnetic properties of  $\text{LiFe}_{5/8}\text{O}_8$  are presented.



#### IV. LATTICE DEFECTS

##### A. Introduction

Structural defects are another important feature of the microstructure. This section deals with the characterization of defects found in, and produced during the deformation of lithium ferrite spinel using high voltage electron microscopy. The possible slip planes and slip vectors in the spinel structure have been discussed by Hornstra<sup>(18,63)</sup>. With the requirement of the electroneutrality through a synchroshear mechanism, Hornstra predicted that slip should occur on  $\{111\}$  planes in spinels, with  $\frac{a}{2}\langle 110\rangle$  as the slip vector. Experimentally, this prediction has been confirmed<sup>(64)</sup>, and, in addition, other slip systems have been reported<sup>(65)</sup>. Also, growth type stacking faults have been observed on  $\{100\}$  and  $\{110\}$  planes<sup>(66-69)</sup> and twins, on  $\{111\}$  planes; but an understanding of these observations has not emerged yet. An explanation of the occurrence of the defects as observed in the present work and in those reported previously<sup>(66-70)</sup> is presented, through atomistic calculation of fault energies.

##### B. Experimental

The single crystal of  $\text{LiFe}_5\text{O}_8$  used in this study were obtained from Airtron-Litton Industries. Fifteen mil. thick discs with face normal along  $\langle 110\rangle$  were cut from the bulk single crystals using a diamond saw. These discs were deformed by a 3 point bending method at  $1200^\circ\text{C}$  in a vertical furnace. Thin specimens for examination in the electron microscope were prepared from the deformed and the undeformed crystals by cutting 3mm discs followed by subsequent

mechanical polishing and ion-thinning. Thin foils were examined in a Hitachi Hu-650 high voltage electron microscope operating at 650 kV. The optimum conditions for high voltage microscopy analysis of defects was utilized as discussed elsewhere<sup>71</sup>.

### C. Results and Interpretation

Figure 28 shows a stacking fault imaged in five different diffraction conditions. The faults can be characterized as follows: When the phase angle of the fault  $\alpha = 2\pi \vec{g} \cdot \vec{R}$  is zero for an integral multiple of  $2\pi$ , the fault is invisible. Let the fault vector  $\vec{R} = [hkl]$ ; then, from Figures 28(c), (e) and (f);

$$h-3k+l = n_1$$

$$-h+k+l = n_2$$

$$4l = n_3$$

where  $n_1, n_2, n_3$  are zero or integers. Solving the three simultaneous equations;

$$h = \frac{1}{2}(n_3 - n_1 - 3n_2)$$

$$k = \frac{1}{4}(n_3 - 2n_1 - 2n_2)$$

$$l = \frac{n_3}{4}$$

With the choice of  $n_1 = 1, n_2 = 0, n_3 = 1$ , we find the smallest possible value of  $\vec{R} = \pm \frac{1}{4}[0\bar{1}1]$ . This is not a lattice vector but is the displacement vector of the fault lying on  $(0\bar{1}\bar{1})$  as determined from trace analysis.  $\alpha = 2\pi \vec{g} \cdot \vec{R} = \pm\pi$  and the fringes show typical  $\pi$  contrast (Figure 28). The fault is bounded at its edges by sessile partial dislocations of Burgers vector  $\frac{1}{4}[0\bar{1}\bar{1}]$ , and corresponds to a stacking fault in the cation sublattice of the spinel as discussed by Van der Biest and

Thomas<sup>(70)</sup>. From image contrast analysis, however, it is not possible to distinguish between extrinsic and intrinsic  $\pi$ -faults in this material (i.e. whether material has locally been "removed" or "inserted" from the structure) and techniques such as direct lattice imaging may be necessary to establish this aspect of the fault. By comparing Figures 28(c) and (f) it can be seen that the dislocation image widths are decreased by imaging in high order bright-field conditions (f) (see Ref. 71).

Figure 29 is a high order bright-field image of dislocations in the deformed material. The dislocation density is not very high; however, straight dislocations lying parallel to the intersection of the foil plane (110) and other {110} planes can be seen. This indicates that slip (or recovery) has occurred on {110} planes. Healed cracks such as those in Figure 30 are also seen occasionally in the deformed microstructure indicating that the material is not completely ductile at 1200°C.

Figure 31 shows a weak beam image of a dislocation network in deformed lithium ferrite. The dislocations lie parallel to the intersections of other {110} planes with the foil plane and are dissociated into partials. The dissociation can be resolved to be

$$\frac{1}{2} \langle 110 \rangle = \frac{1}{4} \langle 110 \rangle + \frac{1}{4} \langle 110 \rangle$$

on {110} slip planes. The image profile computed for the operating multibeam reflection conditions is shown in Figure 31(c), which compares very well with the microdensitometer trace given in Figure 31(b). The partials in the foil are separated by about 220Å. Using non-isotropic

elasticity<sup>(41)</sup>, it is calculated from this spacing that the surface energy between the partials i.e., the stacking fault energy is 75 ergs/cm<sup>2</sup>. For an ionic solid such as LiFe<sub>5</sub>O<sub>8</sub> spinel, this value seems to be low. Since it cannot be ascertained whether or not the partials are in equilibrium positions, as climb may occur during the high temperature deformation, this value of stacking fault energy, or surface energy, must only be approximate.

#### D. Atomistic Calculation of Fault Energy

In principle, when computing the crystal energy, one has to account for<sup>(72)</sup> (i) electrostatic interaction energy, (ii) residual covalent bond energy, (iii) polarization energy, (iv) Born-Meyer repulsion energy and (v) zeropoint vibrational energy. Defining the stacking fault energy as the difference in the energy of interaction between the faulted and the perfect crystal, one needs to take into account only those contributions that would be significantly different in a faulted crystal compared to that in the perfect crystal. The covalency effect is next to the Coulomb energy in importance<sup>(73)</sup> in spinel and is even more important than the polarization energy<sup>(73)</sup>. To a first approximation, when the nature of the fault is such that the stoichiometry of the crystal and the nearest neighbor distributions are not disturbed<sup>(70)</sup>, (as in Figure 5(a) showing the atomic configuration in the presence of a  $(1\bar{1}0)\frac{1}{4}[110]$  fault), the last two effects can be neglected. The residual covalency can be computed approximately from the electrostatic interaction by assigning bond charges  $-|e|/\epsilon(0)$  to the centers of the nearest neighbor bonds<sup>(74)</sup>. The polarization,

effect can be included in an approximate way through the electronic polarizability of the faulted material. Thus, the problem of the computation is reduced to a calculation similar to the ones performed in Section III.B.4.

To evaluate  $\phi_c$  for a perfect crystal, one has to sum Equation 20 over  $q$ ,  $q'$ ,  $\vec{r}$  and  $z$  as before. (This is incorporated in the program in Appendix A). The periodicities defined in Figures 4, 5 and 6 remain unchanged, but the interlayer spacings change to account for the localised bond larges.  $\phi_c$  for the faulted crystal can be calculated similarly by changing  $\vec{r}$  to  $\vec{r} + \vec{R}$  if the fault vector  $\vec{R}$  lies on the fault plane. If  $\vec{R}$  does not lie on the fault plane, the calculations can be carried out by first determining the charge distributions in the faulted crystal. The difference in energies per unit area of the fault plane then gives the stacking fault energy. The results of the calculations for some shear and growth faults in  $MgAl_2O_4$ ,  $NiFe_2O_4$ ,  $LiFe_5O_8$  and  $Fe_3O_4$  are tabulated in Table VI. Twinning energies for  $MgAl_2O_4$  and  $Fe_3O_4$  are also included in the table.

#### E. Discussion

The computed values of fault energies in Table VI show that twins on  $\{111\}$  planes have energies much lower than those of the growth type cation faults on  $\{111\}$  planes. Also, the cation stacking faults should occur with higher probability on planes such as  $\{110\}$  and  $\{100\}$  than  $\{111\}$ , consistent with the observations<sup>(66-70)</sup>. As pointed out by Veyssiere et. al<sup>(75)</sup>. Such computations are significant only for comparison purposes and thus are semiquantitative. The correspondence

between the calculated and measured values of  $\gamma$  here may only be fortuitous.

The original prediction of Hornstra<sup>(18,63)</sup> about the fourfold dissociation of a dislocation on  $\{111\}$  planes has not been confirmed experimentally although images with four intensity peaks have been recorded under different diffracting conditions<sup>(76)</sup>. One such example is shown in Figure 32(a). Figure 32(a) is the weak beam image of a dissociated dislocation and the corresponding high order bright field image is shown in Figure 32(b). As can be seen, the high order bright field image does not show the extra intensity peaks present in the high resolution dark field image of Figure 32(a). It has been confirmed through computation of the image profiles that the extra intensity peaks in Figure 32(a) are purely due to dynamical scattering effects and not to structural characteristics. Also, slip systems other than the ones predicted by Hornstra have been reported as in the present paper, and rather more frequently in nonstoichiometric spinels<sup>(65)</sup>. Calculation of the Peierls' stress on different crystallographic planes remains to be done and the understanding of the slip system in spinels is far from clear. However, the present results show that dislocation motion in  $\text{LiFe}_5\text{O}_8$  occurs on  $\{110\}$  planes alone, in spite of the fact that the Schmidt factor for  $\{110\} \times \langle \bar{1}\bar{1}0 \rangle$  is less than that for  $\{111\} \times \langle \bar{1}\bar{1}0 \rangle$  under the loading conditions.

## V. ELECTRICAL RESISTIVITY AND MAGNETIC HYSTERESIS

### A. Introduction

The combination of the ferrimagnetic properties of ferrites with high electrical resistivity gives these materials great practical usefulness. In this section, the changes in the electrical resistivity as well as magnetic hysteresis with changes in microstructure are studied. Some of the microstructures are produced through the phase transformation in  $\text{LiFe}_5\text{O}_8$  discussed in Section III.A. The effect of cation faults have been studied in as-received  $\text{LiFe}_5\text{O}_8$  as well as polycrystalline  $\text{NiFe}_2\text{O}_4$ .

### B. Experiment

Dispersion of a second phase in  $\text{LiFe}_5\text{O}_8$  was achieved in thin discs via the high temperature phase transformation discussed in Section III, and the microstructures were examined for reproducibility. Defects in single crystal lithium ferrite and polycrystalline  $\text{NiFe}_2\text{O}_4$  were studied by preparing thin foils from the as-received as well as the annealed materials. The electron microscopy observations were made in HU-650 high voltage electron microscope operating at 650 kV. The dynamic hysteresis loops were taken at 60Hz using torroidal specimens. The size of the specimens used is 1.0 cm outer diameter, 0.6 cm inner diameter and 0.2 cm thick. Twenty turns of copper magnetic wire were used in both primary and secondary windings. The electrical resistivity was measured by a three point probe method discussed elsewhere<sup>(77)</sup> in detail.

### C. Results and Interpretation

#### 1. Phase Transformation and Magnetic Properties

The morphology and kinetics of the precipitation reaction has already been discussed in detail in Part III. The hysteresis loops and the corresponding representative microstructures are shown in Figure 33. The hysteresis curve d in Figure 33(D) is from the as received single phase  $\text{LiFe}_5\text{O}_8$ . The coercivity of the two phase microstructures in (a) or (b) of Figure 33(D) is higher than that of single phase  $\text{LiFe}_5\text{O}_8$ . Also the coercivity of polygranular single phase spinel as in Figure 33(C) is higher than that of single phase crystals.  $\text{LiFeO}_2$  phase is paramagnetic<sup>(78)</sup> and thus it is not surprising that its dispersion in a ferrimagnetic phase increases  $H_c$  by acting as a barrier to the domain wall motion<sup>(79)</sup>. A new and significant observation in Figure 33 is that the squareness of the hysteresis loop, defined as  $(Br/4\pi M_s)$  is higher for the two phase microstructures of  $\text{LiFeO}_2$ - $\text{LiFe}_5\text{O}_8$ . Reduction of the value of  $M_s$  in (c) of Figure 32(D) is due to reduction of  $\text{Fe}^{+3}$  to  $\text{Fe}^{+2}$ .

#### 2. Defects and Magnetic hysteresis

Figure 34(A) shows the cation stacking faults in a specimen prepared from the vicinity of the surface of flux-grown  $\text{LiFe}_5\text{O}_8$  single crystal. The faults are on  $\{110\}$  planes with  $\frac{1}{2}\langle 110 \rangle$  as the displacement vector<sup>(70)</sup>. The defect density decreases rapidly with increasing distance from the surface. The hysteresis loops of faulted and unfaulted materials are shown in Figure 34(B). Presence of faults increases the coercivity. In the absence of any data on the magnetic



domain configurations, a discussion on the interaction of the cation faults with the domains is not possible at this stage. It may be noticed that the  $M_s$  value of faulted and unfaulted materials are the same. Figure 35(A) shows a faulted grain in a polycrystalline  $\text{NiFe}_2\text{O}_4$ . More than 30% of the grains are seen to be faulted in the as-received crystals. On annealing the material in air for 12 hours at  $850^\circ\text{C}$ , the fault density decreases considerably, leaving about 95% of the grains fault-free with no other microstructural modifications. There is a change in the hysteresis curve as in Figure 35(B).

### 3. Electrical Resistivity and Microstructure

The changes in electrical resistivity as a function of microstructure are illustrated in Figure 36. The deterioration of  $\rho$  with mass loss is apparent from the Figure. Also, the changes in  $\rho$  with the formation of precipitates is noticeable and consistent with the results of other precipitation hardened systems<sup>(80)</sup> at least qualitatively. The values of  $\rho$  when stacking faults in  $\text{NiFe}_2\text{O}_4$  are present and absent are  $3 \times 10^5 \Omega\text{cm}$  and  $3.1 \times 10^5 \Omega\text{cm}$  respectively and thus are not very different. But  $\rho$  changes from  $2 \times 10^2 \Omega\text{cm}$  to  $3 \times 10^3 \Omega\text{cm}$  in  $\text{LiFe}_5\text{O}_8$  between the near-surface region and the bulk. This may be ascribed to an abundance of  $\text{Fe}^{+2}$  ions near the surface during the crystal growth.

### D. DISCUSSION

Applications of ferrites in computer memory cores and in microwave device components such as latching devices<sup>(81)</sup> require good squareness of the B-H loop. A necessary condition for good squareness is the dominance of the anisotropy energy over the magnetostrictive

energy and this dictates the choice of materials. Proper processing is also used to enhance this effect<sup>(82)</sup>. The present results suggest yet another way of achieving it. In the absence of data on other magnetic properties of the two-phase systems, evaluation of the usefulness of these materials compared to the currently used ones is not possible, but it seems to be a step in the right direction in materials technology.

The result that  $H_c$  increases in a two-phase microstructure is not new<sup>(83)</sup> but the approach is new for ceramic magnets. It may be possible to use a similar approach to achieve better properties in hard magnetic ferrites than presently exist.

The polycrystalline nickel ferrites in the as-fabricated state are highly defective and this may be the reason for the poor performance of this material. (The samples examined here were from a rejected batch of commercial  $NiFe_2O_4$  manufactured by Countis Industries, San Luis Obispo, California). All the magnetic properties of the annealed material have not been studied here, but the data presented here suggests that a proper post-processing thermomechanical treatment may provide ways of improving the properties; thus reducing waste of material.

The accompanying changes in  $\rho$  imply that the low mobility characteristics of the material do not degrade with the microstructure. The effect of cation faults on the electrical resistivity is insignificant compared to their effect on the hysteresis loss. Besides, an improvement in the squareness is accompanied by an improvement in the resistivity too. Changes in the resistivity with frequency have not been examined to evaluate the eddy loss characteristics of these microstructures.

In conclusion, this preliminary study of the effect of micro-structure on magnetic hysteresis shows that proper thermomechanical treatment of ceramic ferrites may be the step beyond the presently existing processes<sup>(2)</sup> which will bring about cheaper, better and more useful ceramic ferrites.

## VI. REMARKS

For ceramic specimens, ordinary metallography is far from simple and methods to study microstructure are distinctly limited. The impossibility of electropolishing non-conducting oxides has impeded progress towards obtaining all the detailed microstructural information on ferrites which has already been obtained for metallic magnets by transmission electron microscopy (considering, for example, the extremely extensive studies of precipitate structures in permanent magnet alloys<sup>(84)</sup>). Furthermore, the limited research in microstructures have not thus far been systematically related to magnetic properties<sup>(85)</sup>. The present research has been the first attempt towards a basic understanding of the microstructure property relationships of some ceramic soft ferrites. The features of the microstructure, the way they evolve, and their effect on the physical properties were some of the topics studied.

From the preceding sections it is clear that the problems associated with these studies are as complex as the systems themselves. Use of novel experimental techniques provides new structural information as illustrated in Section II. The discovery that the octahedral ions are off-center, and that the space group transforms at high temperature is so new that the full implications can scarcely be imagined at the present time<sup>(86)</sup>. The mechanism of superexchange in spinel ferrite<sup>(87)</sup> would suggest that, at the very least, there must be important implications for the magnetostrictive properties<sup>(88)</sup> and indeed an anomalous behaviour of this kind has already been reported<sup>(89)</sup>. In some cases

entirely new properties may become possible, such as anti-ferroelectricity<sup>(11)</sup> and photomagnetic effects<sup>(90)</sup>. Clearly, an immense amount of work remains to be done, and, although there are formidable theoretical difficulties, a fascinating time must lie ahead for all of us involved.

The phase relations in multicomponent systems are in general complex. In addition, results of microscopic examination of phases in many ceramic systems are often difficult to explain<sup>(46)</sup> using the existing phase diagrams since most of these diagrams were determined from bulk samples. This is true for  $\text{LiFe}_5\text{O}_8$ , which, according to the phase diagram of Strickler and Roy<sup>(30)</sup> should melt congruently upon heating. The material loss at elevated temperatures complicates the studies further and a multi-faceted approach is needed for success.

Imperfections always exist in any real material<sup>(41)</sup>. An understanding of their origin may lead to determining ways of controlling the defects when undesirable and vice versa. High voltage electron microscopy is a unique tool to study some of the defects in complex ceramics<sup>(91)</sup>. Only line and planar defects were investigated in some detail here. Grain boundaries need considerable attention, since many commercial materials are polygranular. Also the subject of point defects must be emphasized. A study of defect chemistry accompanying the material loss would provide useful guidelines for the processing and thermomechanical treatments. Finally, the complications that may arise due to the presence of impurities are illustrated in Section III (Figure 16).

The most important problem is, probably, the isolation of a single microstructural feature so as to study its effect on the electromagnetic properties in these complex oxide ceramics. Interestingly enough, investigations of this kind are the most useful ones for a materials designer. They will not only enable one to prepare better materials, but also provide scientific knowledge necessary to design advanced electronic and magnetic materials that may be needed for sophisticated communication and storage devices in future.

The unique combination of electronic and magnetic properties in soft ferrites makes them central to their usage. An improvement in the magnetic characteristics at the expense of electrical conductivity is as useless as its converse. It is important to note that the results in Section V on two phase microstructures combine the best of both of these properties. Improvement of the magnetic characteristics for  $\text{NiFe}_2\text{O}_4$  is not accompanied by any deterioration of the resistivity either.

Thus, based on these limited observations, it may be remarked here that a whole new era in the area of ceramic ferrite materials might be emerging soon. The much neglected research on this group of materials has finally begun. With dedication at present and firm commitment for the future, this new approach should, before long, enable us to design and prepare materials and devices for the ever-advancing electronics technology.

#### ACKNOWLEDGEMENT

The continued guidance, help and encouragement of Professor Gareth Thomas is gratefully acknowledged. It is also a pleasure to thank Professor A. W. Searcy and Dr. O. Van der Biest for many fruitful discussions. Finally, the technical help of the laboratory support staff, many useful conversations with my co-researchers and friends (to mention only a very few, B. Gantayat, F. Dizon, R. Gronsky, U Dahmen, R. Drosd and M. Rahmani) and the enthusiasm of my family members is sincerely acknowledged.

This research was sponsored by the United States Energy Research and Development Administration through the Materials and Molecular Research Division of the Lawrence Berkeley Laboratory.

REFERENCES

1. G. Thomas, "Utilization and Limitations of Phase Transformations and Microstructures in Alloy Design for Strength and Toughness", in Proc. of Battelle Colloquium on Fundamental Aspects of Structural Alloy Design, Ed. by R. I. Jaffee, Seattle, Washington, 1975, In Press. Lawrence Berkeley Laboratory Report #4175.
2. M. Sugimoto, "Recent Advancement in the Field of High Frequency Ferrites" in AIP Conference Proc. 10 (2), Ed. by C. D. Graham Jr. and J. J. Rhyne, American Institute of Physics, New York, 1973, 1335.
3. G. K. Bansal and A. H. Heuer, Acta Met., 20, 1281 (1972).
4. M. H. Lewis, J. Billingham and P. S. Bell, Proc. Fifth International Materials Symp., "Electron Microscopy and Structure of Materials", Ed. G. Thomas, R. M. Fulrath, R. M. Fisher, Univ. of Calif. Press, 1972, 1084.
5. O. Van der Biest, D. R. Clarke and G. Thomas, Proc. Sixth International Materials Symposium, "Ceramic Microstructures", Ed. R. M. Fulrath and J. A. Pask. In Press.
6. A. H. Heuer and T. E. Mitchell, J. Phys. C, 8, L541, (1975).
7. A. Broese van Groenou et. al. Mater. Sci. Eng. 3, 317 (1968/69).
8. W. H. Bragg, Nature, Lond. 95, 561 (1915), Phil. Mag. 30, 305 (1915).
9. S. Nishikawa, Proc. Tokyo Math.-phys. Soc. 8, 199 (1915).
10. N. W. Grimes, Phil. Mag. 26, 1217 (1973).
11. N. W. Grimes, J. Phys. C, 6, L78 (1973).
12. L. Hwang, A. H. Heuer and T. E. Mitchell, Phil. Mag. 28, 241 (1973).



13. J. J. Higgins, J. A. Speer and J. R. Craig, *Phil. Mag.* 30, 683 (1975).
14. E. Samuelson, *J. Phys. C*, 7, L115 (1974).
15. D. P. Williamson and H. W. Grimes, *J. Phys. D*, 7, 1 (1974).
16. L. D. Landau and E. M. Lifshitz, *Statistical Physics*, Pergamon Press, (1959).
17. C. Haas, *J. Phys. Chem. Sol.* 26, 1225 (1965).
18. J. Hornstra, *J. Phys. Chem. Solids*, 15, 311, (1960).
19. K. H. Hellwege, and A. M. Hellwege, (eds.), Magnetic and Other Properties of Oxides and Related Compounds, Landolt-Bornstein Tables, III/4b, 325-343, Springer Verlag, 1970.
20. F. F. Wang, R. L. Gravel, M. Kestigian, *IEEE Trans. Magnetics*, 4, 55 (1968).
21. R. G. West, and A. C. Blankenship, *J. Amer. Cer. Soc.*, 50, 343 (1967).
22. J. P. Remeika, and R. L. Comstock, *J. Appl. Phys.*, 35, 3320 (1964).
23. D. H. Ridgley, H. Lessoff, and J. D. Childress, *J. Amer. Cer. Soc.*, 53, 304 (1970).
24. A. J. Pointon, and R. C. Saull, *J. Amer. Cer. Soc.*, 52, 157, (1969).
25. G. Bandyopadhyay, and R. M. Fulrath, *J. Amer. Cer. Soc.*, 57, 182 (1974).
26. G. Bandyopadhyay, and R. M. Fulrath, *J. Amer. Cer. Soc.*, 57, 483 (1974).
27. M. Amemiya, *Proc. of the International Conf. on Ferrites*, Y. Hoshino, et al., eds., University of Tokyo Press, Tokyo, 154 (1971).

28. M. Amemiya, J. Inorg. Nucl. Chem., 34, 3405 (1972).
29. O. N. Salmon and L. Marcus, J. Amer. Cer. Soc., 43, 549 (1960).
30. D. W. Strickler and R. Roy, J. Amer. Cer. Soc., 44, 225 (1961).
31. Yu. D. Tretyakov et al., J. Solid State Chemistry, 5, 191 (1972).
32. P. B. Braun, Nature, 170, 1123, (1952).
33. O. Vander Biest and G. Thomas, Acta Cryst., A31, 70, (1975).
34. D. J. Barber et al., J. Mat. Sci., 8, 1030 (1973).
35. R. Sinclair, K. Schneider and G. Thomas, Acta. Met. 23, 873 (1975).
36. J. M. Cowley, Acta Cryst. A29, 537 (1973).
37. R. Sinclair and G. Thomas, J. Appl. Crystallography 8, 206 (1975).
38. R. Sinclair, R. Gronsky and G. Thomas, Acta Met. 24, 789 (1976).
39. L. M. Brown, G. R. Woolhouse and U. Valdre, Phil. Mag. 17, 781 (1968).
40. J. D. Eshelby, Prog. Solid Mech. II., 89 (1961).
41. J. P. Hirth and J. Lothe, Theory of Dislocation, McGraw Hill, (1968).
42. M. F. Ashby and L. M. Brown, Phil. Mag. 8, 1083 (1964).
43. H. Brooks in Metal Interfaces, p. 20, Amer. Soc. Metals, 1952.
44. M. Schieber, "High Temperature Phase Transitions in Lithium Ferrite Spinel Single Crystals", J. Inorg. Nucl. Chem., 26, 1363-1367 (1964).
45. E. Posnjak and T. F. W. Barth, "A New Type of Crystal Fine-Structure: Lithium Ferrite ( $\text{Li}_2\text{O} \cdot \text{Fe}_2\text{O}_3$ )", Phys. Rev., 38, (12), 2234-2239 (1931).
46. L. C. DeJonghe and G. Thomas, "High Voltage Electron Microscopy Studies of Phase Transformation in Cobalt Ferrites", Mater. Sci. Eng., 8, (5), 259-274 (1971).

47. H. Schmalzried, Solid State Reactions (English Trans. by A. D. Pelton), Academic Press, 1974.
48. W. D. Kingery, H. K. Bowen and D. R. Uhlman, Introduction to Ceramics, 2nd ed., John Wiley and Sons, Inc. (1976).
49. S. K. Rhee, J. Amer. Cer. Soc. 58, 279 (1975).
50. J. J. Duga, "Surface Energy of Ceramic Materials", Defense Ceramic Information Center Rept. 69-2, 1969.
51. J. J. Gilman, J. Appl. Phys. 31, 2208 (1960).
52. M. E. Striefler and G. R. Barsch, J. Phys. Chem. Sol. 33, 2229, (1972).
53. M. P. Tosi, Solid State Phys. v. 16, Ed. F. Seitz and D. Turnbull, Academic Press, (1964).
54. G. C. Benson, P. Balk and P. White, J. Chem. Phys. 31, 109 (1959).
55. G. C. Benson and K. S. Yun, Solid Gas Interfaces, v-1, Ed. E. A. Flood. Marcel Derrer Inc. N. Y. (1967).
56. M. Born and O. Stern, Sitzber. preuss. Akad. Wiss. Physik. math. Kl. 901 (1919).
57. A. Blandin, J. Friedel and G. Saada, J. dePhys., 27,C3, 128 (1966).
58. C. Kittel, Intr. Sol. St. Phys., 4th Ed. Addison Willey, 1972.
59. Z. P. Chang and G. R. Barsch, J. Geophys. Res. 78, 2418 (1973).
60. L. N. Ryabinkin and A. M. Kapitonov, Bull. Academy of Science of the USSR, Phys. Ser. 34, 975 (1970).
61. A. J. W. Moore, Metal Surfaces, Amer. Soc. Metals, (1962).
62. G. E. Rhead and H. Mykura, Acta Met. 10, 843 (1962).
63. J. Hornstra, Proc. Fourth International Conf. on Reactivity of Solids, (1961).

64. K. C. Radford and C. W. A. Newey, Proc. British Ceramic Society 9, 131 (1967).
65. M. Doukhan and B. Escaig, J. de Phys. Letters 35, 181, (1974).
66. M. H. Lewis, Phil. Mag., 17, 481 (1968).
67. H. Tabota et al., Jap. J. Appl. Phys. 12,7(1973).
68. G. S. Baker and M. J. Whelan, Proc. Seventh International Congress of Electron Microscopy, Ed., P. Favard, 2, 283 (1970), Soc. Francais de Mic. Electronique, Paris.
69. A. G. Fitzgerald and R. Engin, Thin Solid Films, 20, 317 (1974).
70. O. Van der Biest and G. Thomas, phys. stat. sol. A24, 65 (1974)
71. L. J. Chen and G. Thomas, phys. stat sol. A25, 193 (1974).
72. C. A. Coulson, Valence, 2nd ed., Clarendon Press, (1961).
73. J. Smit, Solid State Communications, 6, 745 (1968).
74. J. Phillips, Rev. of Modern Phys. 42, 317 (1970).
75. P. Veyssiere et al., phys. stat. sol. A31, 605 (1975).
76. P. Veyssiere et al., Phil. Mag., 33, 143 (1976).
77. J. J. Dih, Electrical Conductivity in Lithium Ferrite and Lead Zirconate Titanate Ceramics, Ph.D. Thesis, Univ. of Calif. Berkeley, 1976. LBL #4930
78. J. C. Anderson et al., The Magnetic Susceptibilities of  $\text{LiFeO}_2$ , J. Phys. Chem. Sol. 26, pp 1555-1560, 1965.
79. P. Haasen, "Mechanical, Magnetic and Superconductor Hardening by Precipitates", Mat. Sci. Eng., 9, pp 191-196, 1972.
80. J. W. Christian, The Theory of Transformations in Metals and Alloys, Pergamon Press, 1965.

81. G. M. Argentina and P. D. Baba, "Microwave Lithium Ferrite - An Overview", IEEE Trans. Microwave Theory and Tech., MTT-22, pp 652-658, 1974.
82. P. D. Baba et al. "Fabrication and Properties of Microwave Lithium Ferrites", IEEE Trans. Magnetics, MAG-8, pp 83-94, 1972.
83. H. G. Brion et al. "Pinning of Bloch Walls by Non-Magnetic Particles", Int. J. Magnetism, 5, pp 109-110, 1973.
84. J. E. Gould, Cobalt Alloy Permanent Magnets, Centre D'Information du Cobalt, Brussels (1971).
85. D. J. Craik, Magnetic Oxides, Ed. D. J. Craik, John Wiley and Sons, (1975).
86. N. W. Grimes, Contemp. Phys. 17, 71 (1976).
87. P. W. Anderson, Magnetism, v.1, Ed. G. T. Rado and H. Suhl, Academic Press, (1963).
88. C. Heck, Magnetic Materials and their Applications, (English Translation - S. S. Hill), Crane, Russak and Co. (1974).
89. W. Bindloss, J. Appl. Phys. 42, 1474 (1971).
90. W. Lems et al., Phys. Rev. Lett. 21, 1643 (1968).
91. G. Thomas, Physical Aspects of Electron Microscopy and Microbeam Analysis, Ed. B. Siegel and D. R. Beaman John Wiley and Sons, 1975.

TABLE I

Semiquantitative spectrographic analyses of as grown  $\text{LiFe}_5\text{O}_8$  single crystal.

Constituent Element	Amount (wt. % as oxides)
Fe	Principal Constituent
Pb	15.0
B	4.0
Li	2.0
Pt	0.15 (as metal)
Mn	0.025
Al	0.01
Si, Mg, Ca, Ni, Cr, Mo	< 0.005

TABLE II

Annealing times for 15 mil thick discs

	Air	Vacuum ( $10^{-5}$ torr pressure)	Oxygen (760 torr pressure)
Stage I	15-30 minutes	-----	30-45 minutes
Stage II	30-60 minutes	$\leq$ 60 minutes ~	45-75 minutes
Stage III	> 60 minutes	$\geq$ 60 minutes	> 75 minutes

TABLE III

Lithium and iron contents as determined by a semiquantitative chemical analysis.

Atmosphere	Annealing times	<u>Li</u> (wt%)	<u>Fe</u> (wt%)
-----	As received	1.62	63.84
Air	Stage I	1.54	67.44
	Stage III	1.17	68.57
Vacuum	Stage II	1.51	67.73



TABLE IV

Repulsive Interaction Parameters and Born-Mayer Energy for  $\text{MgAl}_2\text{O}_4$

	$r_0$ (Å)	b (ergs)	$V = be^{-\frac{d}{r_0}}$
Mg-O	0.325	$10^{-9}$	$2.74 \times 10^{-12}$
Al-O	0.325	$1.53 \times 10^{-9}$	$4.05 \times 10^{-12}$
O-O	0.275	$5.95 \times 10^{-9}$	$5 \times 10^{-13}$

TABLE V

Values of Surface Energies Calculated from Equation 23

Material.	{111} surface <sub>2</sub> (ergs/cm <sup>2</sup> )	{110} surface <sub>2</sub> (ergs/cm <sup>2</sup> )	{100} surface <sub>2</sub> (ergs/cm <sup>2</sup> )
LiFe <sub>5</sub> O <sub>8</sub>	222	2122	1331
NiFe <sub>2</sub> O <sub>4</sub>	207	1837	1161
Fe <sub>3</sub> O <sub>4</sub>	223	2164	1451

TABLE VI

Computed values of stacking fault energies in spinel

Chemical Formulae	Spinel Type	Fault Configuration	Calculated Energy ergs/cm <sup>2</sup>
MgAl <sub>2</sub> O <sub>4</sub>	Normal Spinel	{100} $\frac{1}{2}$ <110>	292
		{110} $\frac{1}{2}$ <110>	257
		{111} $\frac{1}{2}$ <110>	4130
		{111} Twin	224
LiFe <sub>5</sub> O <sub>8</sub>	Inverse Spinel	{100} $\frac{1}{2}$ <110>	1022
		{110} $\frac{1}{2}$ <110>	194
		{111} $\frac{1}{2}$ <110>	3742
		{111} Twin	267
		$\frac{1}{2}[110] = \frac{1}{2}[110] + \frac{1}{2}[110]$ on (110)	79

## APPENDIX I

### Computer Program for the Calculation of Coulomb Contribution

The following Fortran program calculates  $\phi_c$  of Section III.B.4. Choosing appropriate iteration parameters, the accuracy of the computation can be improved. The present calculations are performed through a trial method to obtain convergent values of  $\phi_c$ . Comment cards in the program define the input parameters. The program is deliberately kept simple so that it can be modified easily to perform other types of calculations such as  $\gamma$  in Section IV.

```
Program Coulomb (Input, Output)
Dimension Phi (56), S(56), DZ(56), RX(56), RY(56), GX(56) GY(56),
1DLZ (784), RI(784), R2(784), PSI(28), SS(28), TITLE (8)
C Program for (110) Surface with Two Stoichiometric Blocs on
Both Sides
C A= Lattice Parameter. EPSLN=Dielectric Constant (=1 for these
C Calculations). EE=Electronic Charge. Phi=Ionic Charge (A Number).
C S=Area of the Two Dimensional Unit Cell.
C RX and RY are Components of R.
C GXX and GYY are Components of G.
C DZ is the Vertical Height of an Atomic Plane.
C M,N,MM,NN, are to be chosen for the Iterations
Real H, K, HM, KM, HKX, HKY
Read 18, Title
Read 11, A, PI, EPSLN, EE
Read 16, M, N, MM, MN
Do 1 I =1, MM
Read 11, PHI(I), S(I), RX(I), RY(I)
1 Read 17, DZ(I)
Read 12, GXX, GYY
Read 12, HM, KM
Print 19, TITLE
11 Format (4F8.4)
12 Format (2F8.4)
13 Format (F14.8)
16 Format (4I3)
17 Format (F8.4)
18 Format (8A10)
19 Format (1H1, 1H, 8A10////)
II=0
I=1
GM=0.
5 Continue
GY(I)=GY
GX(I)=GXX
Print 21,I, DZ(I)
21 Format (1H, 10X,*1=*13,10X,*DZ(I)=*,F8.4)
J=1
10 Continue
PSI(J)=PHI(M+J)
SS(J)=S(M+J)
II=II+1
DLZ(II)=DZ(M+J)-DZ(I)
RI(II)=RX(M+J)-RX(I)
R2(II)=RY(M+J)-RY(I)
H=0.
15 Continue
K=0.
20 Continue
```

```
HKX=ABS(H*GX(I))
HKY=ABS(K*GY(I))
G=2.*PI*(HKX**2.+HKY**2.)**.5
IF(G.EQ.0.) GO TO 25
GR=2.*PI*(H*GX(I)*R1(II)+K*GY(I)*R2(II))
P=-G*DLZ(II)
GMA=4.*PI*EE**2.*10.**4/((EPSLN)*(A**3.))*PHI(I)*PSI(J)/(S(I)
1*SS(J)) *G)*EXP(P)*COS(GR)
GM=GM+GMA
25 Continue
K=K+1.
IF((KM-K).GE.0.) GO TO 20
H=H+1.
IF((HM-H).GE.0.) GO TO 15
J=J+1
IF((N-J).GE.0) GO TO 10
PRINT 13, GM
I=I+1
IF((M-I).GE.0) GO TO 5
Print 22, HM,KM
22 Format (1H,2X,*HM,KM=*2F8.4)
Print 23,GM
23 Format (1H,5X,*Coulomb Energy =*F14.8,1X,*ERGS/Sq. CM.*)
STOP
END
```

FIGURE CAPTIONS

- Figure 1. Selected area electron diffraction pattern from  $\text{LiFe}_5\text{O}_8$ . Foil normal is along  $\langle 100 \rangle$ , so that double diffraction cannot give rise to 200 spots.
- Figure 2. Selected area electron diffraction patterns from  $\text{MgAl}_2\text{O}_4$  in  $\langle 100 \rangle$  orientation; (a) taken at room temperature showing 200, 420, type spots, (b) taken at  $\sim 450^\circ\text{C}$  from the same area where these reflections have disappeared. The slight shift in the Kikuchi pattern is due to a slight buckling of the foil upon heating.
- Figure 3. SAD from  $\text{MgAl}_2\text{O}_4$  oriented near  $\langle 100 \rangle$  to excite the (400) systematic row; (a-c) taken at the temperatures shown during a heating sequence, and (d) taken after cooling the specimen to  $440^\circ\text{C}$ . Note the disappearance of the 200 spot marked by an arrow in (a) upon heating to  $450^\circ\text{C}$  and its reappearance in (d) upon cooling.
- Figure 4. Projection of an ideal spinel structure on the (001) plane. The primitive two-dimensional cell is shown by the dotted lines and the corresponding reciprocal lattice vectors with respect to the axes are given in Equation 1.

- Figure 5 (a) Projection of a faulted spinel structure on the (110) plane. The fault is  $(1\bar{1}0)\frac{1}{4}[1\bar{1}0]$  growth type fault, produced by the removal of two successive layers of atoms along  $[1\bar{1}0]$ , corresponding to a stoichiometric block.
- (b) Same type of projection on (110) as in Figure 4. The reciprocal lattice vectors are given by Equation 2.
- Figure 6 Similar to Figure 4 but for a projection on the (111) plane. The occupancy of different atomic sites are indicated below the sketch. Alternate cation layers can be described as kagomé or mixed layers and are populated differently.
- Figure 7 Sketch to show the position of the  $\text{LiFeO}_2$  phase and the small angle boundaries inside the  $\text{LiFe}_5\text{O}_8$  crystal as the phase transformation proceeds. The three stages are distinguished by the microstructure-depth relationships as shown. Amorphous particles are not shown.
- Figure 8 Bright field image showing octahedral precipitates of  $\text{LiFeO}_2$  in  $\text{LiFe}_5\text{O}_8$  matrix. This BF micrograph, near  $[110]$ , shows the projection of the octahedra with depth oscillation fringes due to inclined  $\{111\}$  faces. The particles have negligible strain contrast around them.



- Figure 9 Lattice fringe image from an ionthinned  $\text{LiFe}_5\text{O}_8$  specimen containing octahedral  $\text{LiFeO}_2$  particles,  $000$ ,  $g_{111}^-$  and  $2g_{111}^-$  are combined to produce the image in Phillips EM-301 high resolution electron microscope. Note the sharpness of the precipitate-matrix boundary at A.
- Figure 10 Lattice fringe image of  $\text{LiFe}_5\text{O}_8 \cdot \text{LiFeO}_2$  interface when  $\text{LiFeO}_2$  precipitates are semicoherent. Diffraction conditions are the same as in Figure 9. The fringe periodicity in  $\text{LiFeO}_2$  is half of that in  $\text{LiFe}_5\text{O}_8$ . Note the small ordered domains in the precipitate.
- Figure 11 (a-c) Selected area diffraction patterns from  $\text{LiFe}_5\text{O}_8$ ,  $\text{LiFeO}_2 + \text{LiFe}_5\text{O}_8$  and  $\text{LiFeO}_2$  regions respectively. Note the diffuse scattering in (b) and (c) arising due to short range order in  $\text{LiFeO}_2$ . The indices marked in the reciprocal lattice section in (d) correspond to those of the spots adjacent to the transmitted beam in the direction of the arrows.
- Figure 12 BF and DF images of  $\text{LiFeO}_2$  in  $\text{LiFe}_5\text{O}_8$ .  $\text{DF}_1$  and  $\text{DF}_2$  are taken using spots 1 and 2 marked in the diffraction pattern in the inset (BF image). Note the presence of diffuse scattering from  $\text{LiFeO}_2$  in the diffraction pattern.

Figure 13 BF Micrographs showing (a) isolated  $\text{LiFeO}_2$  precipitates as they lose coherency with the matrix, (b) two semicoherent precipitates as they coalesce, (c) precipitates growing preferentially on dislocations, (d) part of a long  $\text{LiFeO}_2$  precipitate (B) due to the anisotropic nature of the growth. The morphology in (d) is due to impingement of a row of growing precipitates.

Figure 14 (a) and (b) are images of precipitate-matrix interface dislocations  $\{\text{LiFeO}_2 - \text{LiFe}_5\text{O}_8\}$  imaged in different diffracting conditions so as to show one set of the interfacial dislocations in contrast at one time. The figures show only part of a long  $\text{LiFeO}_2$  precipitate in a thick foil.

Figure 15 (a) BF image of a small angle boundary in the transformed  $\text{LiFe}_5\text{O}_8$  with the second order reflection excited. Foil normal near  $[110]$  pole. (b) Symmetrical  $[110]$  electron diffraction pattern with the selected area aperture covering portions of the grains on either side of the boundary in (a).

Figure 16 (a) BF image of uniformly dispersed amorphous particles in  $\text{LiFe}_5\text{O}_8$  matrix after annealing in air. (b) Amorphous particles growing preferentially at the semicoherent  $\text{LiFeO}_2 - \text{LiFe}_5\text{O}_8$  interface in vacuum annealed  $\text{LiFe}_5\text{O}_8$

Figure 17 BF image showing portion of a long  $\text{LiFeO}_2$  precipitate in  $\text{LiFe}_5\text{O}_8$  annealed in one atmosphere of oxygen at  $1200^\circ\text{C}$ . The second order reflection for the matrix (or the first order spot for the precipitate) is used to image the interface dislocations, which are dissociated as  $\frac{1}{2}\langle 110 \rangle = \frac{1}{4}\langle 110 \rangle + \langle 110 \rangle$ .

Figure 18 Semicoherent  $\text{LiFeO}_2$  precipitates (a) on a grain boundary and (b) in the grain interior in  $\text{LiFe}_5\text{O}_8$  polycrystals. Note the precipitates A and B in (a) growing into grain 2 but retaining a flat interface with respect to grain 1.

Figure 19 BF image showing the duplex microstructure in a large  $\text{LiFe}_5\text{O}_8$  crystal. I is part of a semicoherent  $\text{LiFeO}_2$  precipitate in the matrix II, and is imaged with the matrix 004 reflection excited.

Figure 20 Sketch of the isothermal ternary section of the  $\text{FeO}-\text{Fe}_2\text{O}_3 - \text{LiFeO}_2$  phase diagrams from ref. 31.  $A \rightarrow B \rightarrow C$  is the schematic direction of the transformation path.

Figure 21 Scanning electron micrograph of the  $\{111\}$  surface of  $\text{LiFe}_5\text{O}_8$ , heated for the three hours in vacuum at  $1200^\circ\text{C}$ . The surface is spongy with nearly flat pore-bottoms.

- Figure 22 Same as in Figure 21 of the  $\{110\}$  surface of  $\text{LiFe}_5\text{O}_8$ . Note the growth-step topography. The directions parallel to the facets are indicated.
- Figure 23 Same as Figure 22, heated for 15 minutes in vacuum ( $10^{-5}$  torr) at  $1200^\circ\text{C}$ . The step-like structure is starting to form at A. The heat treatment corresponds to the microstructure in Stage II of Figure 7.
- Figure 24 Sketch to show the periodic charge distribution on two parallel planes P and P', and the geometrical relationships discussed in Section III.B.4.
- Figure 25 Photograph of a flux grown octahedral  $\text{MgAl}_2\text{O}_4$  single crystal showing two of its faces. The  $[110]$  direction is normal to the plane of the photograph. (5x)
- Figure 26 JSM U-3 scanning electron micrograph of a  $\{111\}$  surface of  $\text{LiFe}_5\text{O}_8$  etched in  $\text{H}_3\text{PO}_4$  at  $195^\circ\text{C}$  for 15 minutes. The specimen is gold coated. The three other  $\{111\}$  planes are attacked preferentially by the etchant to expose them; they appear as the three surfaces of a tetrahedron. The edges are etched out in the micrograph.

Figure 27 Schematic representation of the surface morphology in a decomposition reaction. (1) Specimen surface before heating, (2) Reaction front, (3) Residual product richer in A and (4) Pores from which B escapes.

Figure 28 An isolated cation fault with  $R = \frac{1}{4}[011]$  in  $\text{LiFe}_5\text{O}_8$  imaged under different diffracting conditions. Note the symmetry of the  $\pi$ -fringes in the dark field image in (a) and the complementary nature of the bright field and dark field images in (a) and (b). The fault is out of contrast when  $\vec{g} \cdot R = 0$  or integral as in e or f and c, but the bounding partials are out of contrast only when  $\vec{g} \cdot b = 0$ . The width of the dislocation image in (f) is reduced when the 008 reflection is excited.

Figure 29 High order bright field image of straight parallel dislocations with Burgers vector  $\frac{1}{2}[011]$  lying in the plane of the foil, parallel to  $[111]$  direction which is the line of intersection of the (110) foil plane and the (011) slip plane.

Figure 30 Bright field image of healed cracks in lithium ferrite spinel deformed at 1200°C.

Figure 31 (a) High resolution dark field image of dissociated dislocation network in deformed lithium ferrite spinel, (b) microdensitometer trace at A in Fig. (a), (c) computed image profile for the dissociation  $\frac{1}{2}[01\bar{1}] = \frac{1}{4}[01\bar{1}] + \frac{1}{4}[01\bar{1}]$  on (011) plane.

Figure 32 (a) Weak beam image of a dissociated dislocation. The dissociation can be represented as  $\frac{1}{2}[01\bar{1}] = \frac{1}{4}[01\bar{1}] + \frac{1}{4}[011]$ , on the (011) plane. (b) High order bright field image of the same dislocation. Note the four intensity peaks in (a) due to dynamical scattering effects.

Figure 33 (A) Octahedral coherent precipitates of  $\text{LiFeO}_2$  dispersed in  $\text{LiFe}_5\text{O}_8$ . (B) Semicoherent  $\text{LiFeO}_2$  particles with interfacial dislocations of Burgers vector  $\frac{1}{2}\langle 110 \rangle$ . (C) Incoherent grain boundaries in the transformed spinel due to material loss. (D) (a-c) Hysteresis loops corresponding to the microstructures (A-C), (d) hysteresis loop of the single phase  $\text{LiFe}_5\text{O}_8$  single crystal.

Figure 34 (A) Cation stacking faults in  $\text{LiFe}_5\text{O}_8$ . Faults lie on  $\{110\}$  planes with  $\frac{1}{2}\langle 110 \rangle$  displacement vectors. (B) (a) Hysteresis loop corresponding to the microstructure in (A) and (b) same as in Figure 33.D.d.

Figure 35 (A)  $\{110\}_{\frac{1}{4}} \langle 110 \rangle$  cation faults inside a grain in polycrystalline  $\text{NiFe}_2\text{O}_4$ . The grain size is approximately 1.5 microns. (B) (a) Hysteresis loop corresponding to the microstructure in (A). (b) Hysteresis loop on annealing  $\text{NiFe}_2\text{O}_4$  for 12 hours at  $850^\circ\text{C}$  in air.

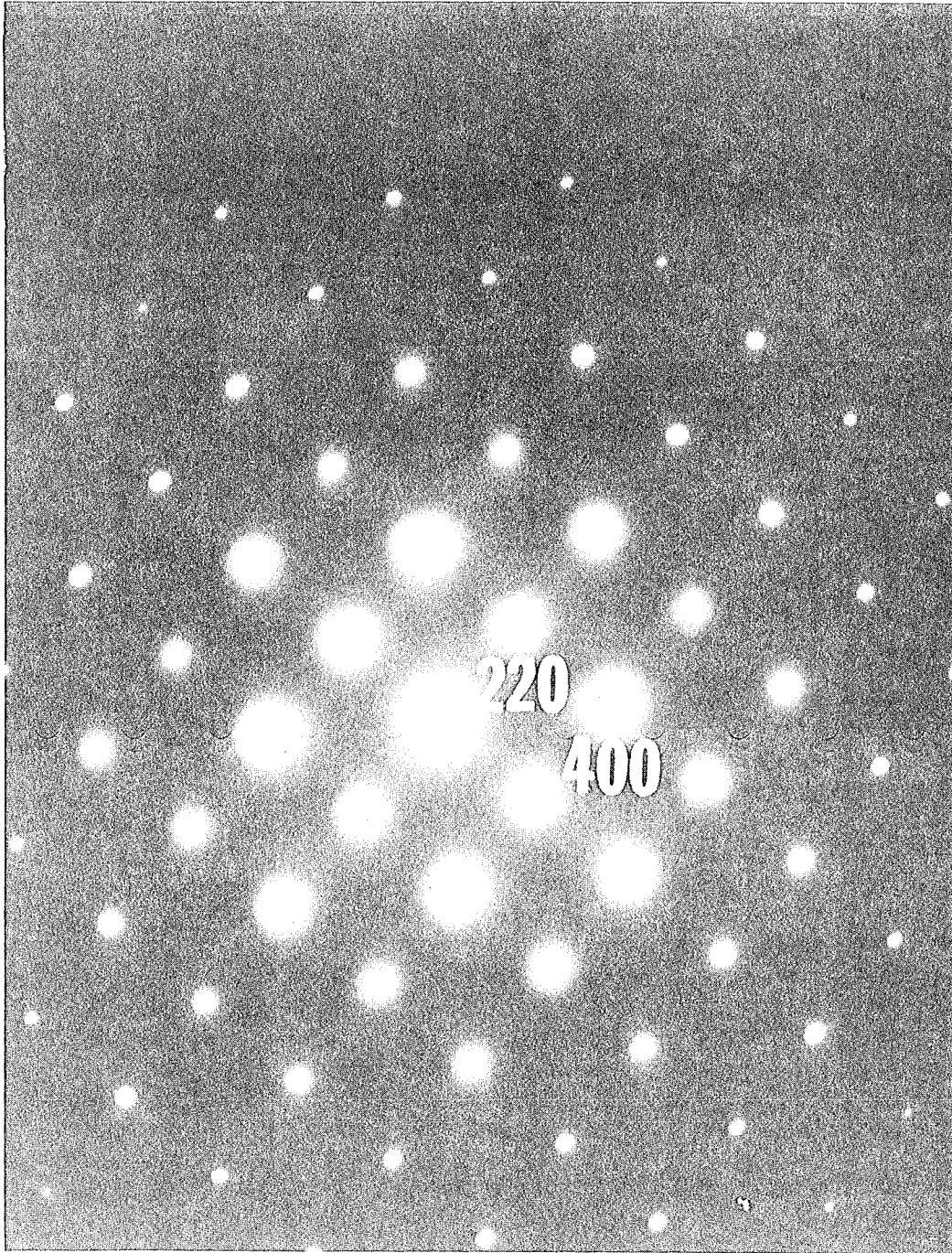
Figure 36 Variation of the DC electrical resistivity of  $\text{LiFe}_5\text{O}_8$  with heat treatment. Typical microstructures of the material are shown beneath the corresponding  $\rho$  values.

n'āsato vidyate bhāvo, n'abhāvo vidyate satah:  
ubhayor api dr̥sto 'ntas tv anayos tattva-darśibhih.

The Bhagavad Gita, II:16

Translation: The unreal has no existence, and the real never ceases  
to be; thus is perceived the reality of both by a  
"researcher."





XBB 7610-9575

Fig. 1

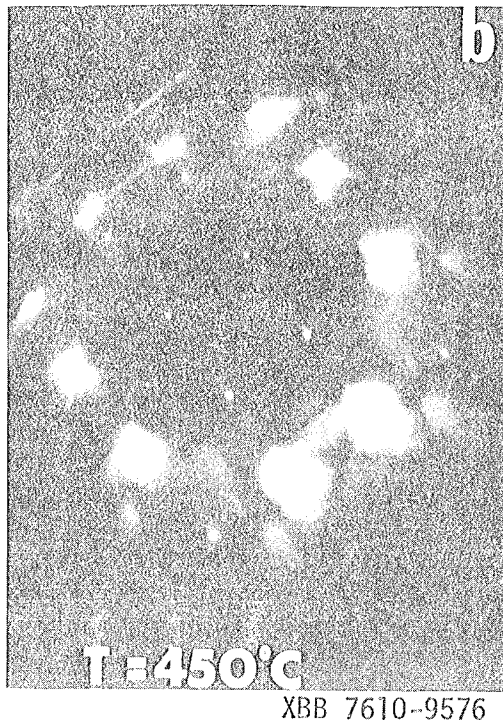
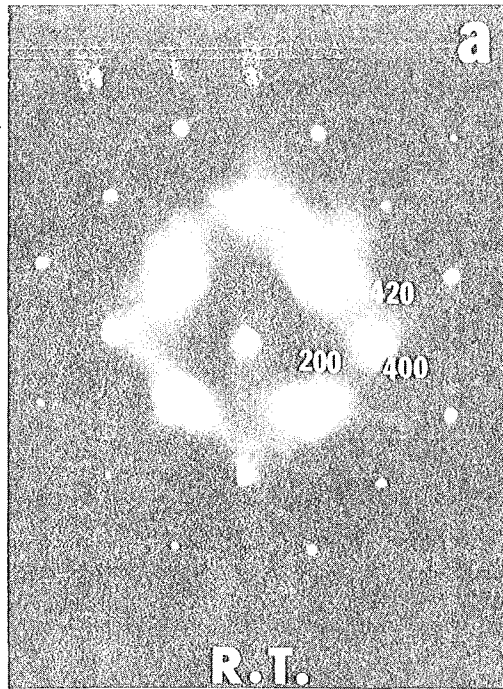


Fig. 2.

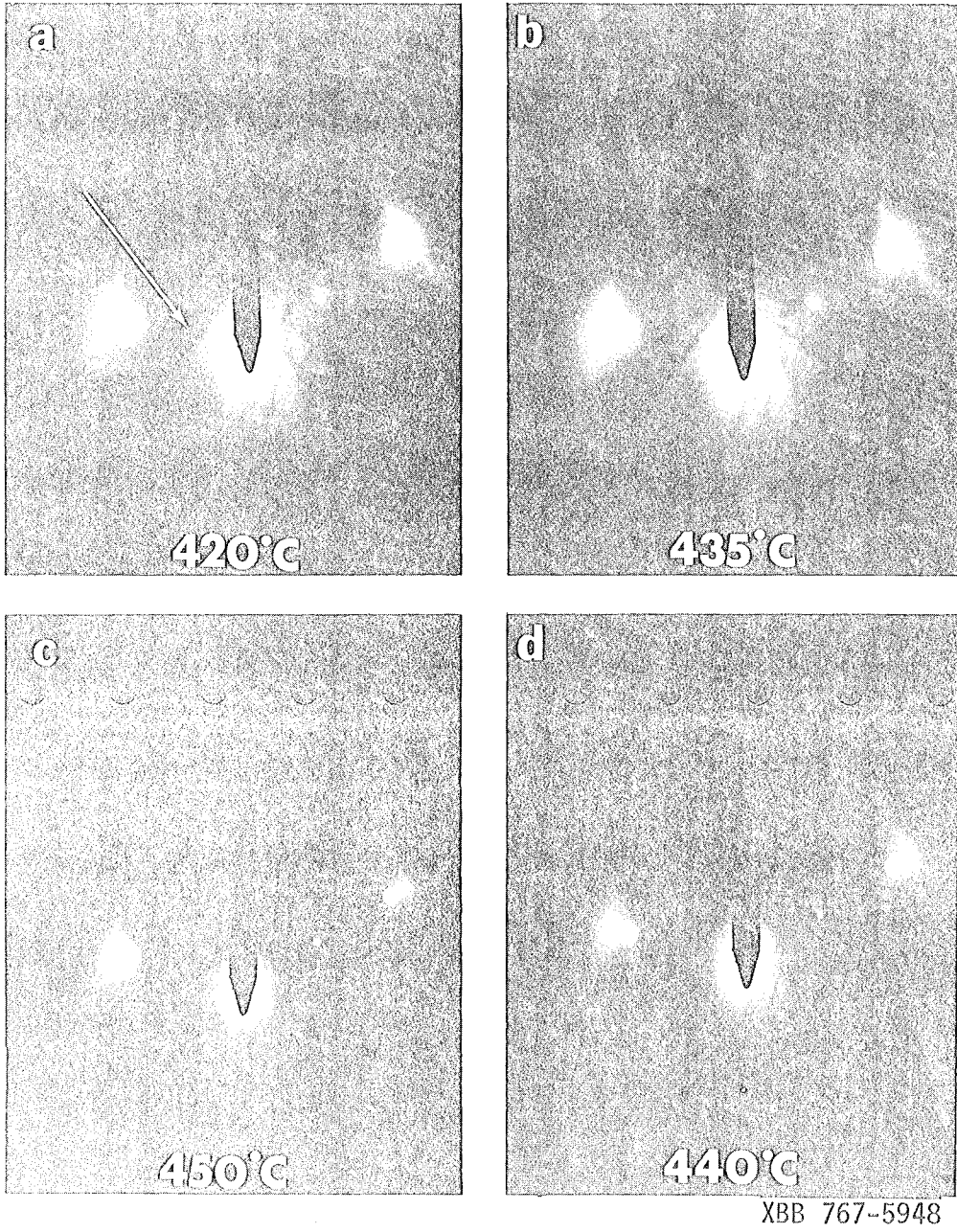
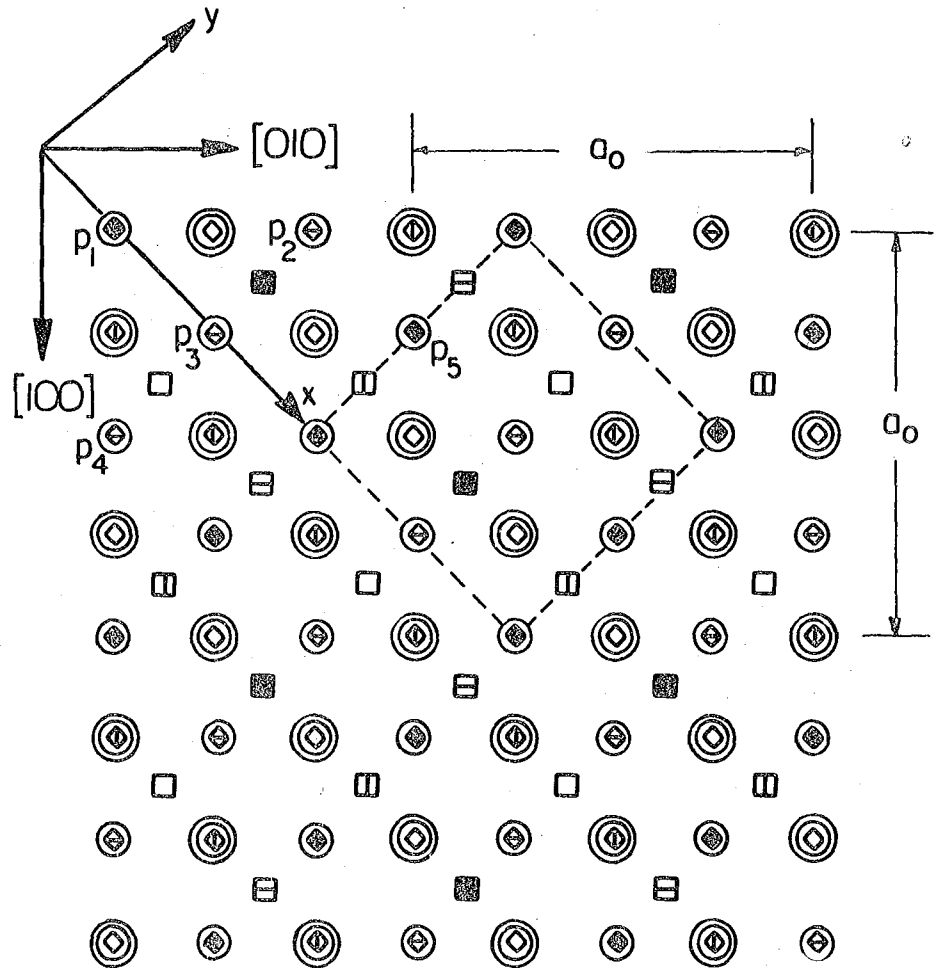


Fig. 3.



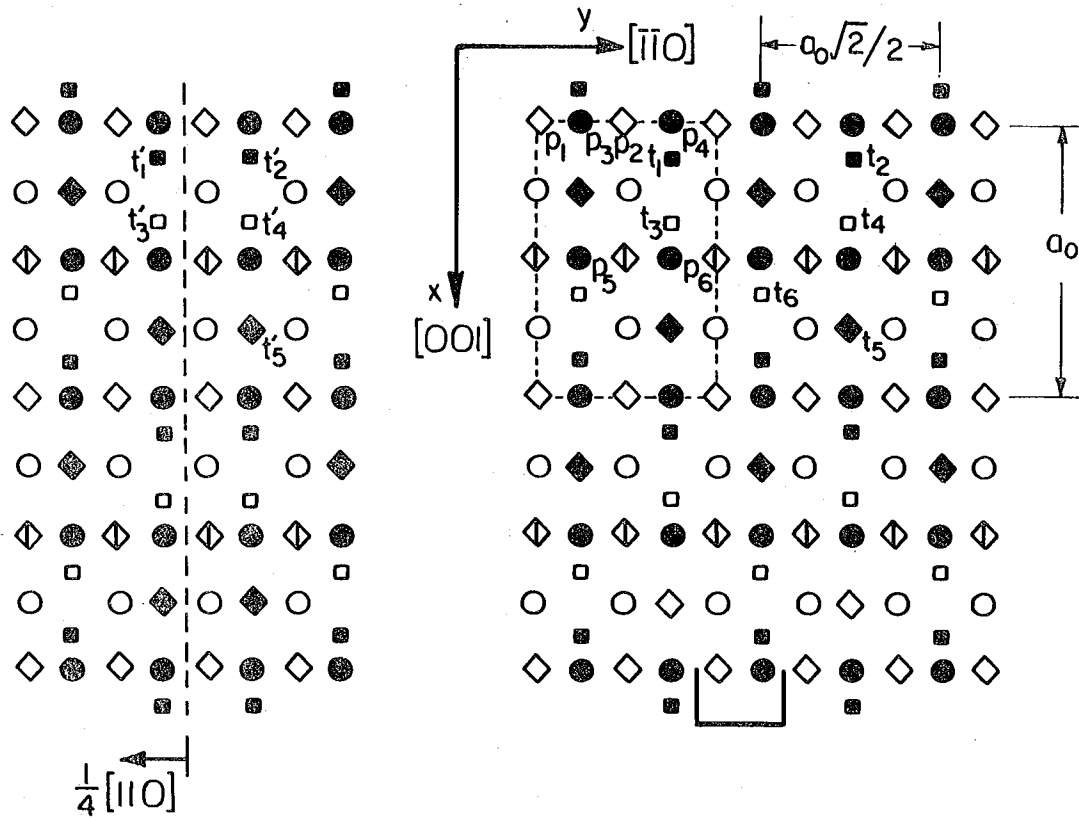
O at		B at				A at			
$\frac{0,4}{\circ}$	$\frac{2,6}{\odot}$	$\frac{0}{\diamond}$	$\frac{2}{\blacklozenge}$	$\frac{4}{\blacklozenge}$	$\frac{6}{\blacklozenge}$	$\frac{1}{\square}$	$\frac{3}{\blacksquare}$	$\frac{5}{\square}$	$\frac{7}{\blacksquare}$

Projection on (001)

Unit Height =  $a_0/8$

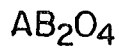
XBL 7510-7435

Fig. 4.



(a) Faulted

(b) Perfect



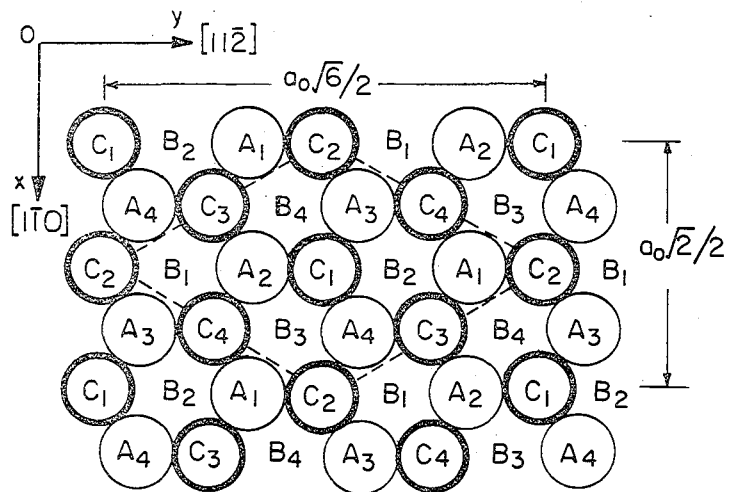
O at		B at			A at	
0, 2	1, 3	0, 2	1	3	1	3
●	○	◆	◇	▽	◻	■

Projection on  $(1\bar{1}0)$   
 Unit Height =  $a_0\sqrt{2}/8$

XBL7510-7433

Fig. 5.

Projection on (111)  
 Unit Height =  $a_0\sqrt{3}/24$   
 Stacking in Spinel Structure  
 in Extended--ABC--Notation  
 Zeroth Layer ( $A_{1-4}$  Kagomé)  
 at Height Zero



Occupied Positions

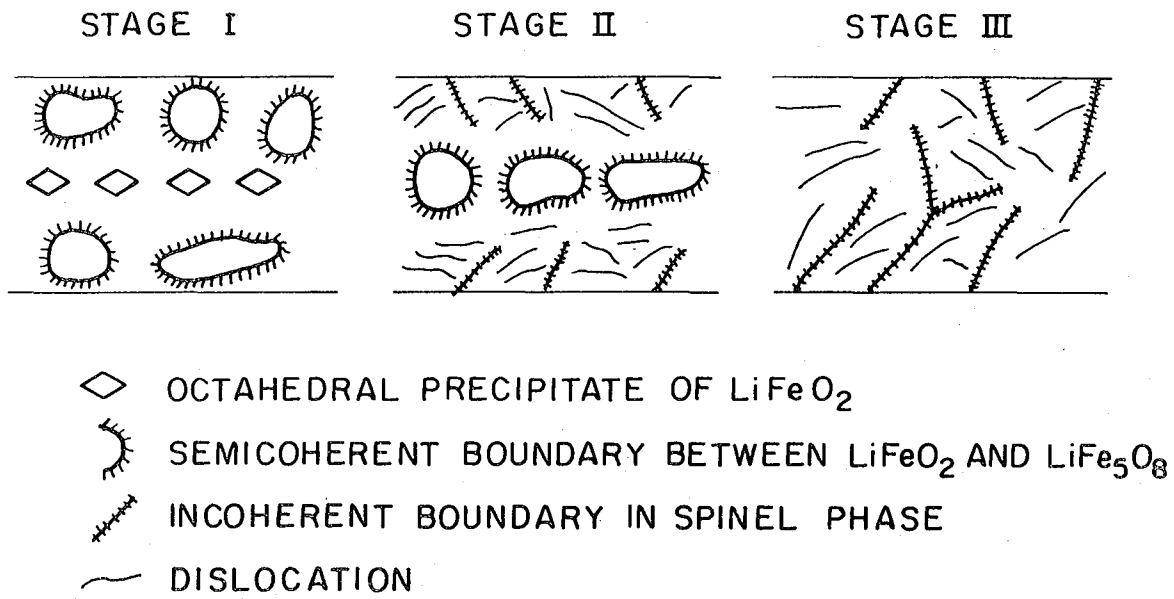
--/A<sub>1-4</sub>/-/C<sub>2-4</sub>/-/B<sub>1-4</sub>/C<sub>1</sub>/A<sub>1</sub>/B<sub>1</sub>/C<sub>1-4</sub>/-/B<sub>2-4</sub>/-/A<sub>1-4</sub>/B<sub>1</sub>/C<sub>1</sub>/A<sub>1</sub>/B<sub>1-4</sub>/-/A<sub>2-4</sub>/-/C<sub>1-4</sub>/A<sub>1</sub>/B<sub>1</sub>/C<sub>1</sub>/A<sub>1-4</sub>/--

Composition in AB<sub>2</sub>O<sub>4</sub>

--/O<sub>4</sub>/-/B<sub>3</sub>/-/O<sub>4</sub>/A/B/A/O<sub>4</sub>/-/B<sub>3</sub>/-/O<sub>4</sub>/A/B/A/O<sub>4</sub>/-/B<sub>3</sub>/-/O<sub>4</sub>/A/B/A/O<sub>4</sub>--  
 ⏟                      ⏟  
 Kagomé              Mixed

XBL 7510-7434

Fig. 6.



XBL 765-6875

Fig. 7.

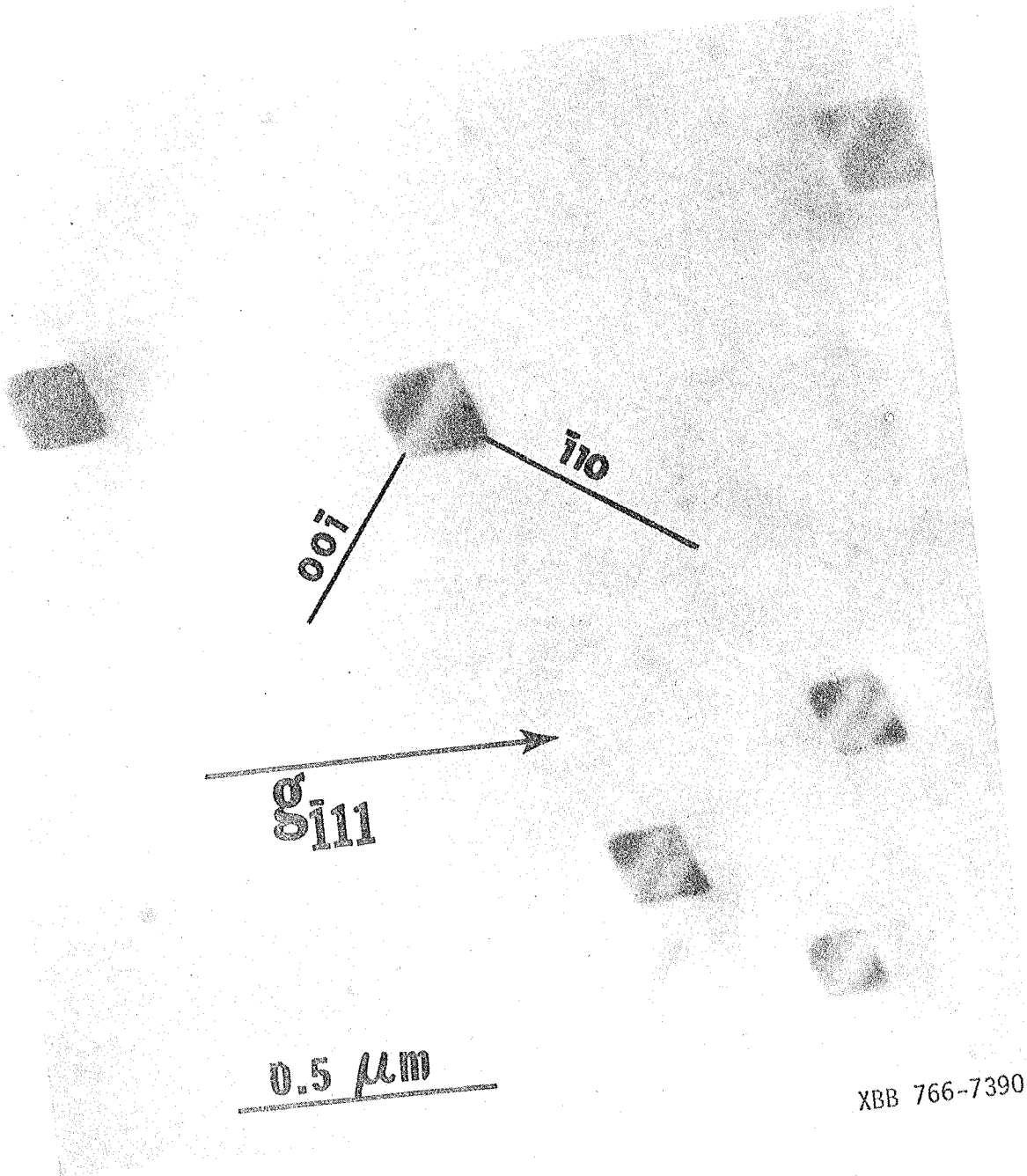


Fig. 8.



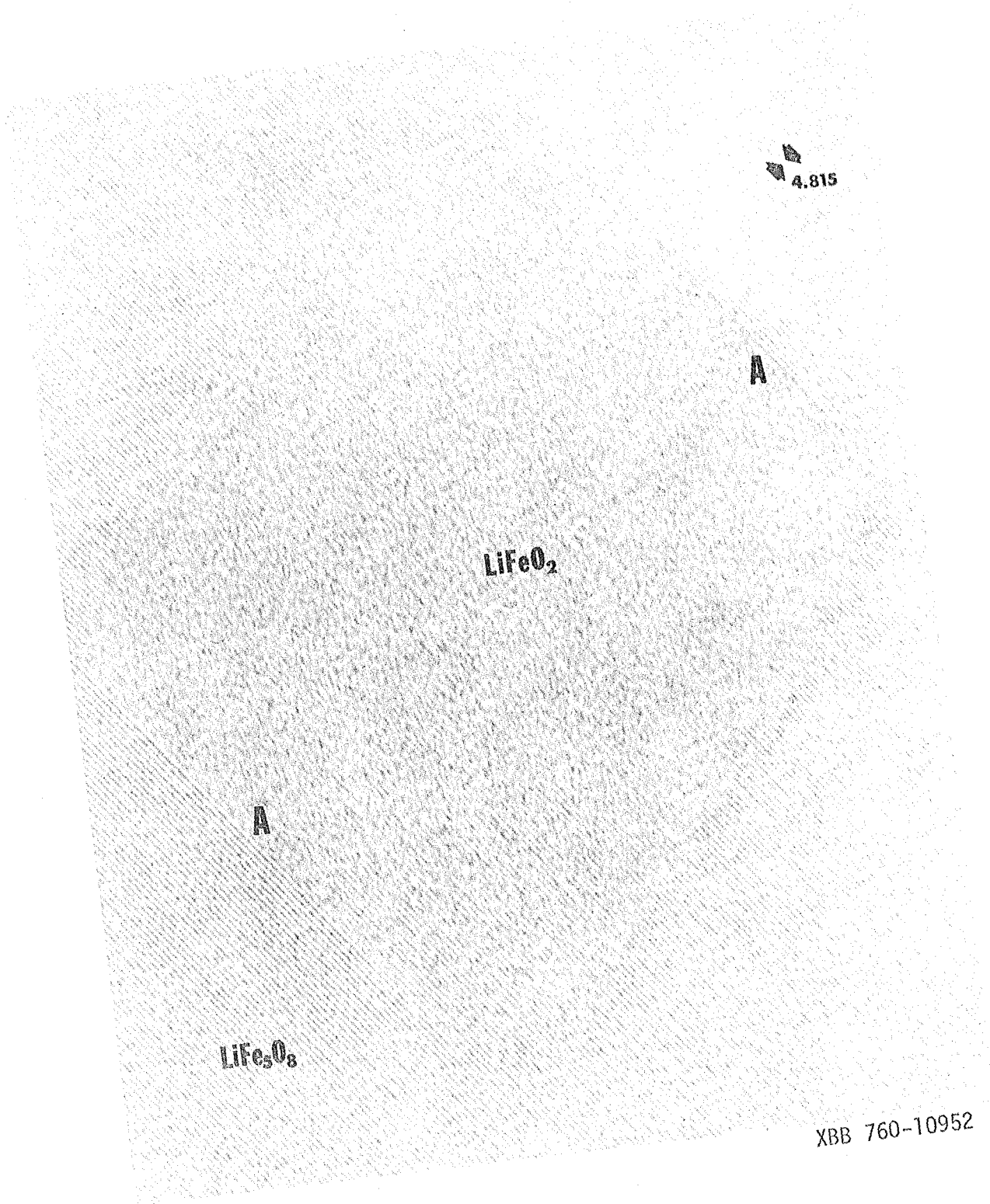
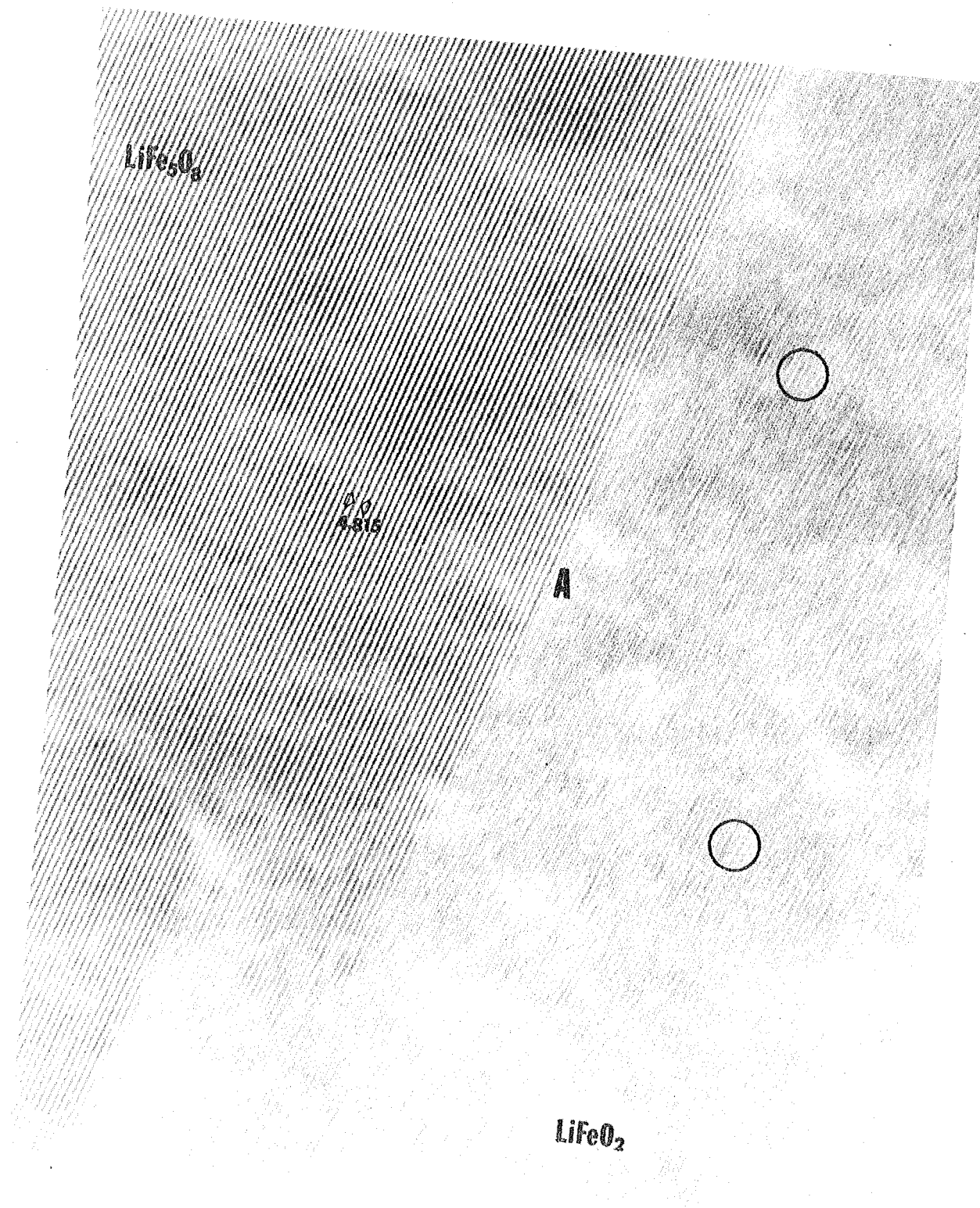
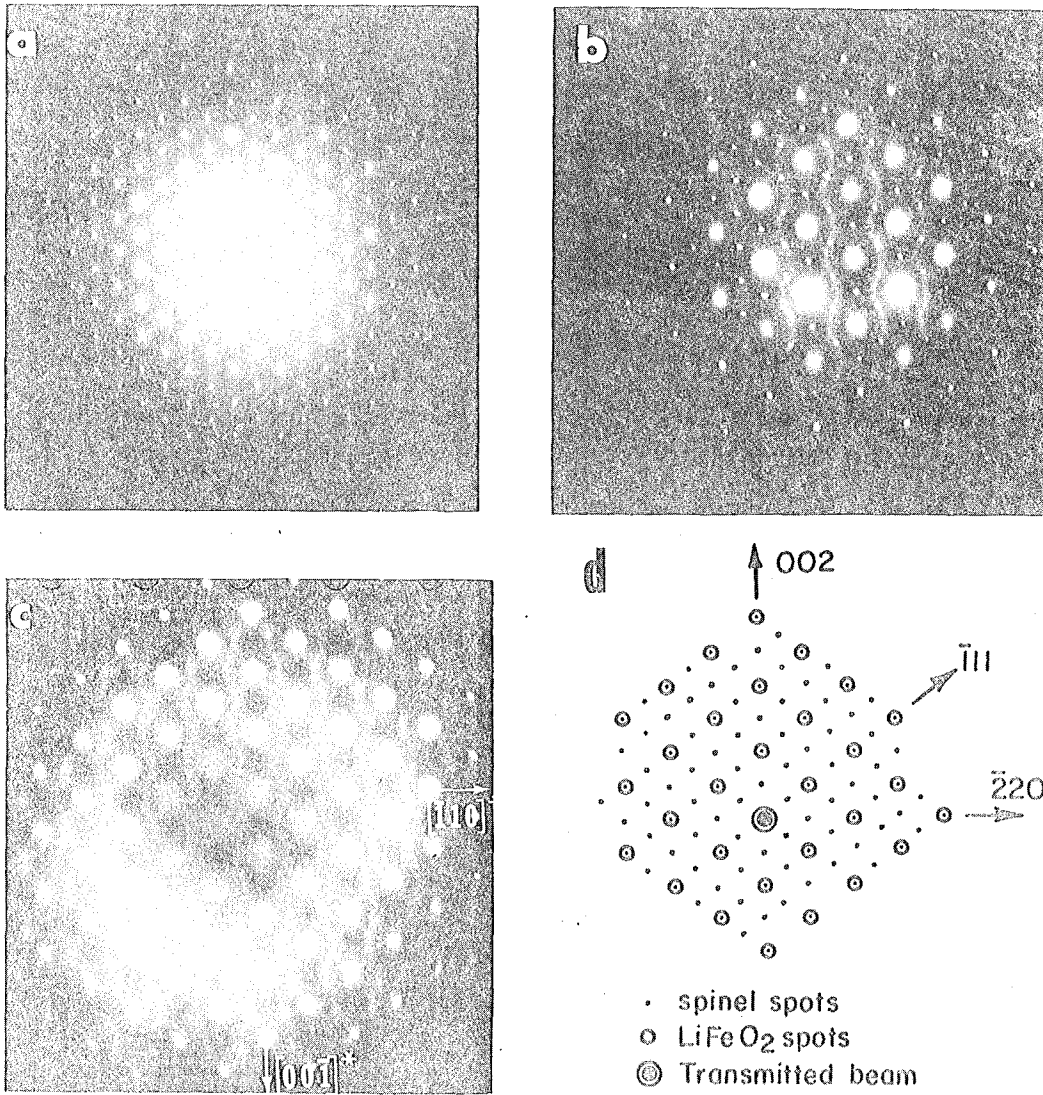


Fig. 9.



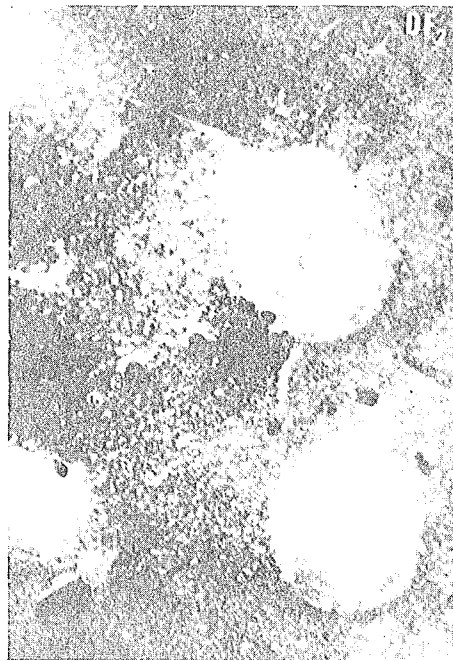
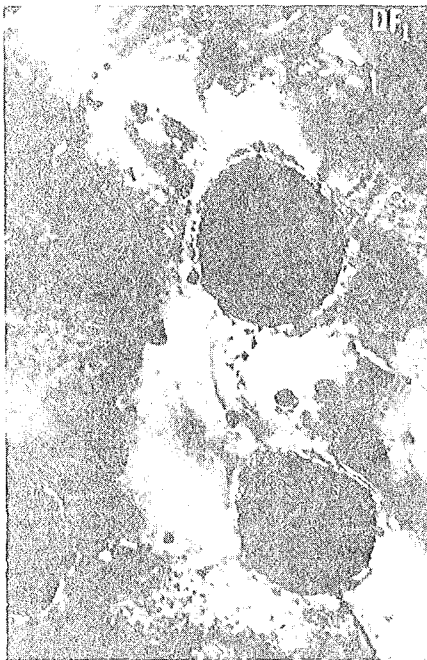
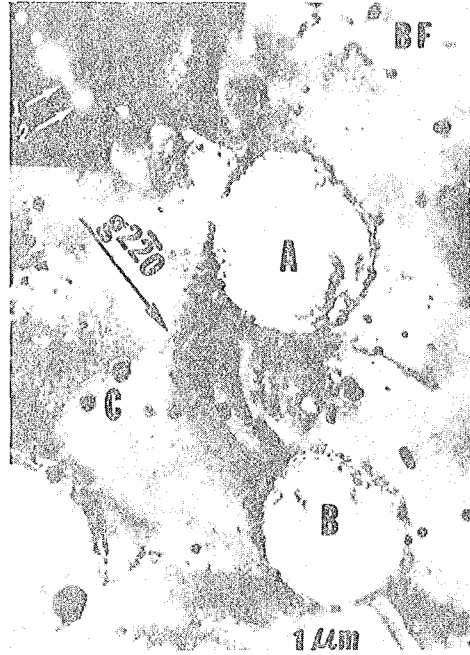
XBB 760-10953

Fig. 10.



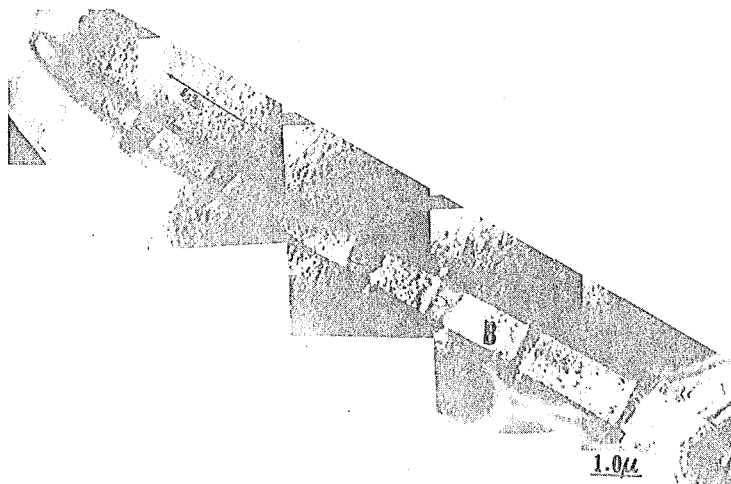
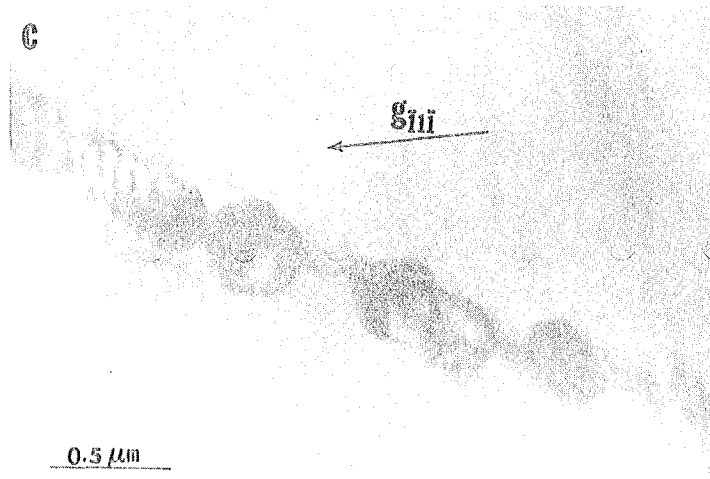
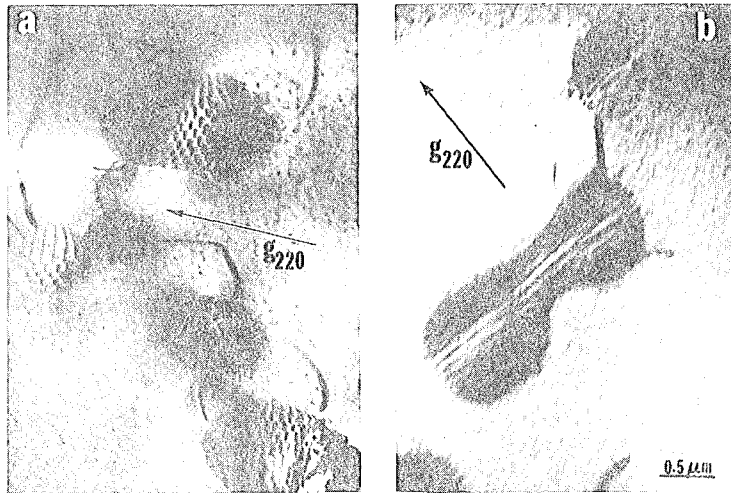
XBB 766-5398

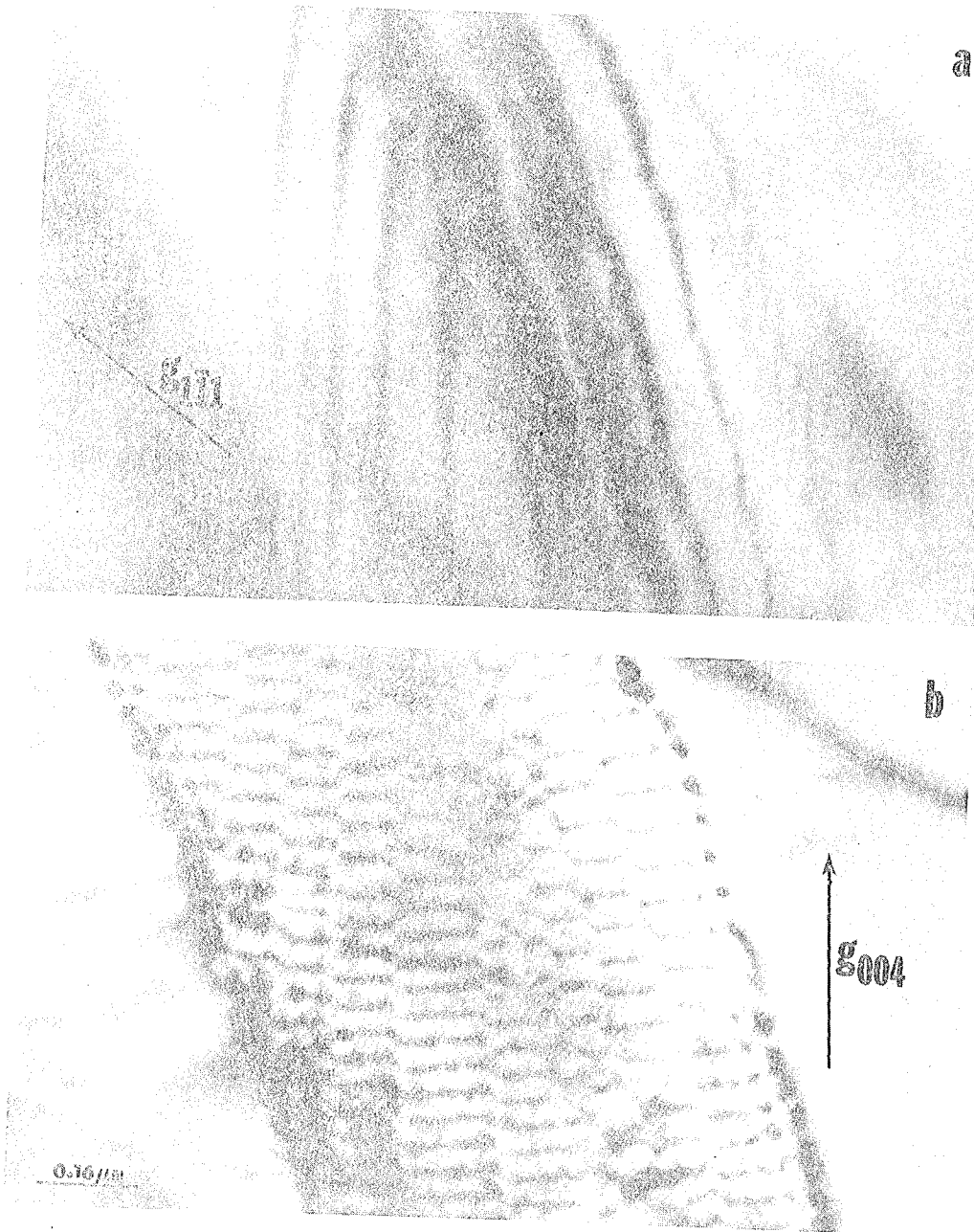
Fig. 11.



XBB 760-10297

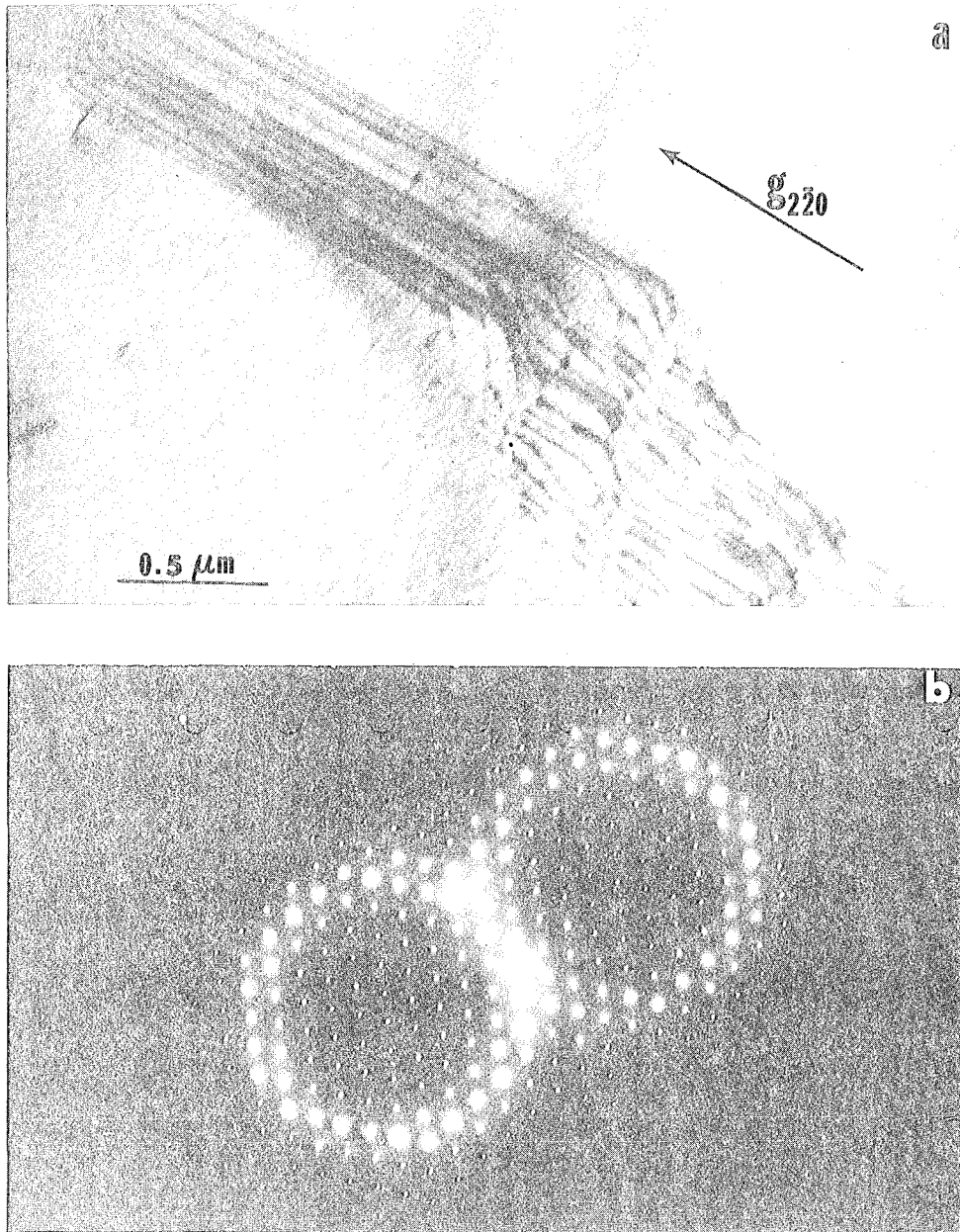
Fig. 12.





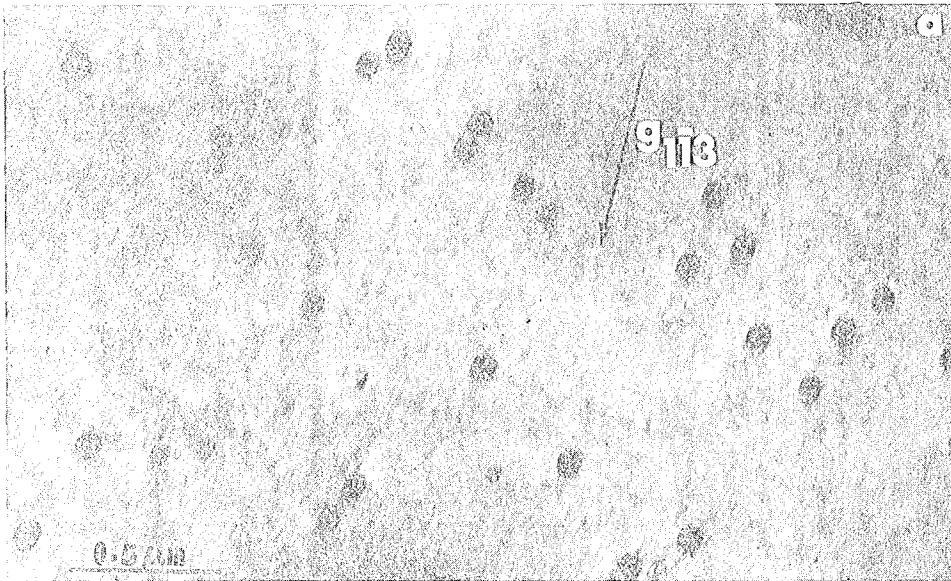
XBB 766-5353

Fig. 14.



XBB 766-5355

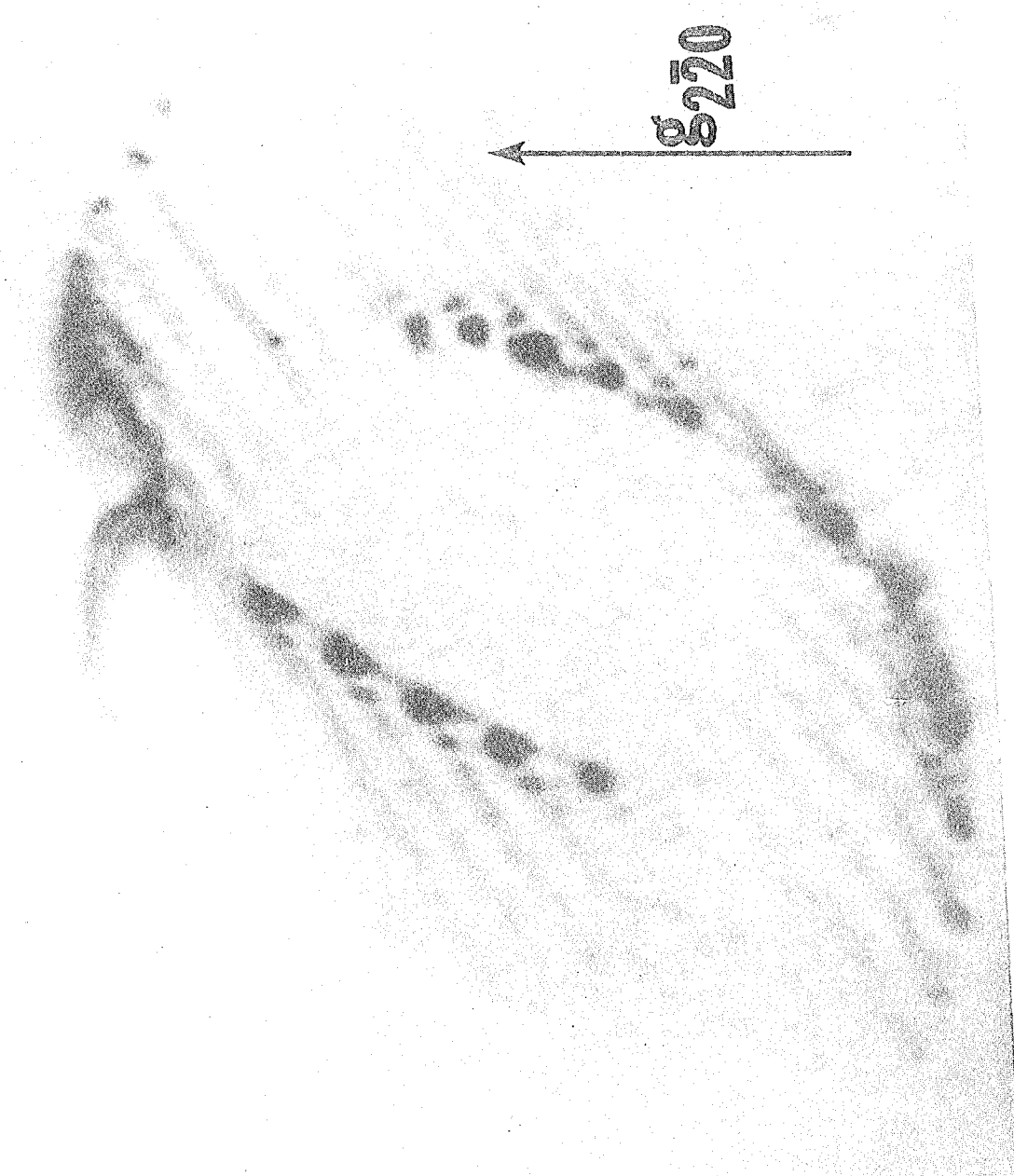
Fig. 15.



XBB 766-5354

Fig. 16.





0.1μ

XBB 766-5357

Fig. 17.

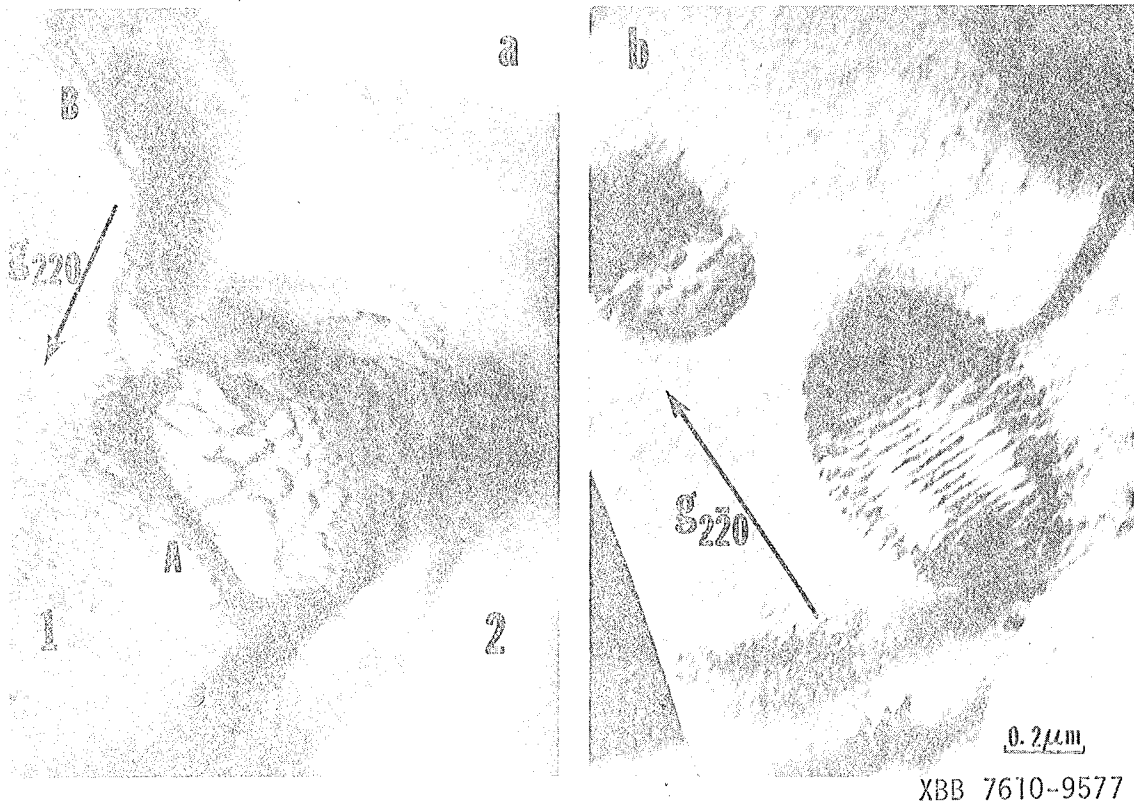
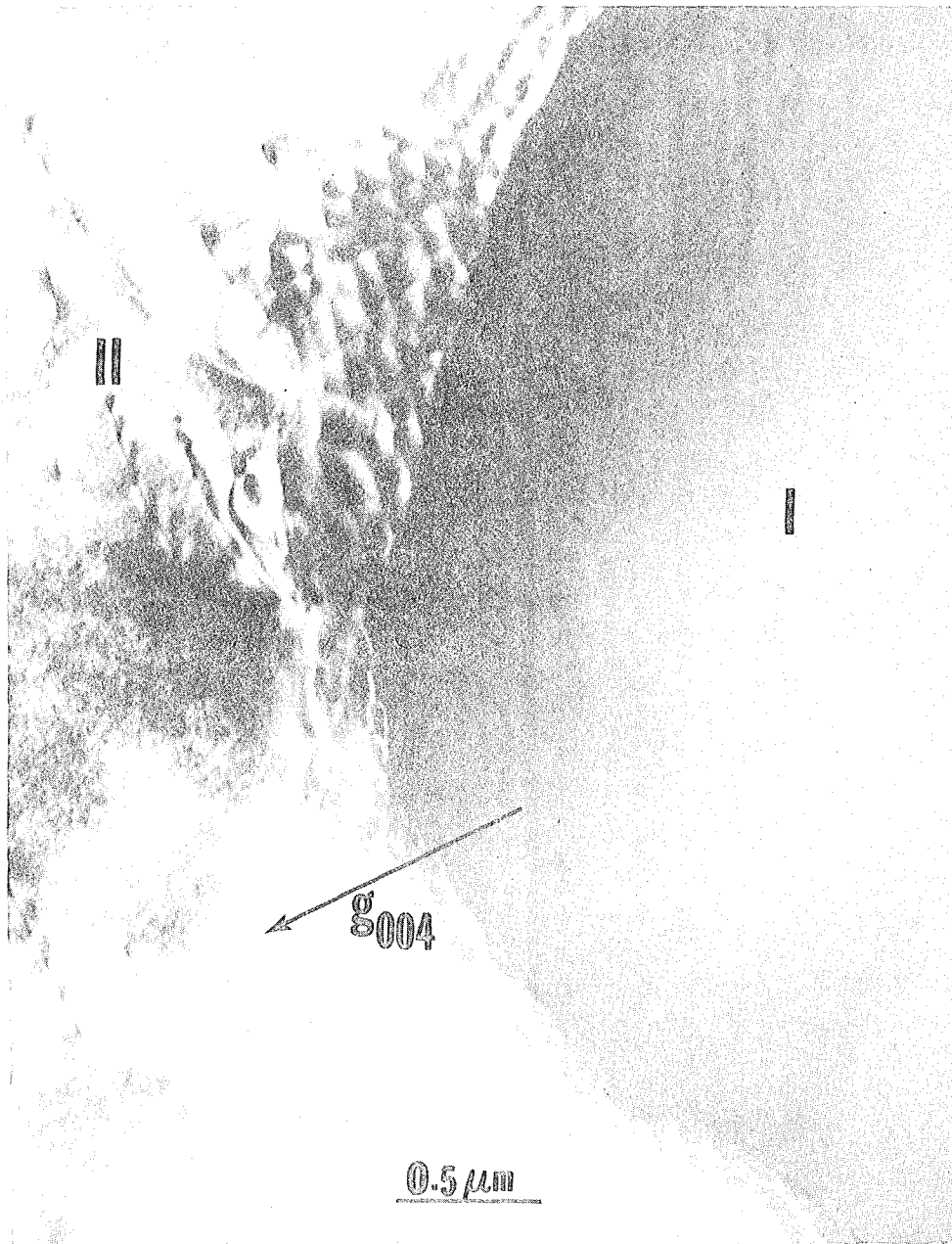
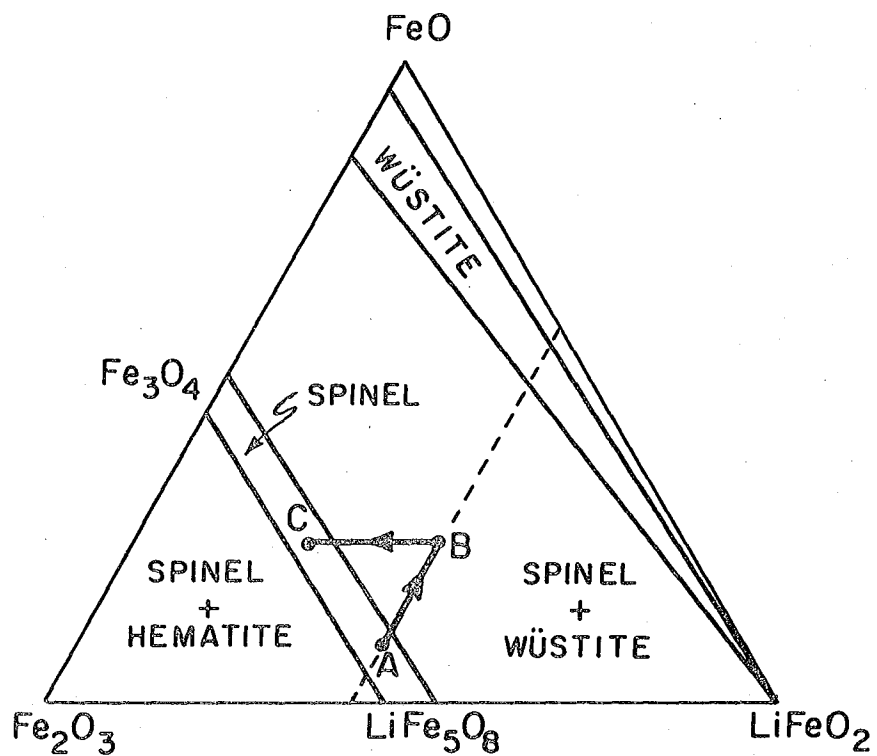


Fig. 18.



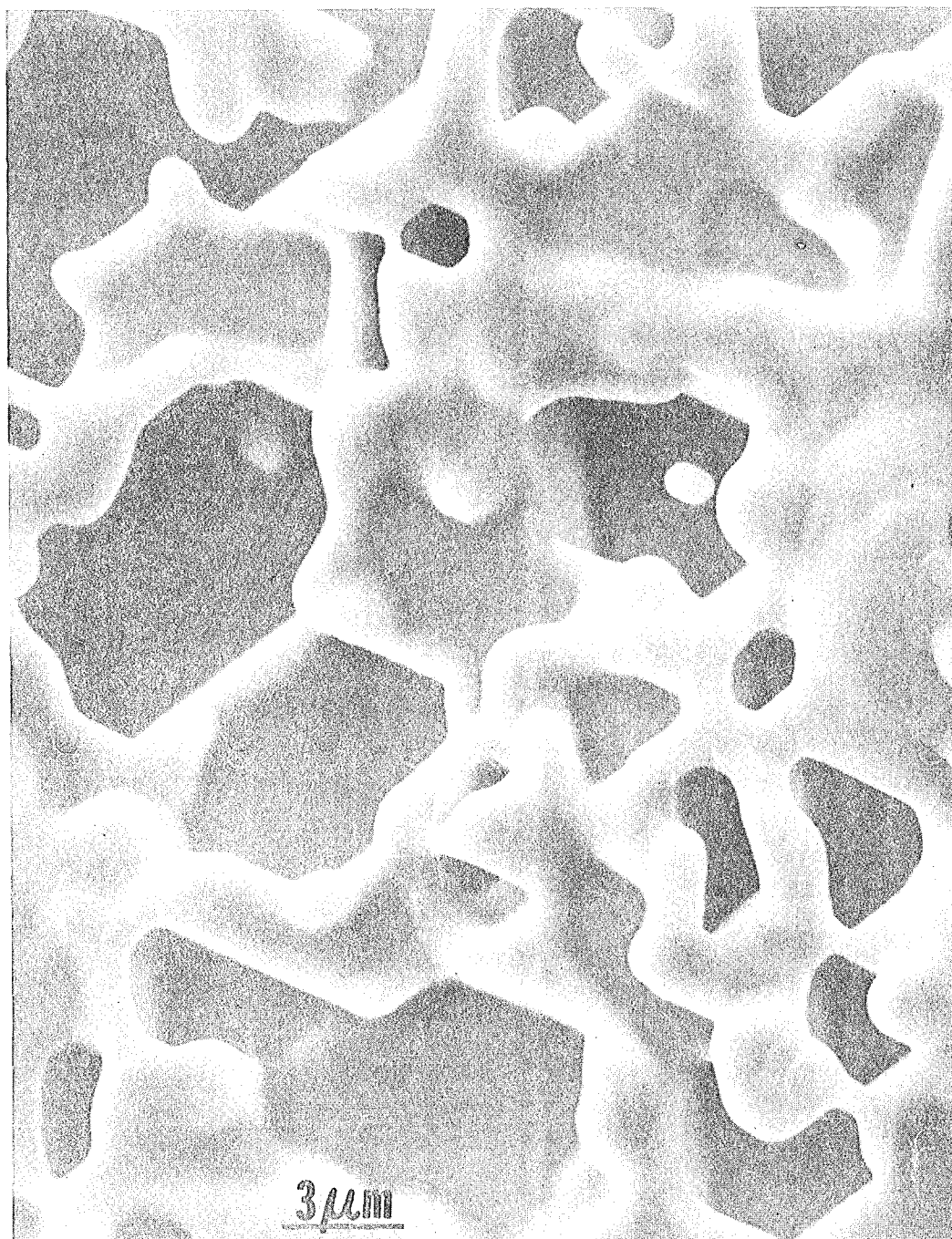
XBB 766-5356

Fig. 19.



XBL 765-1986

Fig. 20.



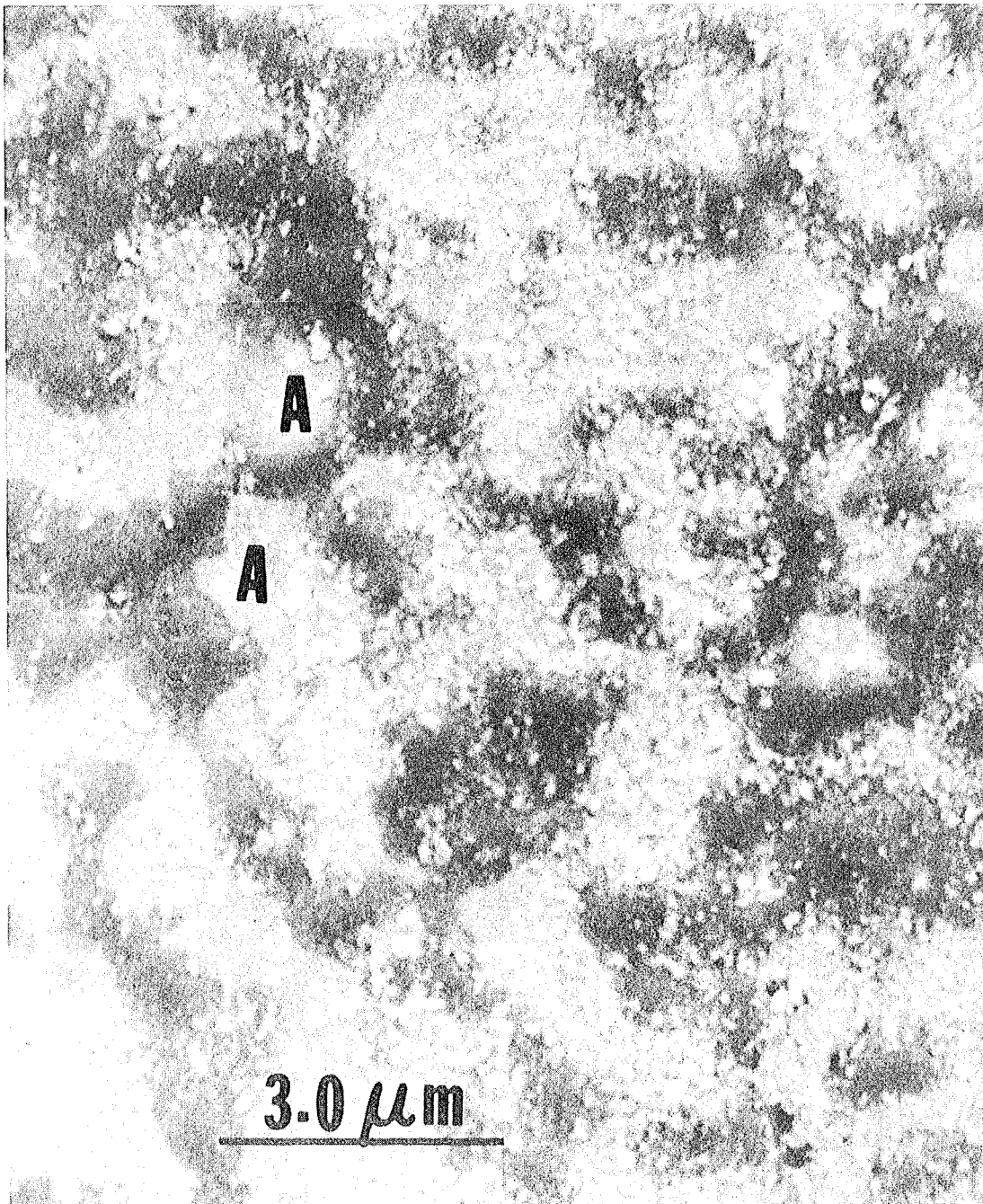
XBB 7511-8376

Fig. 21.



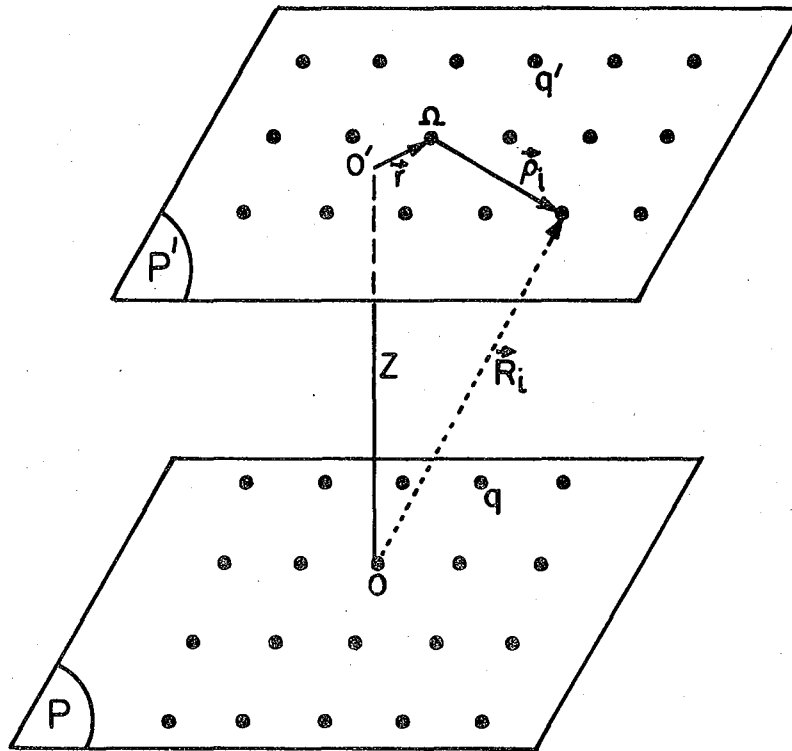
XBB 7511-8377

Fig. 22.



XBB 760-10726

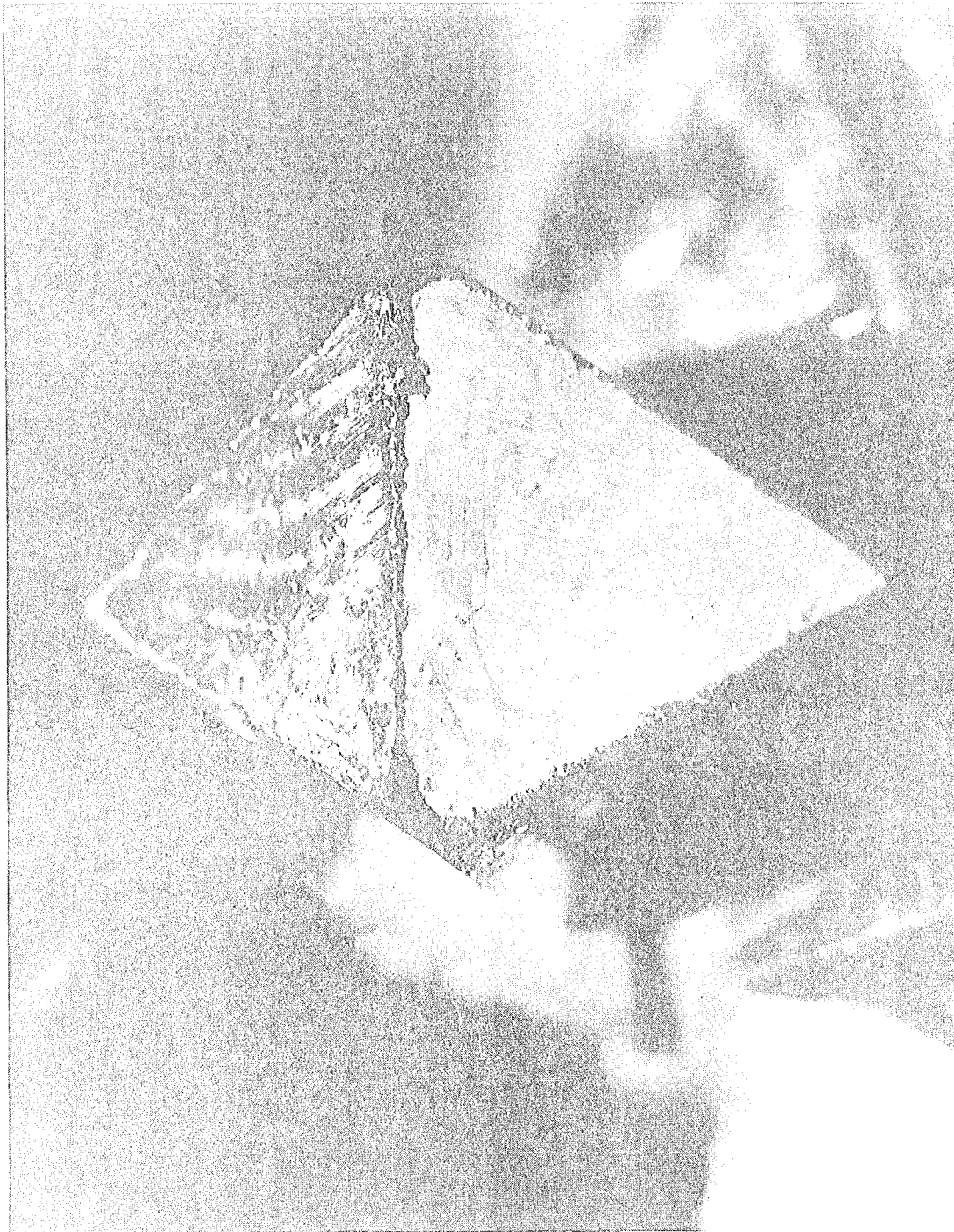
Fig. 23.



XBL 7510-7477

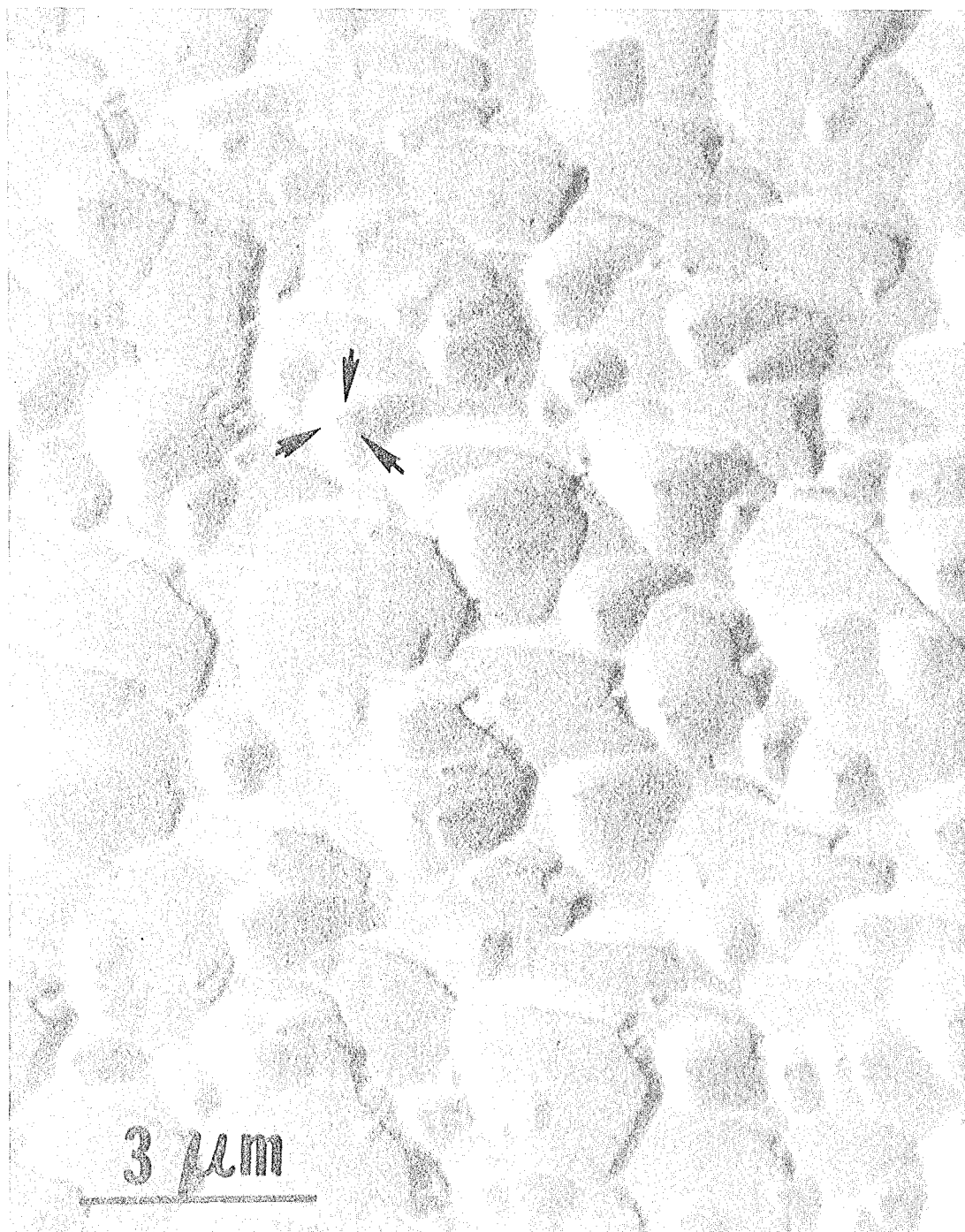
Fig. 24.





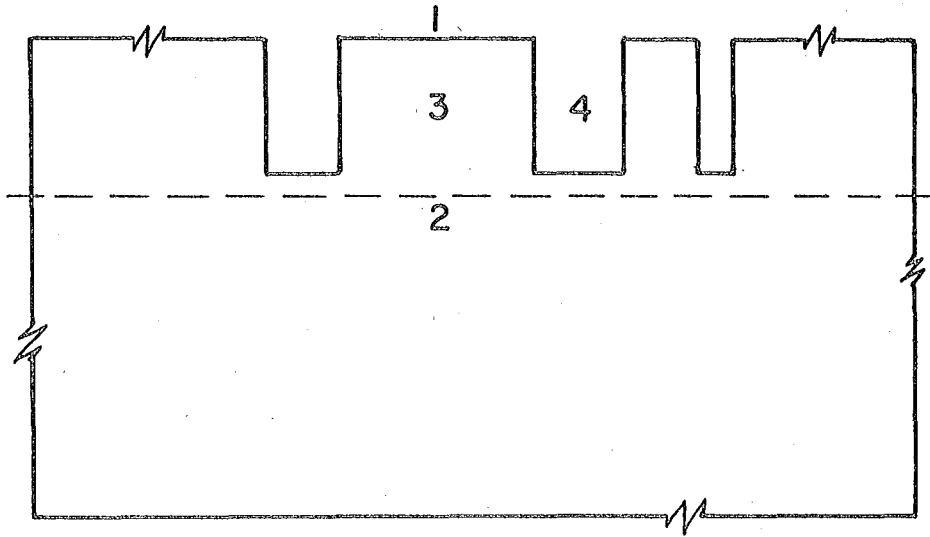
XBB 764-3092

Fig. 25.



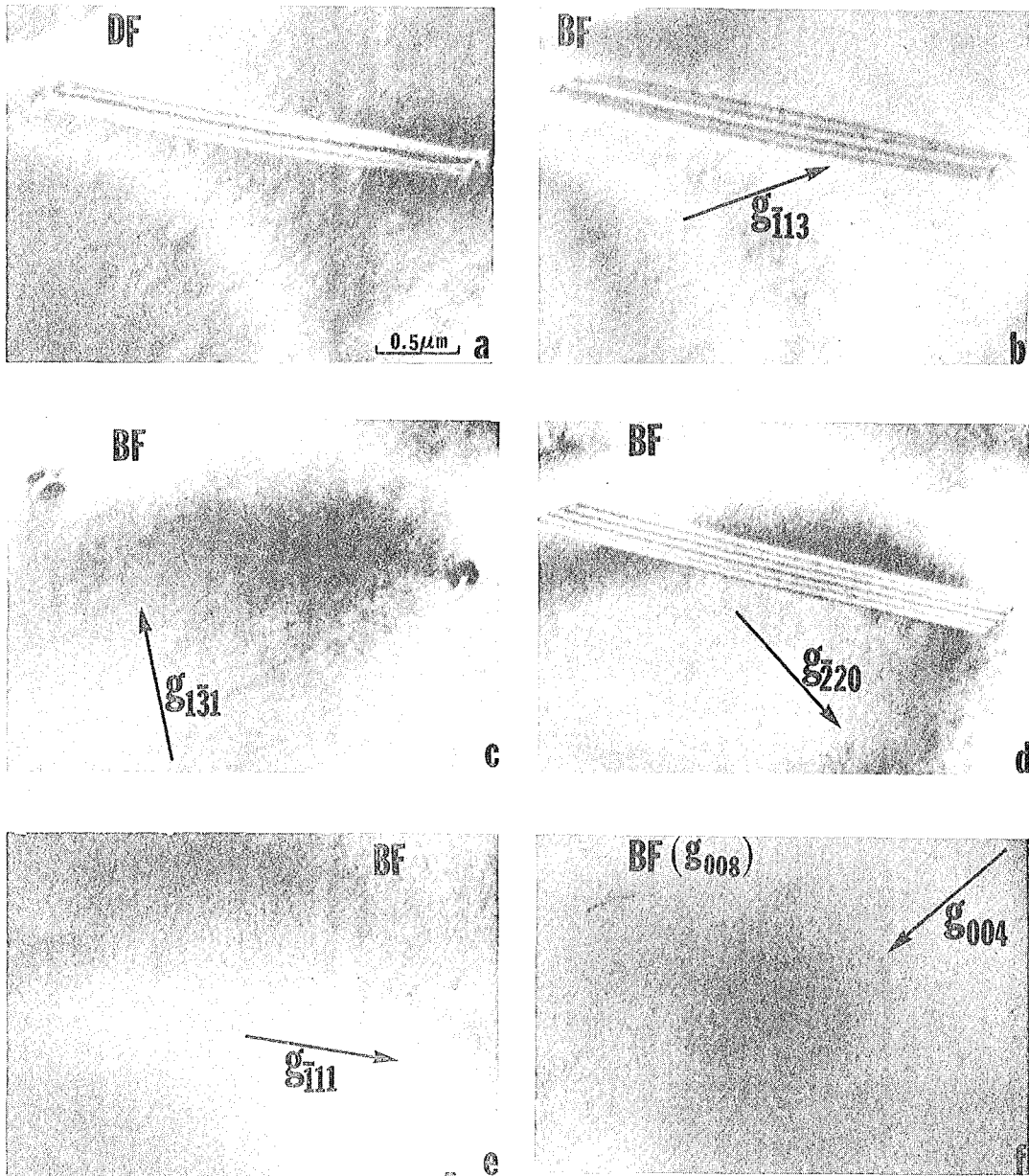
XBB 760-10727

Fig. 26.



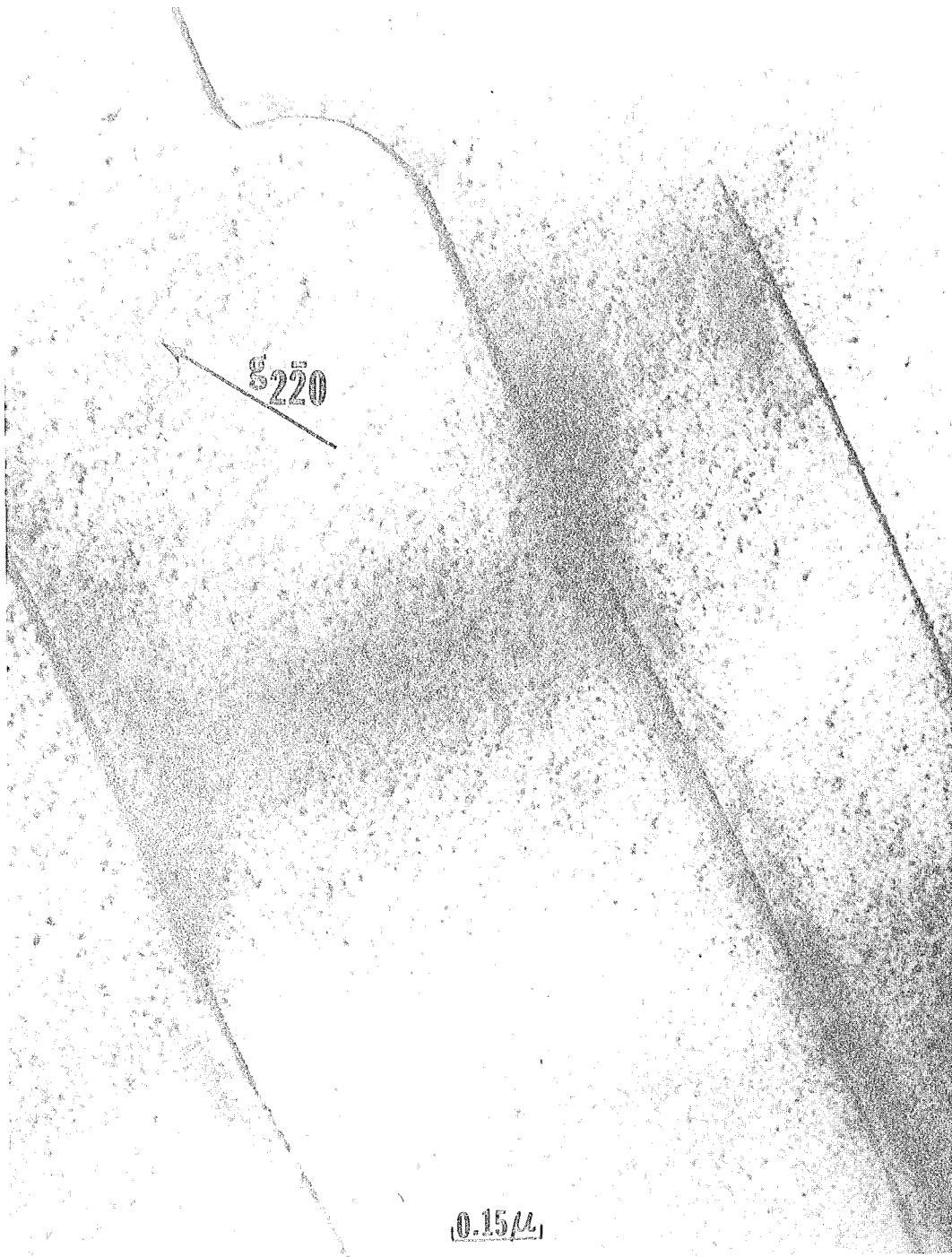
XBL 7512-10,008

Fig. 27.



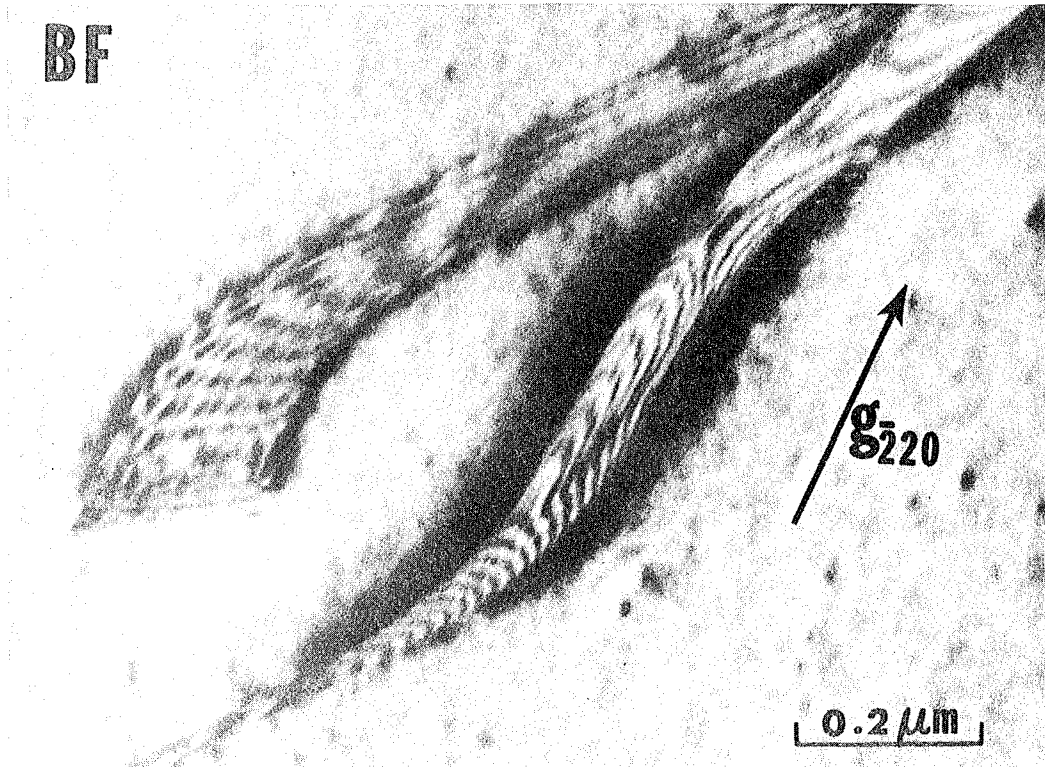
XBB 759-6526

Fig. 28.



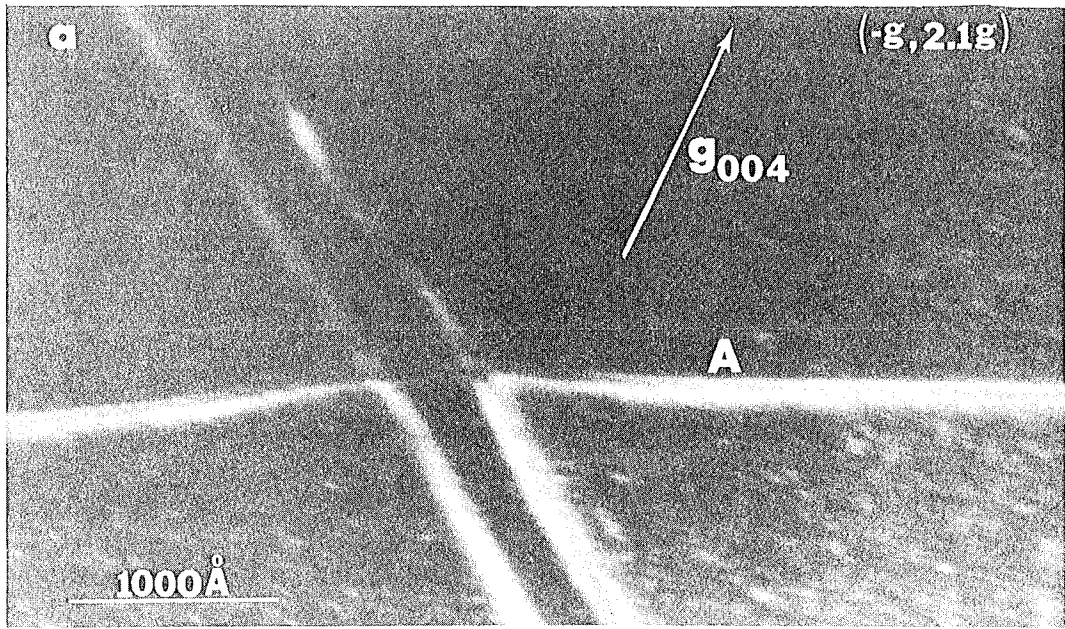
XBB 769-8344

Fig. 29.

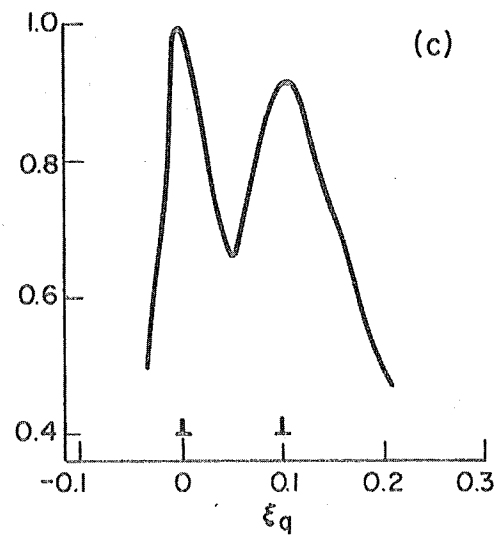
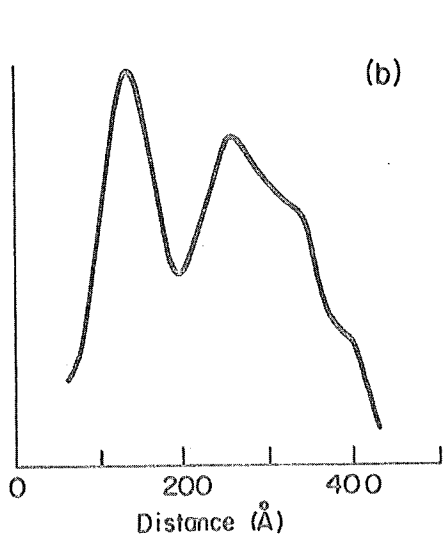


XBB 769-8343

Fig. 30.



XBB 767-6592



XBB 767-6592

Fig. 31

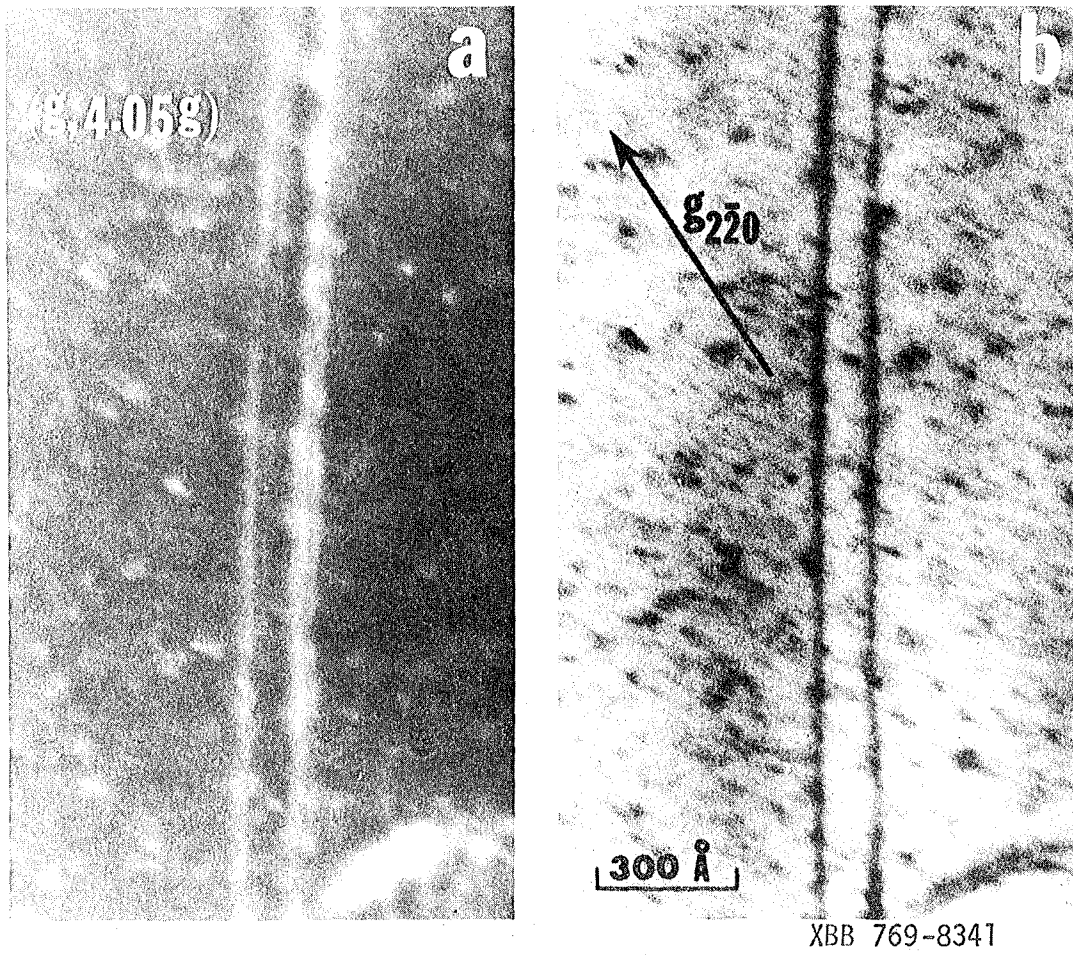
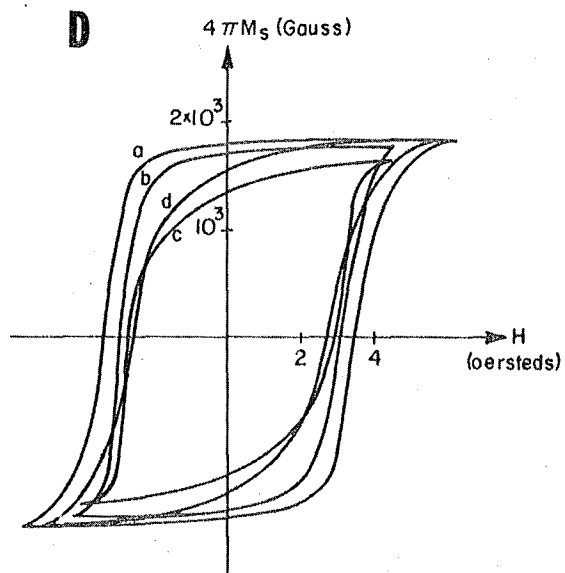
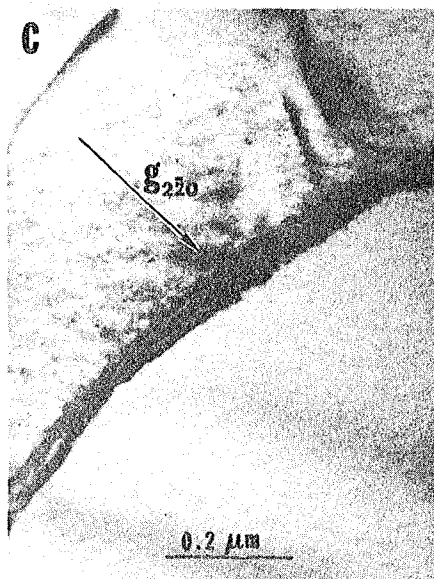
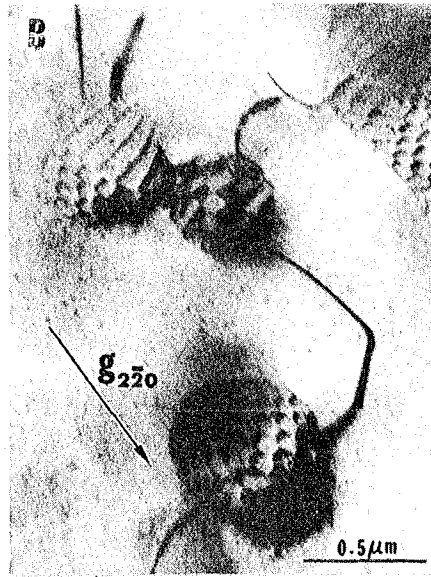
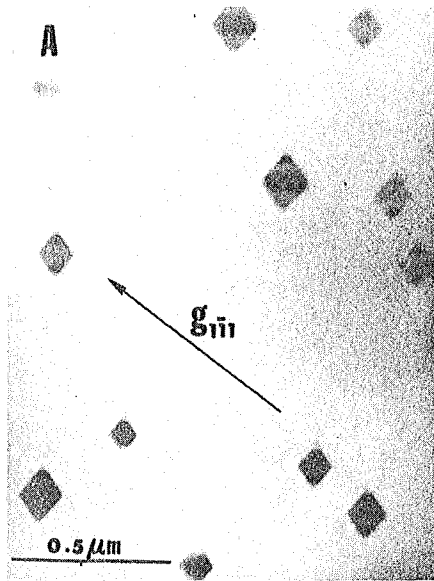


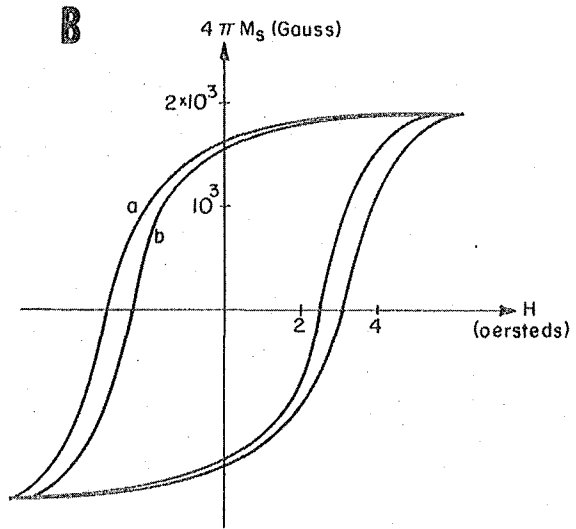
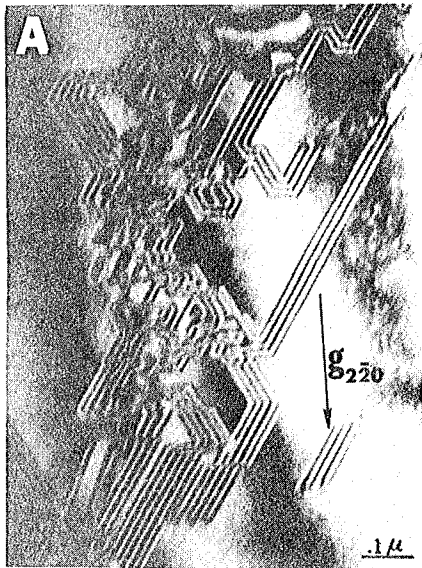
Fig. 32





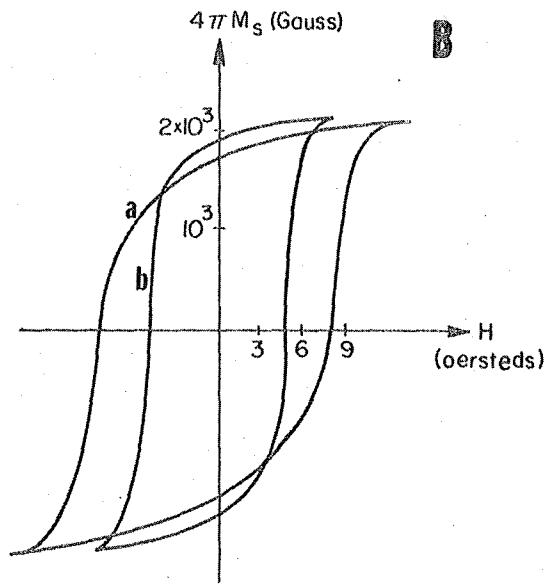
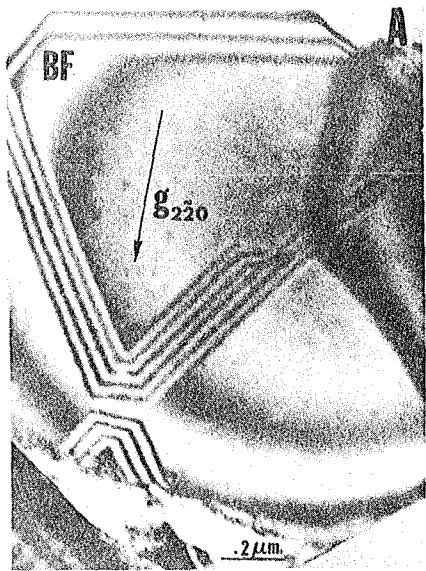
XBB 766-5125

Fig. 33.



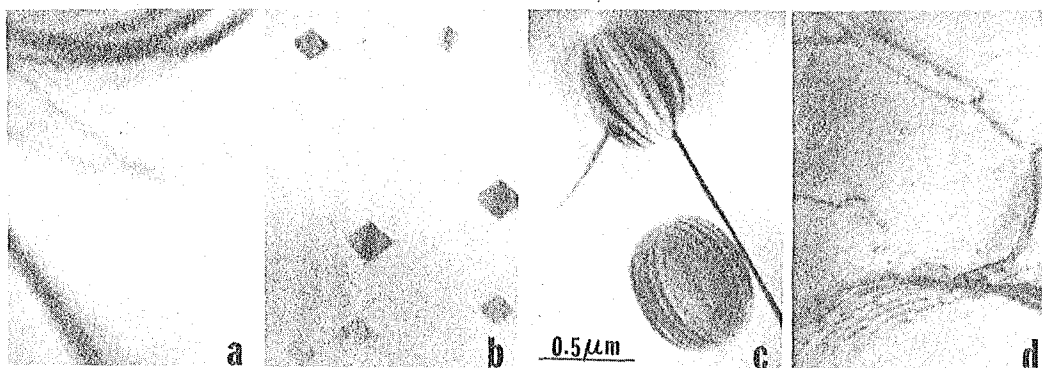
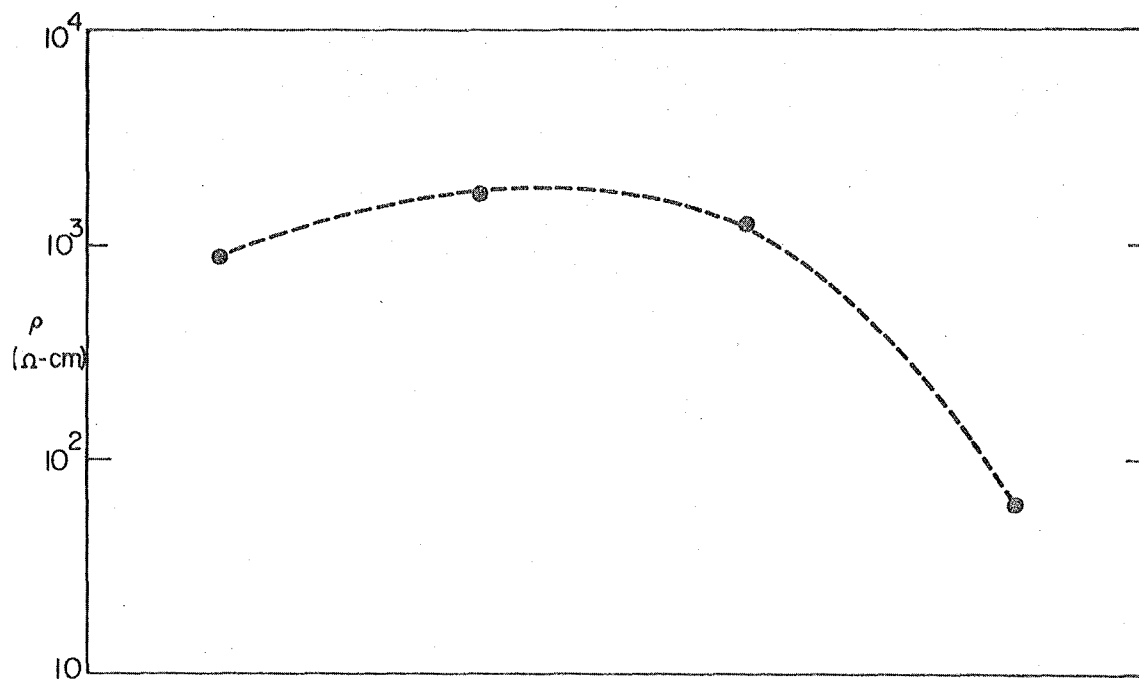
XBB 766-5126

Fig. 34.



XBB 766-5124

Fig. 35.



XBB 760-10725

MICROSTRUCTURES

Fig. 36.



This report was done with support from the United States Energy Research and Development Administration. Any conclusions or opinions expressed in this report represent solely those of the author(s) and not necessarily those of The Regents of the University of California, the Lawrence Berkeley Laboratory or the United States Energy Research and Development Administration.

TECHNICAL INFORMATION DIVISION  
LAWRENCE BERKELEY LABORATORY  
UNIVERSITY OF CALIFORNIA  
BERKELEY, CALIFORNIA 94720